JETP Letters, Vol. 80, No. 8, 2004, pp. 523–526. Translated from Pis'ma v Zhurnal Éksperimental'noĭ i Teoreticheskoĭ Fiziki, Vol. 80, No. 8, 2004, pp. 595–599.

Effect of Superfluidity on the Structure of the Inner Crust of Neutron Stars

M. Baldo[1], U. Lombardo[1, 2], É. E. Saperstein[3], and S. V. Tolokonnikov[3]

[1] *Istituto Nazionale di Fisica Nucleare, Sezione di Catania, Via Santa Sofia 64, I-95129 Catania, Italy*

[2] *Universitá di Catania, I-95129 Catania, Italy*

[3] *Russian Research Centre Kurchatov Institute, pl. Akademika Kurchatova 1, Moscow, 123182 Russia*

e-mail: saper@mbslab.kiae.ru

Received August 4, 2004; in final form, September 13, 2004

A self-consistent, completely quantum calculation of the structure of the inner crust of neutron stars is carried out in the Wigner–Seitz approximation with a realistic phenomenological nuclear energy functional, where pair correlations of neutrons and protons are included in the explicit form. It has been shown that the superfluidity of neutrons and protons affects the structure of the ground state of the crust. © *2004 MAIK "Nauka/Interperiodica".*

PACS numbers: 21.60.–n; 21.65.+f; 26.60.+c

The superfluidity of the matter of neutron stars that was predicted by Migdal [1] periodically attracts interest. This interest has noticeably increased in the last two decades in connection with the accumulation of observation data on irregularities in the rotation periods of neutron stars. This phenomenon is associated with the appearance and disappearance of superfluid vortices in the inner crust of a neutron star (see review [2] and references cited therein). The inner crust is the part of the neutron-star shell with subnuclear densities $0.001\rho_0 \le \rho \le 0.5\rho_0$, where $\rho_0 \simeq 0.17$ fm^{-3} is the normal nuclear density. According to the current concepts, it consists of spherically symmetric nuclear-like clusters forming a crystal lattice immersed in a sea of neutrons and a virtually homogeneous sea of ultrarelativistic electrons responsible for the neutrality of the system. For a certain critical density $\rho_c \simeq 0.5\rho_0$, the inhomogeneous configuration becomes energetically unfavorable and a homogeneous neutron liquid with a small admixture of protons and electrons arises. In a narrow range near ρ_c, clusters can lose their spherical shape and rodlike ("spaghetti"), layered ("lasagna"), or other exotic configurations become preferable. According to the current concepts, the neutron superfluidity of the inner crust of neutron stars is important not only for irregularities in the rotation periods but also for the cooling of the neutron star during its evolution [2].

As a rule, the superfluidity of only the primary neutron component is considered and it is described in the local density approximation. Namely, the superfluid gap $\Delta_n(\mathbf{r})$ at each point $\mathbf{r}$ with the neutron density $\rho_n(\mathbf{r})$ is identified with the gap of the infinite neutron matter of the same density. The latter gap is usually calculated using either the Brueckner method or the variational method with a realistic *NN* potential. The results of the different calculations agree well with each other. Comparatively recent completely quantum calculations of the gap $\Delta_n(\mathbf{r})$ for the inner crust of neutron stars were reported in [3, 4]. In those calculations, the size R_c of the Wigner–Seitz cell, the proton number Z_c in a cluster, and the mean-field form were chosen according to Negele and Vautherin [5]. Completed more than 30 years ago, their work remains the only completely quantum self-consistent description of the inner crust of neutron stars in the Wigner–Seitz method for a wide range of densities, but it disregards superfluidity. For a fixed mean density $\bar{\rho}$, the equilibrium values R_c and Z_c were determined in [5] as values corresponding to the energy minimum under the β-stability condition

$$\mu_n = \mu_p + \mu_e, \tag{1}$$

where μ_n, μ_p, and μ_e are the chemical potentials of neutrons, protons, and electrons, respectively, including their rest masses.

An important qualitative result obtained in [5] was the noticeable shell effect changing the relation between $\bar{\rho}$ and Z_c that had been predicted by semiclassical calculations available at that time (e.g., [6]). According to [5], two close local energy minima compete with each other in a wide range of densities. These minima correspond to the magic proton numbers Z_c = (giant quasi-nucleus Zr) 40 and (giant quasi-nucleus Sn) 50. According to calculations made in [5], with an increase in the density ρ, the first minimum is first lower than the second one, then the second minimum becomes lowest, and the first minimum again becomes lowest near ρ_c.

Several quantum calculations of the structure of the inner crust of neutron stars were carried out recently by

the Hartree–Fock method with the effective Skyrme forces (namely, with their SLy4 and SLy7 variants developed by the Lyon group specially for the description of neutron stars) [7–12]. In all those works, phase transitions near ρ_c between the aforementioned structures were analyzed disregarding pairing.

This work is aimed at studying the superfluidity effect on the structure of the inner crust of neutron stars far from ρ_c, where the topological structure of the system is unambiguous and the self-consistent calculation for a given density provides the equilibrium values of R_c and Z_c. In essence, we generalize the method developed in [5] by including the superfluidity of nucleons. It is worth noting that this region of the inner crust of neutron stars is of most interest for studying superfluidity effects, because the Δ value in nuclear matter is maximal for densities $\rho \le 0.5\rho_c$.

We apply the energy-functional method with pairing in the coordinate representation. It was presented in [13] and developed in detail by Fayans *et al.* [14]. The basic, central component of the energy functional has the form

$$\mathcal{E}_{\rm int} = \frac{C_0}{4}\left[a_+\rho_+^2\frac{1-h_1^+\rho_+/(2\rho_0)}{1+h_2^+\rho_+/(2\rho_0)} + a_-\rho_-^2\frac{1-h_1^-\rho_+/(2\rho_0)}{1+h_2^-\rho_+/(2\rho_0)}\right] + \mathcal{E}_{\rm abn}. \quad (2)$$

Here, the normalization factor $C_0 = (dn/d\varepsilon_F)^{-1}$ is the inverse density of states on the Fermi surface, $\rho_{+,-} = \rho_n \pm \rho_p$, $a_{+,-}$ and $h_{1,2}^{+,-}$ are dimensionless parameters, and the abnormal component of the energy functional responsible for superfluidity has the form

$$\mathcal{E}_{\rm abn} = \sum_{\tau = n,\,p} \mathcal{F}^{\xi,\tau}(\rho)\left|\nu_\tau(\mathbf{r})\right|^2. \quad (3)$$

Here, $\nu_\tau(\mathbf{r})$ is the abnormal density and $\mathcal{F}^{\xi,\tau}(\rho)$ is the density-dependent effective pairing interaction. For atomic nuclei, the interaction $\mathcal{F}^{\xi,\tau}$ is assumed to be independent of τ and this superscript will be omitted. As was shown in [14], the fine details of the isotopic behavior of some nuclear characteristics (e.g., the even–odd effect in rms radii) are sensitive to the details of the density dependence of $\mathcal{F}^{\xi}$, which testifies to the pairing interaction with pronounced surface enhancement. At the same time, most of the mean nuclear characteristics are well described by the simplest one-parametric density-independent interaction

$$\mathcal{F}^{\xi} = C_0 f^{\xi}, \quad (4)$$

which corresponds to the volume pairing. In this case, the parameter f^{ξ} must, however, depend weakly on the mass number so that it changes by about 20% from Ca to Pb. In addition to term (2), the total energy functional [14] contains the Coulomb and gradient terms, as well as the spin–orbit and other spin-dependent components.

The variation of expression (2) with respect to the density ρ_τ provides equations for the mean potentials $U_\tau(\mathbf{r})$ and variation with respect to the abnormal density ν_τ and equations for pairing gaps $\Delta_\tau(\mathbf{r})$ in terms of densities ρ and ν. The quantities U and Δ enter into the system of equations for the Bogoliubov functions $u_i(\mathbf{r})$ and $v_i(\mathbf{r})$, which, in turn, determine the densities ρ and ν through expressions known from [15]. Thus, we arrive at the system of equations that is equivalent to the equations of the Hartree–Fock–Bogoliubov method. We note that the method of Gor'kov equations providing close results was used in [14].

In this work, instead of the direct solution to the pairing problem in the coordinate representation, we use the simpler method of the expansion in the eigenfunctions

$$\phi_\lambda(\mathbf{r}) = \frac{y_{nlj}(r)}{r}\Phi_{jlm}(\mathbf{n})$$

of the problem without pairing (the isotopic index τ will be omitted). Here, Φ_{jlm} are the spin–angular functions and the functions $y_{nlj}(r)$ satisfy the radial Schrödinger equation with the potential $U(r)$ and the following usual boundary conditions at the boundary of a cell:

$$y_{nlj}(r = R_c) = 0 \quad (5)$$

and

$$\left(\frac{d(y_{nlj}/r)}{dr}\right)_{r = R_c} = 0, \quad (6)$$

for even and odd l values, respectively. The equation for the gap is solved in model space bounded by the single-particle energies $\varepsilon_\lambda < E_0$ (which are generally different for neutrons and protons).

The diagonal approximation $\Delta_{\lambda\lambda'} = \Delta_\lambda\delta_{\lambda\lambda'}$ for the gap significantly simplifies the calculations. The analysis performed in [14] for ordinary nuclei shows that the errors of the diagonal approximation for volume pairing are small, except the above-mentioned fine odd–even effects. To reduce the computation time, we use this approximation. In this case, the effective constant f^{ξ} depends (slightly, logarithmically) on the difference $E_0 - \mu$. Since $\mu_n \simeq \mu_p$ in stable nuclei, the same E_0 value corresponding to $E_0 - \mu \simeq 40$ MeV was used for protons and neutrons in [14]. The μ_n and μ_p values for the inner crust of neutron stars differ by tens of MeVs due to the erroneous neutron excess. Therefore, E_0^n must differ from E_0^p in order to use, at least approximately, the same f^{ξ} value from [14] for both subsystems.

Among the known phenomenological approaches, this method provides the maximum accuracy when reproducing the masses and particularly radii of stable spherical nuclei, including nuclei with a large neutron

excess. Therefore, it must well reproduce a nucleus-like cluster. We can look forward to reasonable predictions for the neutron environment, because the application of functional (2) to nuclear mater leads to an equation of state that is qualitatively close to the "realistic" equation of state obtained in the variational method or Brueckner method with realistic *NN* forces.

Figure 1 shows (solid line) the equation of state of neutron matter for energy functional (2) and (dotted line) the realistic equation of state obtained in the Brueckner method with the Argonne v18 *NN* potential [16]. For completeness, the equation of state for Skyrme SLy7 forces specially fitted to describe neutron matter is also shown (dashed line). As is seen, the difference between the three lines is small.

In this work, we present the results of calculations for only one value of the mean density corresponding to the Fermi momentum $k_F = 0.7$ fm^{-1} of the homogeneous neutron matter. For a given radius R_c, we determine the total nucleon number $A = \frac{4}{9\pi}(k_F R_c)^3$ in the cell. Then, this number is divided between Z protons and N neutrons ($A = Z + N$) such that β-stability condition (1) is satisfied. The self-consistent solution of the equations of the energy-functional method for the given R_c automatically provides the distribution of densities and other characteristics of the system that correspond to the minimum of the total binding energy. In addition to the integral of Eq. (2), this energy includes the contribution from Z electrons, which is calculated by standard methods [5].

Figure 2 shows the binding energy per nucleon E_B/A and the corresponding Z_c values calculated for the wide range R_c = 20–35 fm (dashed lines) without pairing ($f^\xi = 0$) and (solid lines) including pairing with the parameters $f^\xi = -0.45$ (the average value between Ca and Pb [14]), $E_0^n = 40$ MeV, and $E_0^p = 0$. For the case without pairing, the absolute minimum is reached for $R_c = 25$ fm and $Z_c = 40$, but it is only 1 keV below another local minimum for $R_c = 28$ fm and $Z_c = 50$ and the third minimum for $R_c = 30$ fm and the nonmagic number $Z_c = 58$. Finally, we note that a pronounced local minimum exists for $R_c = 21$ fm and magic $Z_c = 20$, but it is much higher. Thus, this calculation without pairing qualitatively corroborates the results obtained in [5], although details depend on the explicit form of the energy functional. However, the inclusion of pairing strongly changes the pattern: although a very weak local minimum remains for $R_c = 28$ fm and $Z_c = 50$, the absolute minimum is shifted to larger values, $R_c \simeq 31$ fm and $Z_c \simeq 70$.

It is not surprising that the pairing effects weaken the shell effect: this fact is well known for atomic nuclei. However, the weakening degree for the inner crust of neutron stars can be estimated only by direct calculation. One more effect is seen in Fig. 2: pairing

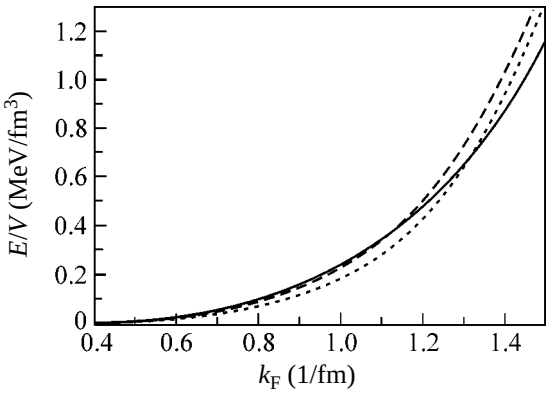

Fig. 1. Energy density of neutron matter.

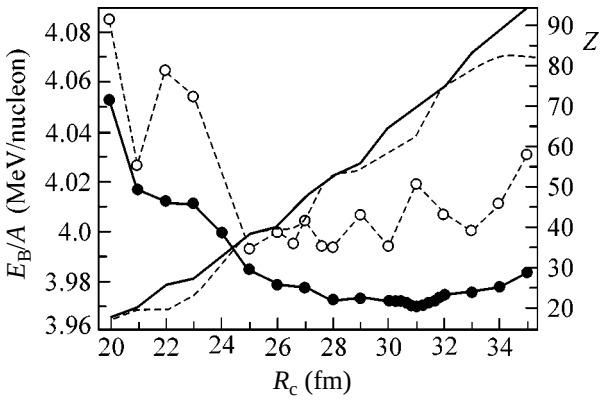

Fig. 2. Binding energy per nucleon and proton number Z_c in the Wigner–Seitz cell.

almost always increases Z_c. This effect can be easily explained. Indeed, since electrons inside the inner crust of neutron stars are ultrarelativistic, we have $\mu_e \simeq (9\pi Z_c/4)^{1/3}/R_c$. The substitution of this expression into β-stability condition (1) yields

$$Z_c \simeq \frac{4}{9\pi}(\mu_n - \mu_p)^3 R_c^3. \quad (7)$$

Pairing usually reduces μ_n and μ_p, because the chemical potential without pairing is determined by the single-particle energy of the last unoccupied level, whereas the chemical potential with pairing is most often between this level and the last occupied level. Moreover, these levels themselves become lower when pairing is included, because it increases the total binding energy of the system. This effect is more pronounced for protons than for neutrons, because the spacing between single-particle levels in the proton subsystem is much larger. Indeed, this spacing in the proton and neutron subsystems is determined by the cluster radius R_{cl} and Wigner–Seitz cell radius R_c, respectively. The latter radius is noticeably larger than the former radius, and the level spacing is proportional to R^{-2}. At the same

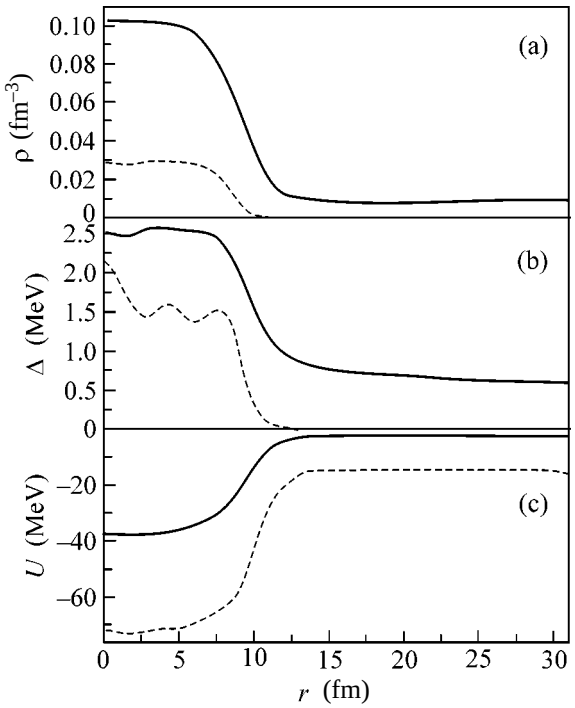

Fig. 3. (a) Density distributions, (b) pairing gaps, and (c) mean potentials for (solid lines) neutrons and (dashed lines) protons in the Wigner–Seitz cell for $R_c = 31$ fm with pairing.

time, this spacing is the measure of the effect under consideration. As a result, the difference between the chemical potentials on the right-hand side of Eq. (7) increases, usually, due to pairing, which leads to an increase in the equilibrium cluster charge Z_c.

For illustration, Fig. 3 shows the density distributions $\rho_n(r)$ and $\rho_p(r)$, pairing gaps $\Delta_n(r)$ and $\Delta_p(r)$, and mean potentials $U_n(r)$ and $U_p(r)$ corresponding to the equilibrium configuration for $R_c \simeq 31$ fm. As is seen, there is a pronounced cluster similar to atomic nuclei in its properties (but with a much deeper proton potential), and it sharply changes to almost homogeneous neutron matter. The description of this domain by energy functional (2) is obviously questionable. Therefore, the predictions of this calculation cannot be treated literally.

We note that the neutron gap depends only slightly on R_c. The behavior of the proton gap is more complex. Although the curve $\Delta_p(r)$ is usually close to that shown in Fig. 3, Δ_p inside the cluster decreases noticeably for magic Z values (even vanishes for $Z = 20$). We emphasize that the characteristic gap Δ_n or Δ_p is much smaller than the depth of the neutron or proton potential inside the cluster. Therefore, the inclusion of pairing is substantial only for a comparatively narrow group of states with energies $|\varepsilon_\lambda^{n,p} - \mu_{n,p}| \lesssim \Delta_{n,p}$. Their contribution to the total binding energy or total density is small. Therefore, for example, the density profiles of neutrons and protons as calculated for the same Z and R_c values in the approach under consideration and the approach developed in [5] (or, e.g., with the effective Skyrme forces) differ slightly from each other. Pairing changes the equilibrium values Z and R_c, because the chemical potentials $\mu_{n,p}$ appearing in β-stability condition (1), as well as the dependence of the binding energy on R_c, change when pairing is included (see Fig. 2).

We now develop a more realistic model of the inner crust of neutron stars. In this model, energy functional (2) is used only for the nuclear cluster, whereas an energy functional microscopically calculated for low-density neutron matter is used for the exterior region of neutron matter. Preliminary calculations corroborate the basic conclusion of this work that the inclusion of superfluidity is of fundamental importance for determining the equilibrium configuration of the inner crust of neutron stars.

We are grateful to M.V. Zverev, N.E. Zein, E.A. Ryabinkin, V.A. Khodel', and a referee of this paper for stimulating discussions and remarks. This work was supported by the Council of the President of the Russian Federation for Support of Young Russian Scientists and Leading Scientific Schools (project no. NSh-1885.2003.2).

REFERENCES

1. A. B. Migdal, Zh. Éksp. Teor. Fiz. **37**, 249 (1959) [Sov. Phys. JETP **10**, 176 (1960)].
2. C. J. Pethick and D. G. Ravenhall, Annu. Rev. Nucl. Part. Sci. **45**, 429 (1995).
3. F. Barranco, R. A. Broglia, H. Esbensen, and E. Vigezzi, Phys. Lett. B **390**, 13 (1997).
4. F. Barranco, R. A. Broglia, H. Esbensen, and E. Vigezzi, Phys. Rev. C **58**, 1257 (1998).
5. J. Negele and D. Vautherin, Nucl. Phys. A **207**, 298 (1973).
6. G. A. Baym, H. A. Bethe, and C. J. Pethick, Nucl. Phys. A **175**, 225 (1971).
7. F. Douchin and P. Haensel, Phys. Lett. B **485**, 107 (2000).
8. P. Magierski and P.-H. Heenen, Phys. Rev. C **65**, 045804 (2002).
9. A. Bulgac and P. Magierski, Nucl. Phys. A **683**, 695 (2001).
10. A. Bulgac and P. Magierski, Phys. Scr. T **90**, 150 (2001).
11. A. Bulgac and P. Magierski, Acta Phys. Pol. B **32**, 1099 (2001).
12. P. Magierski, A. Bulgac, and P.-H. Heenen, Nucl. Phys. A **719**, 217 (2003).
13. A. V. Smirnov, S. V. Tolokonnikov, and S. A. Fayans, Yad. Fiz. **48**, 1661 (1988) [Sov. J. Nucl. Phys. **48**, 995 (1988)].
14. S. A. Fayans, S. V. Tolokonnikov, E. L. Trykov, and D. Zawischa, Nucl. Phys. A **676**, 49 (2000).
15. A. B. Migdal, *Theory of Finite Fermi Systems and Applications to Atomic Nuclei* (Nauka, Moscow, 1965; Interscience, New York, 1967).
16. M. Baldo, C. Maieron, P. Schuck, and X. Vinas, Nucl. Phys. A **736**, 241 (2004).

Translated by R. Tyapaev

JETP Letters, Vol. 80, No. 8, 2004, pp. 527–531. Translated from Pis'ma v Zhurnal Éksperimental'noĭ i Teoreticheskoĭ Fiziki, Vol. 80, No. 8, 2004, pp. 600–604.

Giant Third Optical Harmonic Generation in Island Silver Films

E. M. Kim[1,*], S. S. Elovikov[1], T. V. Murzina[1], O. A. Aktsipetrov[1], M. A. Bader[2], and G. Marowsky[2]

[1] *Department of Physics, Moscow State University, Vorob'evy gory, Moscow, 119992 Russia*

** e-mail: JaneKim@shg.ru*

[2] *Laser-Laboratorium Göttingen, D-37077 Göttingen, Germany*

Received September 20, 2004

Giant third optical harmonic (TH) generation has been experimentally observed in island silver films. The TH intensity in the island silver films studied is more than two orders of magnitude higher than the value observed for the smooth surface of a homogeneous silver film. The mechanism of enhancement of the nonlinear cubic response is associated with the resonance enhancement of the local optical field at the TH wavelength, which is caused by the excitation of local surface plasmons in the ensemble of metal nanoparticles. © *2004 MAIK "Nauka/Interperiodica".*

PACS numbers: 73.61.–r

The phenomenon of giant second harmonic (SH) generation in island silver films was observed by Wokaum *et al.* [1] almost immediately after the discovery of surface-enhanced Raman scattering (SERS) [2] and surface-enhanced SH generation [3] on the rough surface of a silver electrode prepared by electrochemical etching. It was established [1] that the SH intensity in island silver films is by three orders of magnitude higher than the value observed for a smooth silver surface. The mechanism of this enhancement was immediately formulated in terms of the resonant local-field enhancement (at the pump or SH wavelength) due to the excitation of local surface plasmons in silver nanoparticles. The plasmon mechanism of the local-field enhancement was developed by Berreman [3] and Moskovits [4] based on the results of SERS investigations on rough metal surfaces. Experimental investigations of the plasmon mechanism of SERS and SH generation were performed for the rough surface of a silver electrode in an electrochemical cell [5] and for the rough surface of some other metals [6].

The nonlinear polarization of a single spherical nanoparticle at the SH frequency is expressed as

$$P_{2\omega} \sim L(2\omega)\chi^{(2)}(2\omega)L^2(\omega)E^2(\omega), \qquad (1)$$

where $\chi^{(2)}(2\omega)$ is the second-order nonlinear susceptibility and $L(\omega)$ and $L(2\omega)$ are the local field factors at the pump and SH frequencies, respectively. There are three factors influencing the magnitude and spectral position of the plasmon modes of metal nanoparticles and the corresponding local field factors. The first is the removal of degeneracy and the splitting of the frequency of the intrinsic plasmon modes of a metal nanoparticle caused by the deviation of the particle shape from the ideal sphere. The second factor determining the plasmon spectra of individual particles is the permittivity of the environment or (as in the case of island films) the substrate. An increase in the permittivity leads to a long-wavelength shift of the plasma resonance. Finally, the plasmon spectrum of an ensemble of metal particles (such as an island film) depends strongly on the dipole interaction between particles and, hence, on their number density in the film.

Generalization of relation (1) to the case of a nonlinear cubic inhomogeneity of the medium allows the nonlinear third-order polarization to be written as

$$P_{3\omega} \sim \langle L(3\omega)\rangle\langle\chi^{(3)}(3\omega)\rangle\langle L^3(\omega)\rangle E^3(\omega), \qquad (2)$$

where $\chi^{(3)}(3\omega)$ is the third-order nonlinear susceptibility, $L(3\omega)$ is the local field factor at the third harmonic (TH) frequency, and the symbol $\langle\ \rangle$ denotes averaging over random realizations of the spatial arrangement of nanoparticles in the island film ensemble.

Investigations of the optical (and nonlinear optical) phenomena in island films must take into account peculiarities in the morphology of such inhomogeneous systems which, representing a random two-dimensional ensemble of nanoparticles, exhibit spatial fluctuations both in the nonlinear susceptibilities and in the local field factors entering into Eqs. (1) and (2). These fluctuations lead to incoherency of the SH and TH generation processes, which should be considered in such cases as the hyper-Rayleigh scattering (HRS). Both these features of the nonlinear optics of random ensembles of metal nanoparticles—the enhancement and incoherency of the nonlinear response—were experimentally studied in much detail in the case of giant SH generation (see, e.g., [7]).

The phenomenon of HRS at the TH frequency in island films was reported in our previous paper [8], but

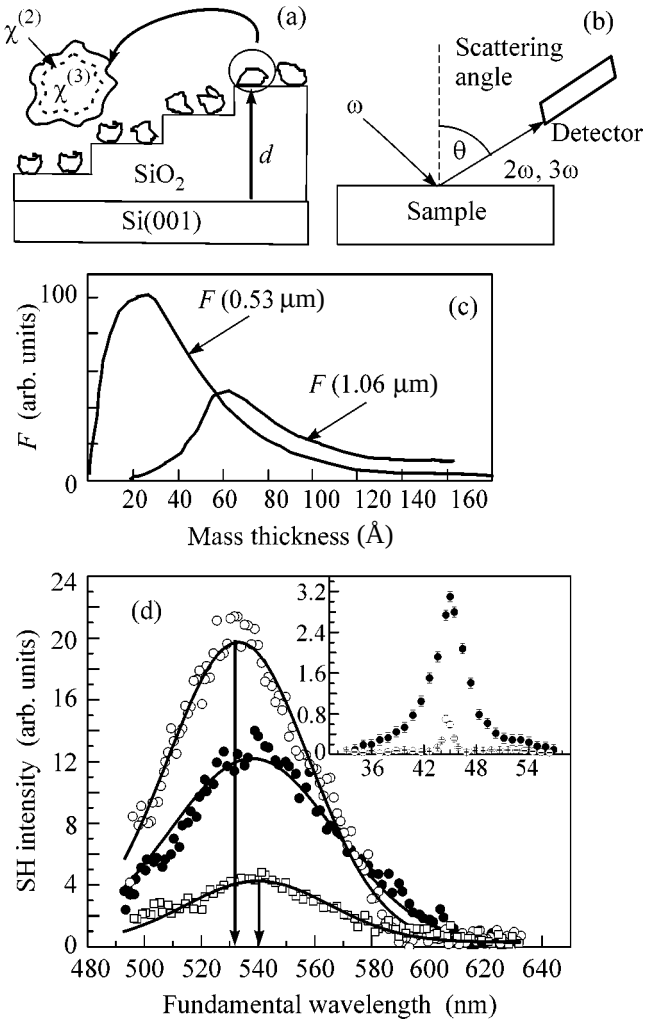

Fig. 1. (a) Schematic diagram of an island silver film deposited over a stepped wedge of silicon oxide on the surface of a silicon substrate; a silver nanoparticle depicted on a greater scale shows localization of the quadratic (surface) and cubic (volume) nonlinear susceptibilities; (b) schematic diagram showing the ray geometry for the measurement of polar scattering indicatrices of incoherent diffuse SH and TH; (c) plots of the local field factor F versus the effective film thickness at a wavelength of 0.53 and 1.06 μm (reproduced from [1]); (d) SH intensity spectra for an island silver film on the stepped oxide wedge at an oxide layer thickness of d = (open circles) 100, (black circles) 70, and (native oxide, open squares) 0 nm; solid curves are the Gaussian approximations of the experimental plots; the inset shows (black circles) the HRS indicatrix at the SH wavelength for the island silver film and (open circles) the angular instrumental function of the detection system.

the strong enhancement of TH generation has not yet been considered. By analogy with the giant SH generation in island silver films, we may expect that the giant TH enhancement may also take place due to the mechanism of the resonance excitation of local surface plasmons. Additional interest in the giant TH generation is stimulated by the fact that this process involves the third-order nonlinear susceptibility localized in the volume of nanoparticles (see the inset in Fig. 1a). Thus, the SH and TH generation processes provide different but mutually complementary information about the electron properties of nanoparticles.

This paper reports the observation and experimental investigation of the giant TH generation in island silver films. The nonlinear optical spectroscopy of TH generation in an island silver film deposited onto a silicon substrate with a controlled variable distance from the silicon surface to the silver nanoparticles shows evidence of a plasmon enhancement mechanism.

The island silver films were deposited onto a Si(001) substrates by thermal evaporation in a vacuum system with a residual gas pressure not exceeding 10^{-5} Torr. Silicon plates were selected as substrates because of their highly smooth and homogeneous surface. In order to detect the giant TH generation, we prepared films of two types: (i) thin films with an island structure and an effective mass thickness of 1 nm and (ii) thick homogeneous films with a thickness of about 40 nm (which is greater than the skin layer thickness on silver). The mass thickness of a film is critical for observation of the giant TH, because this parameter determines the morphology of the island film, in particular, the size of the nanoparticles and, hence, their local plasma resonance frequency.

Figure 1c shows plots of the local field factor F versus the mass thickness of a silver film (reproduced from [1]). These plots reveal a shift of the resonance maximum of the local field factor at the SH wavelength toward lower film thicknesses relative to the resonance at the pump wavelength. According to these results, we selected the film with a mass thickness of 1 nm for detecting the giant TH generation. This thickness was suggested to correspond to the resonance of the local field factor at the TH frequency under our experimental conditions. The 40-nm-thick homogeneous silver film was used as the reference of a nonenhanced TH signal for evaluating the enhancement factor in the case of giant TH generation in island silver films.

In order to study the plasmon mechanism of the giant TH enhancement, we used a special structure comprising a stepped wedge of silicon oxide on a silicon substrate, on which the sample island film was deposited. Using this structure, it was possible to study the influence of the permittivity of the semiconductor substrate on the spectrum of local plasmons excited in the island silver film. The stepped wedge was prepared as follows. First, a 100-nm-thick high-quality silicon oxide layer was grown on a Si(001) plate surface. Then, steps with a constant height increment of about 5 nm were formed in this oxide layer by etching at a rate of 5 nm/min in a buffer solution of NH_4F with hydrofluoric acid. This stepped wedge with oxide steps of variable height within $d \sim 5$–100 nm is schematically depicted in Fig. 1a. Using this wedge, it was possible to control the distance between the island film and semiconductor substrate, thus, varying the plasma reso-

nance parameters and, hence, the local field factors in Eqs. (1) and (2).

The surface topography of island silver films was studied using an atomic force microscope. The results of these measurements showed that the average particle size in the film plane was 60–70 nm and the average particle height was 6–10 nm.

The nonlinear optical measurements of the TH intensity enhancement and the indicatrices of diffuse TH scattering were performed using a YAG:Nd^{3+} laser with a wavelength of 1064 nm, a pulse power density of 10 MW/cm^2, a pulse width of 15 ns, and a pulse repetition rate of 25 Hz. The nonlinear optical spectroscopy of the TH generation was carried out using the radiation of a Spectra-Physics MOPO 710 parametric light generator tunable in a spectral range of 490–670 nm with a pulse width of 4 ns and a pulse energy of 10 mJ excited by the third-harmonic radiation of the YAG:Nd^{3+} laser. A part of the pump radiation was diverted into a reference channel, which allowed the SH and TH responses of the island silver films to be normalized to the corresponding signals from a reference quartz crystal, thus, reducing the influence of fluctuations in the pump power on the accuracy of the measurements. The SH and TH response signals were detected, after passage through the corresponding UV or blue–green filters, by a photomultiplier and a lock-in detection system. By means of the polar rotation of the detection system, it was possible to measure the HRS indicatrices at the SH and TH wavelengths (Fig. 1b), while the rotation of a sample about the normal to the surface was used for studying the anisotropy of the SH and TH intensity, which was necessary for separating the isotropic contribution to the nonlinear response due to the island film from the anisotropic contribution due to the substrate.

In measurements of the total (integrated over the polar angle) TH and SH intensity, it is necessary to take into account the diffuse component of the corresponding signal, $\int (I_{\mathrm{Si+Ag\,film}}(\theta) - I_{\mathrm{Si}})d\theta$, where θ is the scattering angle, I_{Si} is the mirror coherent signal from the Si(001) substrate surface, $I_{\mathrm{Si+Ag\,film}}(\theta)$ is the total signal including both the mirror coherent signal from the silicon surface and the island film and the diffuse incoherent signal from the silver nanoparticles, which is dependent on the scattering angle. The inset in Fig. 1d shows (i) the typical HRS indicatrix measured at the SH wavelength for the *s*–*s* combination of the polarizations of the fundamental and SH waves and (ii) the angular instrumental (transmission) function of the system of measurement of scattering indicatrices. The *s*–*s* geometry was selected taking into account strict selection rules [9] prohibiting the isotropic mirror SH component generation on the smooth silicon surface. The diffuse SH signal component observed in the angular interval 33°–57° shows the presence of an incoherent SH generated by a random ensemble of silver nanoparticles.

Figure 1d shows the SH intensity spectra for the identical island silver films deposited onto the stepped oxide wedge for three values of the oxide thickness. The curves clearly reveal the thickness-dependent shift of the SH resonance maximum toward longer wavelengths, which is explained by the influence of the real part of the permittivity of silicon on the local resonance plasma frequency in the island film. The amplitude of the resonance SH signal increases with increasing distance from the substrate to the silver nanoparticles, because the effect of the imaginary part of the permittivity of silicon on the amplitude of the resonance local field factor at the SH frequency decreases with increasing distance from the film to the silicon substrate.

In order to observe and quantitatively evaluate the giant TH enhancement, the TH intensity was measured for the samples of three types prepared on a silicon substrate with a constant oxide thickness of about 100 nm. Figure 2a shows the azimuthal dependence of the TH intensity for (i) the island silver film with an effective mass thickness of about 1 nm, (ii) a thick homogeneous reference silver film, and (iii) a Si(001) surface without deposited layers. All measurements were performed for the *s*–*s* combination of the polarizations of the fundamental and TH waves.

The TH intensity for the Si(001) surface as a function of the azimuthal angle can be expressed as

$$I_{3\omega}^{ss}(\varphi) \sim \{\chi^{(3)}(3\omega)\}^2 (E^3(\omega))^2 [a + b\cos(4\varphi)], \quad (3)$$

where φ is the azimuthal angle and a and b are the numerical coefficients related to a particular form of the cubic nonlinearity tensor and the incidence angle of the pump radiation. The anisotropic term in relation (3) is of the same order of magnitude as the isotropic term ($I_{\mathrm{Si}}^{\mathrm{isot}} \approx I_{\mathrm{Si}}^{\mathrm{anis}}$), which can be seen from the experimental dependences in Fig. 2a (open circles). A comparison of the isotropic and anisotropic contributions to the TH intensity in the films of various types (Fig. 2a) shows that the presence of an island film, on the one hand, significantly increases the total isotropic TH component due to the isotropic incoherent contribution from silver nanoparticles ($I_{3\omega}^{\mathrm{isot}} = I_{\mathrm{Si+Ag\,film}}^{\mathrm{isot}} / I_{\mathrm{Si}}^{\mathrm{isot}} = 2.6$) and, on the other hand, reduces the anisotropic component of the total TH signal ($I_{3\omega}^{\mathrm{anis}} = I_{\mathrm{Si+Ag\,film}}^{\mathrm{anis}} / I_{\mathrm{Si}}^{\mathrm{anis}} = 0.46$). The latter effect is associated with the absorption of pump radiation and the TH signal (from the silicon substrate) in the island film, which leads to a decrease in the anisotropic signal intensity.

Similarly to the case of the giant SH generation considered above, evaluation of the enhancement factor for the giant TH generation requires the measurement of the diffuse TH component for obtaining the TH intensity integrated with respect to the polar angle.

The inset in Fig. 2b shows (i) the HRS indicatrix measured at the TH wavelength for the island silver film and (ii) the angular instrumental (transmission)

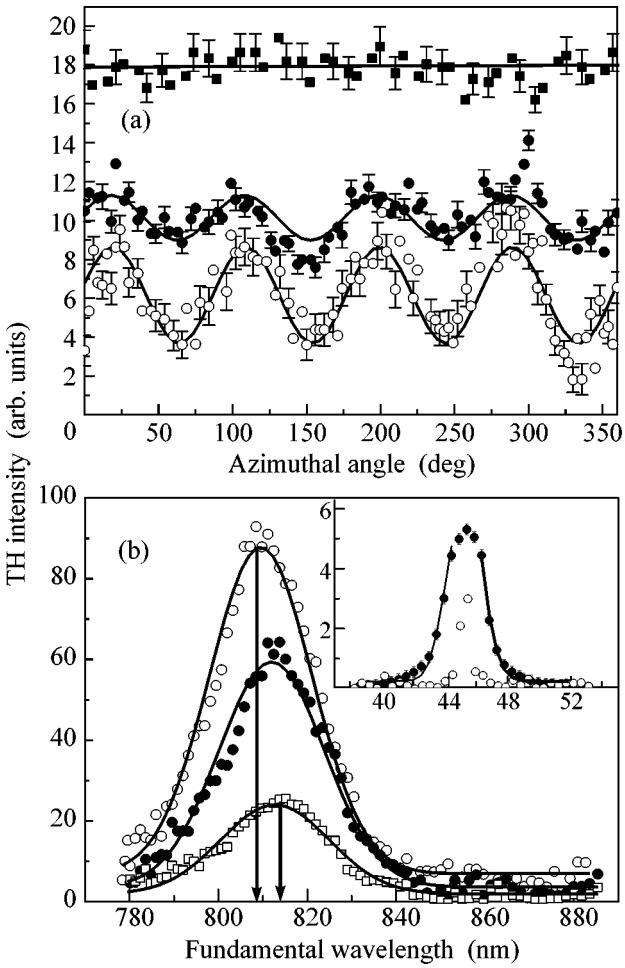

Fig. 2. (a) Plots of the TH intensity versus azimuthal angle for the clean Si(001) surface (open circles), thin island silver film (black circles), and thick reference silver film (black squares); solid curves are the approximations by Eq. (3); (b) TH intensity spectra for the island silver film on the stepped oxide wedge at an oxide layer thickness of d = (open circles) 100, (black circles) 70, and (native oxide, open squares) 0 nm; solid curves show the Gaussian approximations of the experimental plots; the inset shows (black circles) the HRS indicatrix at the TH wavelength for an island silver film and (open circles) the angular instrumental function of the detection system, and the solid line is the approximation by Eq. (3) from [8].

function of the detection system. These curves were measured using the *s*–*s* combination of polarizations of the fundamental and TH waves. The diffuse component of the TH signal is observed in the angular interval 38°–52°.

The degree of the giant TH enhancement in island silver films can be evaluated using the expression

$$G(3\omega) = \frac{\int [I_{\mathrm{Si+Ag\,film}} - I_{\mathrm{Si}}]d\theta}{I^{\mathrm{isot}}_{\mathrm{thin\,Ag}}}, \qquad (4)$$

where $I^{\mathrm{isot}}_{\mathrm{thin\,Ag}}$ is the isotropic TH intensity component generated in the "conditional" thin homogeneous silver film with an effective mass thickness of about 1 nm (equivalent to the island film in the amount of silver). The TH intensity for such a conditional 1-nm-thick silver film can be estimated from the results of measurements of the TH intensity for the 40-nm-thick homogeneous reference silver film. Taking into account that (i) the pump radiation penetrates into the reference silver film to a depth of about 10 nm and (ii) the TH radiation is emitted from a layer with a thickness on the same order, the enhancement of the giant TH generation can be evaluated using the ratio $I^{\mathrm{isot}}_{\mathrm{thin\,Ag}}/I^{\mathrm{isot}}_{\mathrm{thick\,Ag}} = 1/10^2$. Once the $I^{\mathrm{isot}}_{\mathrm{thick\,Ag}}$ is experimentally determined (Fig. 2a) we can calculate $I^{\mathrm{isot}}_{\mathrm{thin\,Ag}}$ and estimate the TH enhancement factor, which has proved to be $G(3\omega) = 1.4 \times 10^2$. A comparison of the enhancement factor for the giant SH generation (according to our results and the data from [1]) to the giant TH enhancement factor experimentally determined in this study shows a somewhat lower enhancement in the case of the giant TH generation, which is probably due to a higher absorption of the TH radiation in silver.

In order to study the role of the local plasma resonance in the mechanism of the giant TH enhancement, we have studied the TH spectra for identical island films deposited onto the surface of the stepped oxide wedge. Figure 2b shows the spectra of the giant TH intensity for three values of the oxide layer thickness. Similarly to the case of the SH spectroscopy, the curves reveal a shift of the TH intensity resonance maximum toward shorter wavelengths with increasing distance between the silver nanoparticles and silicon substrate. This behavior of the TH intensity resonance shows the influence of the real and imaginary parts of the permittivity of the substrate on the behavior of the local plasma resonance frequency and confirms the proposed plasmon mechanism of the giant TH generation enhancement.

In conclusion, we observed the phenomenon of giant TH generation in a two-dimensional ensemble of silver nanoparticles with an enhancement coefficient of 1.4×10^2 relative to the TH intensity for a homogeneous silver film. The results of the investigation of the resonance spectra of the TH intensity in a wedge structure with variable distance between the silver nanoparticles and semiconductor substrate showed that the mechanism of enhancement of the giant TH intensity is associated with the enhancement of the local optical fields as a result of the excitation of local surface plasmons in the ensemble of silver nanoparticles.

This study was supported by the Russian Foundation for Basic Research (project nos. 04-02-16847, 04-02-17059, 03-02-39010, and 01-02-04018), the Council of the President of the Russian Federation for Support of Young Russian Scientists and Leading Sci-

entific Schools (project no. NSh-1604.2003.2), the NATO Science for Peace Program (grant no. PST.CLG.979406), and the INTAS (grant no. 03-51-3784).

REFERENCES

1. A. Wokaun, J. G. Bergman, J. P. Heritage, *et al.*, Phys. Rev. B **24**, 849 (1981).
2. C. K. Chen, A. R. B. de Castro, and Y. R. Shen, Phys. Rev. Lett. **46**, 145 (1981).
3. D. W. Berreman, Phys. Rev. **163**, 855 (1967).
4. M. Moskovits, J. Chem. Phys. **69**, 4159 (1978).
5. C. K. Chen, A. R. B. de Castro, and Y. R. Shen, Phys. Rev. Lett. **46** (2), 145 (1981).
6. G. T. Boyd, Th. Rasing, J. R. R. Leite, and Y. R. Shen, Phys. Rev. B **30**, 519 (1984).
7. M. Breit, V. A. Podolsky, S. Gresillon, *et al.*, Phys. Rev. B **64**, 125106-1 (2001).
8. E. M. Kim, S. S. Elovikov, and O. A. Aktsipetrov, JETP Lett. **77**, 158 (2003).
9. O. A. Aktsipetrov, I. M. Baranova, and Yu. A. Il'inskii, Sov. Phys. JETP **64**, 167 (1986).

Translated by P. Pozdeev

JETP Letters, Vol. 80, No. 8, 2004, pp. 532–534. Translated from Pis'ma v Zhurnal Éksperimental'noĭ i Teoreticheskoĭ Fiziki, Vol. 80, No. 8, 2004, pp. 605–608.

Real-Time Observation of the Dynamics of Vibrational-Energy Redistribution within an Isolated Polyatomic Molecule by Spontaneous Raman Spectroscopy

A. L. Malinovsky, A. A. Makarov*, and E. A. Ryabov

Institute of Spectroscopy, Russian Academy of Sciences, Troitsk, Moscow region, 142190 Russia

**e-mail: amakarov@isan.troitsk.ru*

Received September 22, 2004

The dynamics of intramolecular vibrational-energy redistribution from an initially excited mode ν_1 (the acetylene-type H–C bond) to the other modes of the H–C≡C–Si$(CH_3)_3$ molecule was studied experimentally. Probing was performed by spontaneous anti-Stokes Raman scattering. The measured deexcitation time of ν_1 was 128 ± 10 ps. © *2004 MAIK "Nauka/Interperiodica".*

PACS numbers: 33.20.Fb; 34.30.+h; 42.62.Fi

Intramolecular vibrational-energy redistribution (IVR) is a fundamental phenomenon apparently inherent in any polyatomic molecule if it is excited highly enough [1–13]. The following subjects of investigations in this area are of paramount interest:

(i) energy thresholds above which the effect is observed for various molecules [4, 8];

(ii) vibrational spectra, which contain qualitative information on the existence of the effect and from which quantitative information on IVR dynamics can be derived in a number of cases [3, 7–9, 11, 12, 14];

(iii) this dynamics itself measured in real time [6, 15].

This paper presents the first direct measurement of the energy outflow rate from a mode of a moderately complex molecule by spontaneous Raman scattering (RS) spectroscopy. The experiment was performed with the H–C≡C–Si$(CH_3)_3$ molecule in the gas phase. The $\nu_1 \approx 3312$ cm^{-1} mode of this molecule, which corresponds to the acetylene-type H–C bond, is the highest frequency mode. It differs substantially in frequency from the C–H modes of methyl groups. The transition $|v_1 = 0\rangle \longrightarrow |v_1 = 1\rangle$ was selectively excited by a radiation pulse of an optical parametric oscillator (OPO). The excited molecules were probed by a radiation pulse of a picosecond Nd^{3+}:YAG laser (operating at a wavelength of 1.064 μm). Namely, the anti-Stokes Raman-scattering signal integrated over the ν_1 band was measured as a function of the delay time between the pump and probe pulses. The magnitude of this signal is proportional to the energy in the probed vibrational degree of freedom of the molecule [2, 4, 8, 16].

The experimental design is schematically shown in Fig. 1. The Nd^{3+}:YAG laser with a half-maximum pulse duration of 44 ps was used both for pumping the OPO and for RS probing. The laser pulse was divided between these two channels. The OPO was designed according to a noncollinear scheme [17] based on $LiNbO_3$ crystals. The pump and probe pulse energies were 200–300 μJ and approximately 1.5 mJ, respectively. The pulse repetition rate was 6.25 Hz.

The pump and probe pulses were aligned using a dichroic mirror and were focused coaxially into a cell with an H–C≡C–Si$(CH_3)_3$ gas. The gas pressure was 30 Torr. The beam polarizations were mutually perpendicular. The profile of the pump-radiation beam in the caustic region was such that approximately 60% of the radiation passed through the hole 200 μm in diameter. The probe beam waist was considerably narrower in diameter: no more than 100 μm. The time delay between pulses was adjusted by means of a mechani-

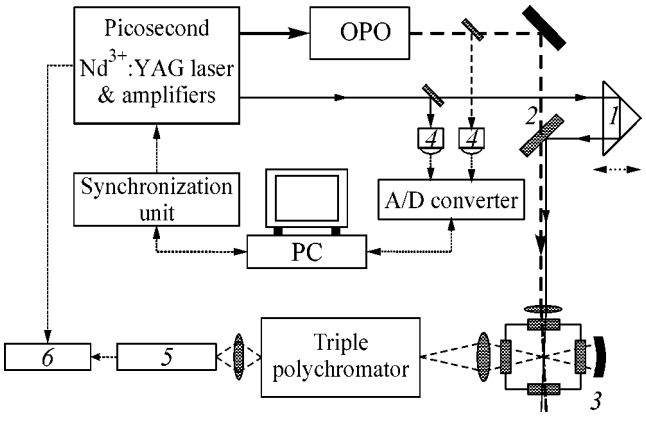

Fig. 1. Schematic diagram of the experimental setup: (*1*) prism, (*2*) dichroic mirror, (*3*) gas cell, (*4*) pulse energy control detectors, (*5*) photomultiplier, and (*6*) pulse counter.

0021-3640/04/8008-0532$26.00 © 2004 MAIK "Nauka/Interperiodica"

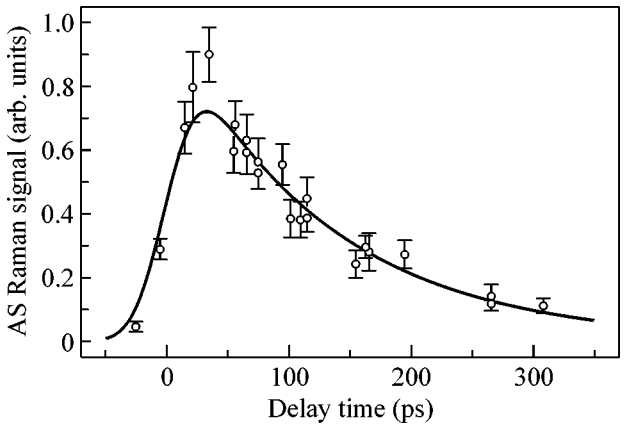

Fig. 2. Integral anti-Stokes RS signal in the ν_1 band of the H–C≡C–Si$(CH_3)_3$ molecule vs. the delay time of the probe pulse with respect to the pump pulse. The measurement error bars are determined by photocount statistics. The solid curve is the best fit to the experimental data by the double convolution of pump and probe pulses with the function $\theta(t)\exp(-t/\tau)$.

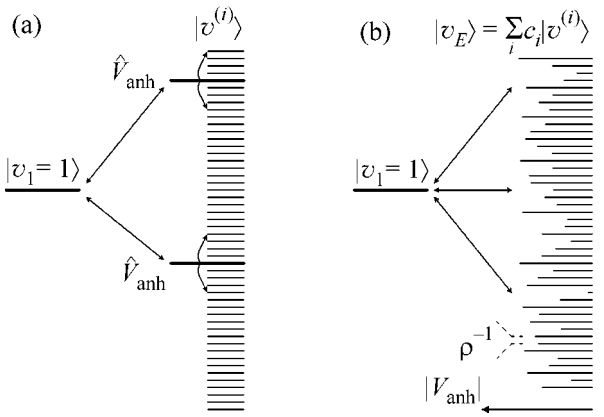

Fig. 3. Interaction of the excited state $|v_1 = 1\rangle$ with vibrational states close in energy. (a) If the states $|v_i\rangle$ are harmonic, the interaction with a few levels indicated by heavy lines dominates; these levels, in turn, are coupled with a few other levels, etc. (b) If the states $|v_i\rangle$ are strongly mixed so that they form new eigenstates $|v_E\rangle$, the initial interaction is redistributed over the entire quasi-continuous spectrum.

cally movable prism. Its positioning precision was ±0.05 mm, which corresponded to ±330 fs. The zero time delay between pulses was determined by the signal peak at the sum frequency $\omega_{OPO} + 2\omega_{YAG}$ generated as a result of upconversion in the lithium iodate crystal; the accuracy of this referencing was ±3.3 ps.

The OPO wavelength in the vicinity of 3 μm was tuned to the ν_1 band of the H–C≡C–Si$(CH_3)_3$ molecule. The OPO spectrum whose width measured by the upconversion method was about 50 cm^{-1} covered the rotational structure of the excited ν_1 band with guarantee. The RS signal was detected using a triple polychromator in the region of 785.7–788.1 nm, which completely covered the anti-Stokes position of the ν_1 band. The signal was recorded in the photon-counting mode by a Hamamatsu H7421-50 photomultiplier and an SR400 gated pulse counter.

The experimental results are presented in Fig. 2. The experimental points are well described by a dependence implying that energy is transferred from the initially excited mode to other vibrational degrees of freedom of the molecule according to an exponential law with a time constant of $\tau = 128 \pm 10$ ps. Undoubtedly, this time characterizes the dynamics of vibrational-energy redistribution within the isolated molecule, because the mean free time at the aforementioned gas pressures in the cell exceeds the maximum delay time between the pump and probe pulses in Fig. 2 by more than an order of magnitude.

The physical cause for IVR is the anharmonic interaction of molecular vibrations. The good agreement of the observed dynamics with the exponential decay of the initial excitation is explained within the model that is recognized as the most probable though not the only possible IVR scenario [8, 13, 18, 19]. The model is applied to our case as follows (Fig. 3). The combination vibrational levels $|v^{(i)}\rangle \equiv |v_1 = 0;\ v_2^{(i)}\ v_3^{(i)} \ldots v_s^{(i)}\rangle$ with the excitation of some of the other $(s - 1)$ normal modes, except ν_1, with the energy $E^{(i)} \approx \sum_{j=2}^{s} v_j^{(i)} \nu_j$ in the vicinity of ν_1 are mixed with each other due to the anharmonic interaction.[1] High-order interactions coupling states with strongly differing sets of vibrational quantum numbers, which, in addition, can be localized on bonds weakly interacting with each other directly, play the key role in this picture. The particular realization of such high-order interactions is sequential mixing with exchange by a relatively small number of vibrational quanta due to the dominant cubic and/or quartic intermode anharmonicity [19]. It is suggested that a quasi-continuous spectrum of states $|v_E\rangle = \sum_i c_i |v^{(i)}\rangle$ is formed as a result. These states represent "random" superpositions of many harmonic states $|v^{(i)}\rangle$. According to [20], their density ρ for the H–C≡C–Si$(CH_3)_3$ molecule at an energy of 3312 cm^{-1} equals 2.1×10^4 levels/cm^{-1} with regard to only the states whose symmetry A_1 coincides with the symmetry of the ν_1 mode. Because the states $|v_E\rangle$ are "ergodic" [21] (that is, their wavefunctions are not localized on some normal vibrations), the anharmonic interaction $\hat{V}_{anh}$ of the state $|v_1 = 1\rangle$ with those states is random (Fig. 3b), as distinct from the situation where mixing is absent (Fig. 3a). It is natural to suggest that the characteristic scale of energy intervals in which $\hat{V}_{anh}$ fluctuates is the mean distance ρ^{-1} between the states $|v_E\rangle$. In this case, if the absolute value of the interaction matrix element

[1] The possible role of vibrational–rotational interactions will be discussed below.

$\langle v_1 = 1|\hat{V}_{\text{anh}}|v_E\rangle$ on the average considerably exceeds the inverse density of states, that is,

$$\left|\left\langle v_1 = 1\middle|\hat{V}_{\text{anh}}\middle|v_E\right\rangle\right| \gg \rho^{-1}, \quad (1)$$

then, according to the exact solutions of a number of model problems [22, 23], the quasi-continuous spectrum is virtually equivalent to a continuous one in the sense that the evolution of the population of the initially prepared state $|v_1 = 1\rangle$ is well approximated by an exponential decay at the rate[2]

$$\tau^{-1} = 2\pi\overline{\left|\left\langle v_1 = 1\middle|\hat{V}_{\text{anh}}\middle|v_E\right\rangle\right|^2}\rho. \quad (2)$$

Substituting the experimental τ value into Eq. (2), we find that inequality (1) is unconditionally fulfilled.

Furthermore, we note that the time of the energy redistribution from the ν_1 mode of the H–C≡C–Si$(CH_3)_3$ molecule to the other modes that is obtained in this work is by more than an order of magnitude shorter than the value of 2000 ps obtained from the treatment of the IR spectra of the same molecule in a cooled molecular beam [20]. Our value is in better agreement with the value of 96 ps obtained in a recent work [15] by IR–IR double resonance spectroscopy. However, in the latter case, the gas pressure was several tens of times higher than in our experiment so that the contribution of collisions to the measured time was possibly not excluded.

The difference between the results obtained from the IR spectra in a cooled beam and those obtained, as in this work, by a direct method but at room temperature is most likely associated with fundamental causes rather than "the experimental limitations of high-resolution infrared spectroscopy," as was stated as an assumption in [24]. A possible cause is the initial thermal excitation of low-frequency modes leading to an increase in anharmonic interactions (see also [24]). It seems likely that, along with anharmonic interactions, vibrational–rotational interactions (which increase rapidly as the rotational quantum numbers increase) can play an auxiliary role in the mode mixing in some specific cases. At present, only qualitative suggestions on this point are available (see, e.g., [25]). The estimation of the contribution of various mechanisms to the IVR rate is the subject of further experimental investigations and theoretical simulations.

We are grateful to E.P. Chukalina and S.A. Klimin for the auxiliary measurements of FTIR spectra; to Yu.S. Dolzhikov, V.B. Laptev, and N.-D.D. Ogurok for technical assistance; and to V.S. Letokhov for useful discussions. This work was supported by the Russian Foundation for Basic Research (project no. 02-02-16687), the Council of the President of the Russian Federation for Support of Young Russian Scientists and Leading Scientific Schools (project no. NSh-1772.2003), and the Ministry of Industry, Science, and Technology of the Russian Federation (state contract no. 40.020.1.1.11.61).

[2] It should certainly be kept in mind that, in contrast to the continuous case, significant return to the initial state can occur in the quasi-continuous case at long times. However, estimates show that it is virtually unobservable if at least ten levels are involved in the process.

REFERENCES

1. É. V. Shuryak, Zh. Éksp. Teor. Fiz. **71**, 2039 (1976) [Sov. Phys. JETP **44**, 1070 (1976)].
2. V. N. Bagratashvili, Yu. G. Vaĭner, V. S. Dolzhikov, *et al.*, Pis'ma Zh. Éksp. Teor. Fiz. **30**, 502 (1979) [JETP Lett. **30**, 471 (1979)].
3. H.-R. Dübal and M. Quack, Chem. Phys. Lett. **72**, 342 (1980).
4. V. N. Bagratashvili, Yu. G. Vaĭner, V. S. Dolzhikov, *et al.*, Zh. Éksp. Teor. Fiz. **80**, 1008 (1981) [Sov. Phys. JETP **53**, 512 (1981)].
5. G. M. Stewart and J. D. McDonald, J. Chem. Phys. **78**, 3907 (1983).
6. P. M. Felker and A. H. Zewail, Chem. Phys. Lett. **102**, 113 (1983).
7. E. Abramson, R. W. Field, D. Imre, *et al.*, J. Chem. Phys. **83**, 453 (1985).
8. *Laser Spectroscopy of Highly Vibrationally Excited Molecules*, Ed. by V. S. Letokhov (Adam Hilger, Bristol, 1989).
9. A. McIlroy and D. J. Nesbitt, J. Chem. Phys. **92**, 2229 (1990).
10. T. Uzer, Phys. Rep. **199**, 73 (1991).
11. K. K. Lehmann, G. Scoles, and B. H. Pate, Annu. Rev. Phys. Chem. **45**, 241 (1994).
12. D. J. Nesbitt and R. W. Field, J. Phys. Chem. **100**, 12735 (1996).
13. M. Gruebele, in *Advances in Chemical Physics*, Ed. by I. Prigogine and S. A. Rice (Wiley, New York, 2000), Vol. 114, p. 193.
14. V. N. Lokhman, A. A. Makarov, I. Yu. Petrova, *et al.*, J. Phys. Chem. A **103**, 11299 (1999).
15. H. S. Yoo, M. J. DeWitt, and B. H. Pate, J. Phys. Chem. A **108**, 1348 (2004).
16. E. Mazur, I. Burak, and N. Bloembergen, Chem. Phys. Lett. **105**, 258 (1984).
17. A. Seilmeier, K. Spanner, A. Laubereau, and W. Kaiser, Opt. Commun. **24**, 237 (1978).
18. A. Stuchebrukhov, S. Ionov, and V. Letokhov, J. Phys. Chem. **93**, 5357 (1989).
19. A. A. Stuchebrukhov and R. A. Marcus, J. Chem. Phys. **98**, 6044 (1993).
20. E. R. Th. Kerstel, K. K. Lehmann, T. F. Mentel, *et al.*, J. Phys. Chem. **95**, 8282 (1991).
21. S. A. Rice, in *Photoselective Chemistry*, Part 1, Ed. by J. Jortner, R. D. Levine, and S. A. Rice (Wiley, New York, 1981), Adv. Chem. Phys., Vol. 47, p. 117.
22. M. Bixon and J. Jortner, J. Chem. Phys. **48**, 715 (1968).
23. A. A. Makarov, V. T. Platonenko, and V. V. Tyakht, Zh. Éksp. Teor. Fiz. **75**, 2075 (1978) [Sov. Phys. JETP **48**, 1044 (1978)].
24. H. S. Yoo, D. A. McWhorter, and B. H. Pate, J. Phys. Chem. A **108**, 1380 (2004).
25. J. S. Go, G. A. Bethardy, and D. S. Perry, J. Phys. Chem. **94**, 6153 (1990).

Translated by A. Bagatur'yants

JETP Letters, Vol. 80, No. 8, 2004, pp. 535–539. From Pis'ma v Zhurnal Éksperimental'noĭ i Teoreticheskoĭ Fiziki, Vol. 80, No. 8, 2004, pp. 609–613.

Controlling Potential Traps for Filtering Solitons in Bose–Einstein Condensates¶

R. Fedele[1]*, P. K. Shukla[2], S. De Nicola[1], M. A. Man'ko[3], V. I. Man'ko[1], and F. S. Cataliotti[4]

[1] *Dipartimento di Scienze Fisiche and INFN, Università Federico II di Napoli, I-80126 Napoli, Italy*
** e-mail: renato.fedele@na.infn.it*
[2] *Ruhr-Universitat Bochum, Germany*
[3] *Lebedev Physical Institute, Russian Academy of Sciences, Moscow, 119991 Russia*
[4] *University of Catania, Italy*

Received August 5, 2004

We present a controlling potential method for solving the three-dimensional Gross–Pitaevskii equation (GPE), which governs the nonlinear dynamics of the Bose–Einstein condensates (BECs) in an inhomogeneous potential trap. Our method allows one to construct ground and excited matter wave states whose longitudinal profiles can have bright solitons. This method provides the confining potential that filters and controls localized BECs. Moreover, it is predicted that, while the BEC longitudinal soliton profile is controlled and kept unchanged, the transverse profile may exhibit oscillatory breathers (the unmatched case) or move as a rigid body in the form of either coherent states (performing the Lissajous figures) or a Schrödinger cat state (matched case). © *2004 MAIK "Nauka/Interperiodica".*

PACS numbers: 03.65.Ge; 03.75.Lm; 05.30.Jp; 05.45.Yv

It is well known that the dynamics of Bose-Einstein condensates (BECs) in condensed matters is governed by the Gross-Pitaevskii equation (GPE) [1]. Stationary solutions of the latter in one space dimension can be cast in the form of solitons [2]. The formation of bright and dark/grey solitons is attributed to the attractive as well as repulsive interatomic interaction and that were created experimentally in elongated BECs [3].

We consider here the multidimensional GPE with confining potentials for BECs and present a new analytical method for filtering different kinds of solitons by controlling the confining potential. This idea could be realized by recently developed techniques involving lithographically fabricated circuit patterns, which provide electromagnetic guides and microtraps for ultracold neutral systems of atoms in BEC experiments [4]. Alternatively, the use of optically induced potentials is also extremely versatile for producing "exotic" potentials [5].

We obtain exact controlled 3D solutions for the ground and excited soliton states of BECs.

The dynamics of BECs in a spatially nonuniform confining potential well are governed by the GPE [1]

$$i\hbar\frac{\partial\Psi(\mathbf{r},t)}{\partial t} = -\frac{\hbar^2}{2m_a}\nabla^2\Psi(\mathbf{r},t) + U(\mathbf{r},t,|\Psi(\mathbf{r},t)|^2)\Psi, \quad (1)$$

where $\hbar$ is the Planck constant divided by 2π; $\Psi(\mathbf{r}, t)$ is the macroscopic wave function of the condensate; m_a is the atomic mass; $U(\mathbf{r}, t, |\Psi(r, t)|^2) = V_{\text{ext}}(\mathbf{r}, t) + gN|\Psi(\mathbf{r}, t)|^2$, $V_{\text{ext}}(\mathbf{r}, t)$ is the external confining potential for BECs; the coupling constant g is related to the short range scattering (s-wave) length a representing the interactions between atomic particles, namely, $g = 4\pi\hbar a/m_a$; and N is the number of atoms. The short range scattering length a of the atoms can be either positive or negative, giving rise to either attractive or repulsive forces.

We consider a generic external potential composed of two parts, viz. $V_{\text{ext}}(\mathbf{r}, t) = V_\perp(\mathbf{r}_\perp, t) + V(z, t)$. We look for a solution of (1) in the form $\Psi(\mathbf{r}, z, t) = \Psi_\perp(\mathbf{r}_\perp, t)\Psi_z(z, t)$. Hence, Eq. (1) can be decomposed as

$$i\hbar\frac{\partial\Psi_\perp}{\partial t} = -\frac{\hbar^2}{2m_a}\nabla_\perp^2\Psi_\perp + V_\perp(\mathbf{r}_\perp, t)\Psi_\perp, \quad (2)$$

$$i\hbar\frac{\partial\Psi_z}{\partial t} = -\frac{\hbar^2}{2m_a}\frac{\partial^2\Psi_z}{\partial z^2} + g_{1\text{D}}N|\Psi_z|^2\Psi_z + V(z,t)\Psi_z, \quad (3)$$

where $g_{1\text{D}} = g\int|\Psi_\perp|^4 d^2r_\perp$. We see that the transverse and longitudinal equations are exactly decoupled, the former being a linear equation and the latter being the 1D cubic nonlinear Schrödinger equation (cNLSE) whose nonlinear coupling coefficient depends on the

¶ This article was submitted by the authors in English.

shape of the transverse BEC's density profile. Note also that g_{1D} is, in principle, a function of t ($g_{1D} = g_{1D}(t)$).

We assume that the transverse external potential is quadratic; i.e., $V_\perp(x, y, t) \equiv m_a[\omega_x^2(t)x^2 + \omega_y^2(t)y^2]/2$. Thus, Eq. (2) admits, in rectangular coordinates, the following complete set of normalized Hermite–Gauss modes: $\Psi_{\perp nm}(x, y, t) = \Psi_{xn}(x, t)\Psi_{ym}(y, t)$, where

$$\Psi_{jk}(j, t) = H_k[j/\sqrt{2}\sigma_j(t)] \times \frac{\exp[-j^2/4\sigma_j^2(t) + im_a\gamma_j(t)j^2/2\hbar + i\phi_{jk}(t)]}{[2\pi\sigma_j^2(t)2^{2k}(k!)^2]^{1/4}}, \quad (4)$$

with $j = x, y$ and $k = 0, 1, 2, 3, \ldots$. The quantities $\sigma_j(t)$, $\gamma_j(t)$, and ϕ_{jk} satisfy the following system of equations

$$d^2\sigma_j/dt^2 + \omega_j^2(t)\sigma_j - \hbar^2/4m_a^2\sigma_j^3 = 0, \quad (5)$$

$\gamma_j(t) = (1/\sigma_j(t))(d\sigma_j(t)/dt)$, $\phi_{jk}(t) = (2k + 1)\phi_{j0}(t)$, and $d\phi_{j0}(t)/dt = -\hbar/4m_a\sigma_j^2(t)$. Since Eq. (2) is linear, in principle, an arbitrary normalized solution $\Psi_\perp$ can be expressed as a linear combination of the above $\Psi_{\perp nm}$; i.e., $\Psi_\perp = \Sigma_{nm}c_{nm}\Psi_{\perp nm}$. Note that $\Psi_{j0}(j, t)$ is a purely Gaussian time-dependent fundamental mode and $\sigma_j(t)$ is its rms $\sqrt{\langle j^2\rangle}$. Consequently, the transverse effective spot size of the condensate can be defined as $\sigma_\perp(t) \equiv \sqrt{\sigma_x^2(t) + \sigma_y^2(t)}$. Equation (5) (a Pinney equation) describes the envelope oscillations of the condensate along the jth transverse direction within the quadratic potential well $V_j(j, t) = m_a\omega_j(t)j^2/2$.

For ω_j independent of time, Eq. (5) can be easily integrated. For the initial conditions: $\sigma_{j0} \equiv \sigma_j(t = 0)$ and $\gamma_{j0} \equiv \gamma_j(t = 0)$, we have for the BEC transverse envelope motion

$$\sigma_j(t) = \sigma_{j0}\left[\left(\cos\omega_j t + \frac{\gamma_{j0}}{\omega_j}\sin\omega_j t\right)^2 + \frac{\sigma_j^{*4}}{\sigma_{j0}^4}\sin^2\omega_j t\right]^{1/2}, \quad (6)$$

where $\sigma_j^* = \sqrt{\hbar/m_a\omega_j}$. From Eq. (6), it is evident that, if $\gamma_{j0} \neq 0$, the BECs execute envelope oscillations (breathers). If $\gamma_{j0} = 0$, the jth transverse BEC state is described by a wave function (given for each integer k by Eq. (4)) whose rms does not change in time (stationary state) when $\sigma_{j0} = \sigma_j^*$ (the matched case) or it executes oscillatory breathers when $\sigma_{j0} \neq \sigma_j^*$ (the unmatched case). In particular, for $k = 0$, this jth transverse state is described by the 1D harmonic oscillator ground state, which is purely Gaussian and has the characteristic of being the simplest coherent state. A complete set of coherent states in such a harmonic potential well can be obtained just by shifting the center of the Gaussian state by a time-dependent vectorial shift, say $\mathbf{r}_{\perp 0}(t) = (x_0(t), y_0(t))$, with respect to the minimum of the potential well obeying the classical harmonic oscillator motion.

We seek a solution of Eq. (3) in the form $\Psi_z(z, t) = F(z, t)\exp(-iE_at/\hbar)$, where E_a is a real number and F is a complex function (the solution of a cNLSE)

$$i\hbar\partial F/\partial t = -(\hbar^2/2m)\partial^2F/\partial z^2 + \beta|F|^2F. \quad (7)$$

Here β is a real constant. Consequently, we have to impose the following condition for the potential: $V(z, t) = [\beta - g_{1D}(t)N]|F|^2 + E_a$. Equation (7) admits bright (dark/grey) soliton solutions for $\beta < 0$ ($\beta > 0$). The main property of these solutions is that they are stationary profile solutions (nonlinear traveling waves); namely, $F(z, t) = \mathcal{F}(\xi)\exp(-iE_st/\hbar)$, where $\xi \equiv z - u_0t$, u_0, and E_s are arbitrary constants representing the soliton speed and nonlinear frequency shift, respectively. For $\beta < 0$, the bright standing (nontravelling) envelope soliton solution of Eq. (7) is $F(z, t) = (1/\sqrt{2l_z})\,\mathrm{sech}(z/l_z)\exp(-iEt/\hbar)$, where $E = \int F^*\hat{H}_zF\,dz$ is a negative arbitrary constant, which plays the role of an energy eigenvalue associated with the "nonlinear longitudinal eigenstate" of Eq. (7) and characterizes a continuous spectrum of the soliton energy.

In view of the above analysis, we realize that a method for filtering longitudinal bright soliton states of BECs can be established. Let us suppose that we want to produce a bright soliton with amplitude F_M and width l_z. First, we find from $F(z, t)$ the corresponding value of β and E; i.e., $\beta = -\hbar^2/m_al_z^2F_M^2$, $E = -\hbar^2/2m_al_z^2$. The latter shows a direct correspondence between the BEC longitudinal width l_z (soliton width) and its longitudinal energy E (soliton energy). So, one could also characterize the soliton continuous spectrum in terms of l_z. We then design, using the techniques described in [4, 5], an external potential well $V(z, t) = -(\hbar^2/ml_z^2)[1 + (mNl_z/2\hbar^2)g_{1D}(t)]\,\mathrm{sech}^2(z/l_z)$. Note that the external longitudinal potential well is time-modulated through the factor g_{1D}, which, in turn, depends on the time due to the time variation of the transverse rms $\sigma_j(t)$. Assuming that, by virtue of Eq. (4), $\Psi_\perp = \Psi_{\perp nm}$, we have $g_{1D}^{(nm)}(t) \equiv g\int|\Psi_{\perp nm}(x, y, t)|^4\,d^2r_\perp$, which can be cast as $g\delta_n\delta_m/2\pi^2\sigma_x(t)\sigma_y(t)$, where $\delta_k = (1/2^{2k}(k!)^2)\int_{-\infty}^{\infty}\exp(-2\xi^2)\,[H_k(\xi)]^4d\xi$. Let us now discuss the possibilities to use different modes as solutions to the linear transverse evolution equation describing the BEC state related to the factorized form of the BEC wave function. Having a solution $\Psi_\perp(x, y, t)$, one has controlling tools for the longitudinal soliton solution of the GPE. These tools are reduced to the time-dependent

variable g_{1D}. When each ω_j does not depend on time, $\sigma_j(t)$ is given by Eq. (6). Consequently, we have

$$V(z,t) = -\frac{\hbar^2}{m_a l_z^2}\left[1 + \frac{m_a N l_z g \delta_n \delta_m}{4\pi^2 \hbar^2 \sigma_x(t)\sigma_y(t)}\right]\mathrm{sech}^2\frac{z}{l_z}. \quad (8)$$

By virtue of (4), it is easy to see that the transverse BEC probability density of matter waves $|\Psi_{\perp nm}(x, y, t)|^2$ is affected by oscillatory breathers. In general, due to the linearity of Eq. (2), an arbitrary transverse BEC state $\Psi_\perp$, which can be expressed as a superposition of the Hilbert space base $\{\Psi_{\perp nm}\}$, should exhibit similar oscillatory breathers as well. It turns out that, in order to filter and control a longitudinal bright soliton profile of BEC while preserving its width, one has to impose an external potential well given by (8), which takes into account the transverse BEC breathers. A discussion of some special cases is in order. First, we consider the case of stationary transverse states (eigenstates of the transverse Hamiltonian $\hat{H}_\perp$). Here, the rms of the modes associated with the *j*th transverse direction satisfies the initial condition in the matched case ($\sigma_{j0} = \sigma_j^*$ with $\gamma_{j0} = 0$) and, consequently, does not change in time (there is no spread variation of the transverse BEC state). Thus, the external longitudinal potential well is reduced to the following time-independent form: $V(z) = -(\hbar^2/m_a l_z^2)(1 + m_a N l_z g \delta_n \delta_m / 4\pi^2 \hbar^2 \sigma_x^* \sigma_y^*)\,\mathrm{sech}^2(z/l_z)$, which shows that, in order to preserve the soliton distribution width (no spread variations), the potential controlling system does not have to account for breather effects. It follows that the corresponding controlled 3D BEC state is $\Psi_{nml_z}(x, y, z, t) = \psi_{nml_z}(x, y, z)\exp[iE_{nm}/\hbar]$,

$$E_{nm} = (n + 1/2)\hbar\omega_x + (m + 1/2)\hbar\omega_y - \hbar^2/2m_a l_z^2,$$

$$\psi_{nml_z}(x, y, z, t) = \frac{\exp[-(x^2/4\sigma_x^{*2}) - (y^2/4\sigma_y^{*2})]}{[4\pi\sigma_x^*\sigma_y^* l_z 2^{n+m} n!m!]^{1/2}} \times H_n(x/\sqrt{2}\sigma_x^*)H_m(y/\sqrt{2}\sigma_y^*)\,\mathrm{sech}(z/l_z), \quad (9)$$

where the subscript l_z accounts for the continuity of the longitudinal energy spectrum. On the contrary, the transverse energy is characterized by a discrete spectrum; i.e., $\langle \hat{H}_{\perp nm} \rangle = (n + 1/2)\hbar\omega_x + (m + 1/2)\hbar\omega_y$.

Figure 1 clearly shows the oscillatory breathers of both the BEC transverse density distributions and the temporal controlling potential function due to the transverse rms (spot size) oscillations. While this BEC "respiration" takes place, the soliton-like BEC longitudinal profile remains unchanged. For $n = m = 0$, the 2D transverse BEC cross section (transverse spot) is an ellipse whose shape changes progressively as the ratio $\sigma_x(t)/\sigma_y(t)$ changes in time. In particular, this ratio, which initially is <1, reaches 1 and subsequently becomes >1. For *n* and/or *m* greater than 1, the transverse spot is more than 1. For increasing values of *n* and

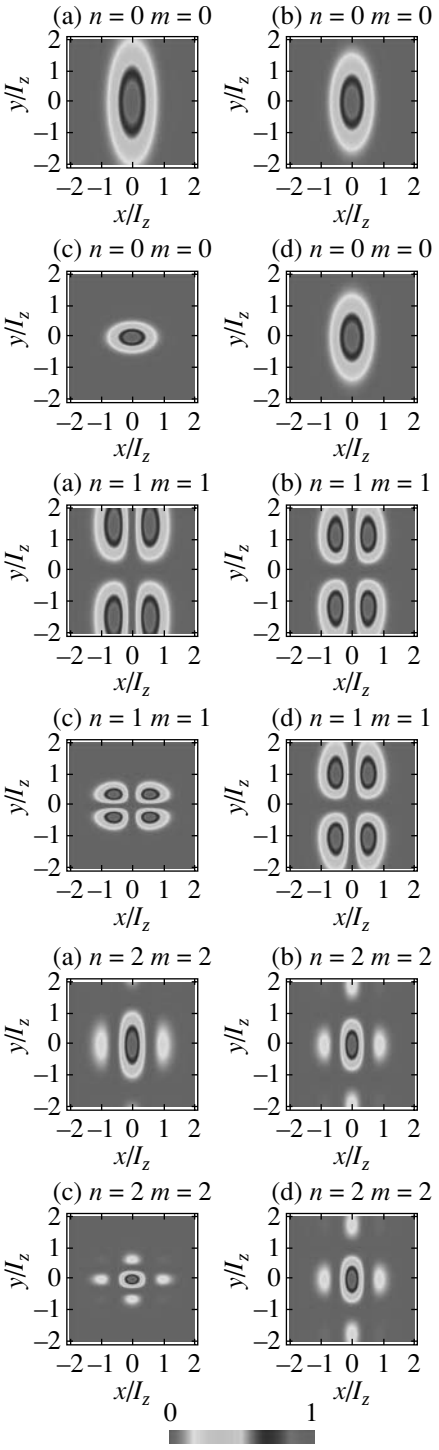

Fig. 1. Cross sections of the BEC transverse probability density $|\Psi_\perp|^2$ at $z = 0$ and different times: $t_1 = 1.57/\omega_x$ (a), $t_2 = 3.14/\omega_x$ (b), $t_3 = 4.71/\omega_x$ (c), and $t_4 = 6.28/\omega_x$ (d). The three groups of panels are plotted for different values of mode indices: $n = 0$, $m = 0$; $n = 1$, $m = 1$; $n = 2$, $m = 2$. The calculations refer to $\omega \equiv \omega_y/\omega_x = 0.5$, $\sigma_x^*/l_z = 0.5$, and $\sigma_y^*/l_z = \sigma_x^*/l_z\sqrt{\omega} = 1/\sqrt{2}$. The normalized transverse widths are $\sigma_{x0}/l_z = 0.5$ and $\sigma_{y0}/l_z = 1$; $\gamma_{x0}/\omega_x = 0.5$ and $\gamma_{y0}/\omega_y = 1$.

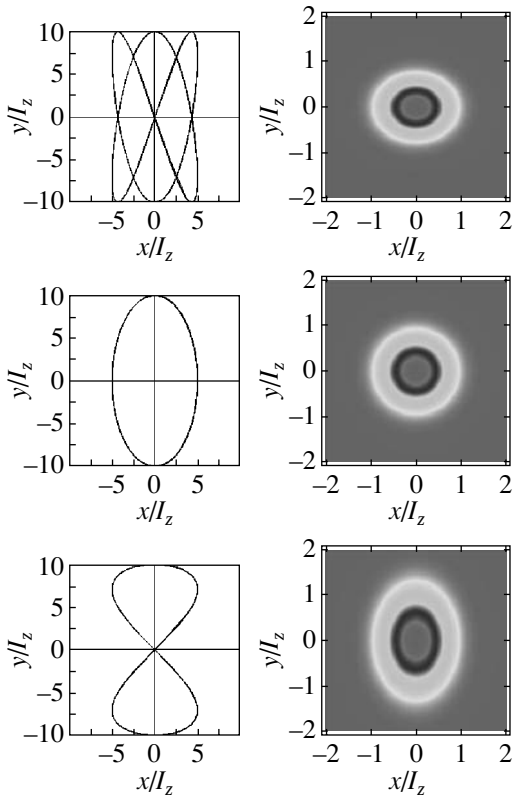

Fig. 2. Centroid motion of the coherent wavepacket per forming Lissajous figures (left panel) and the corresponding BEC transverse probability density $|\Psi_\perp|^2$ at $z = 0$ (right panel) for the ratio ω_y/ω_x equal to 1.5, 1.0, and 0.5, respectively (from top to bottom). The x and y components of the maximum amplitude of the centroid motion normalized with respect to l_z are 5 and 10, respectively. The relative phase between them is 1.57 rad and $\sigma_x^*/l_z = 0.5$, $\sigma_y^*/l_z = \sigma_x^*/l_z\sqrt{\omega_y/\omega_x}$. The ellipse eccentricity σ_x^*/σ_y^* is governed by $\sqrt{\omega_y/\omega_x}$.

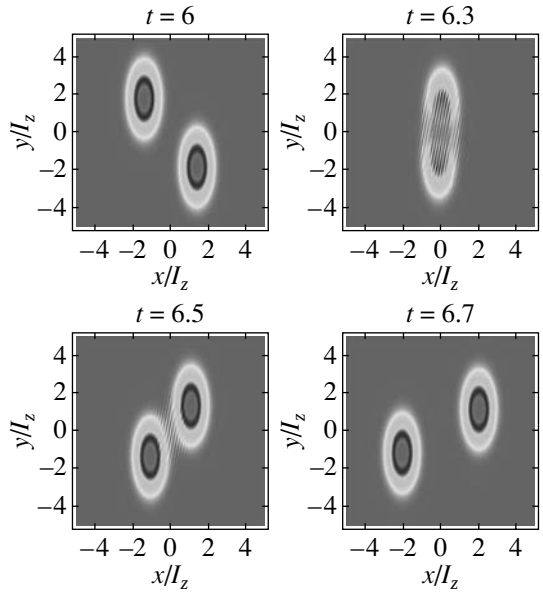

Fig. 3. Cross sections of the BEC transverse probability density $|\Psi_\perp|^2$ associated with the even coherent state (Schrödinger cat) at $z = 0$ and different tunes: $t_1 = 6.0/\omega_x$, $t_2 = 6.3/\omega_x$, $t_3 = 6.5/\omega_x$, and $t_4 = 6.7/\omega_x$. At time t_2, the Schrödinger cat state shows a marked interference effect as can be seen by the formation of a clear interference fringe pattern. The x and y components of the maximum amplitude of the centroid motion normalized with respect to l_z are 5 and 5, respectively. The relative phase between them is 1.57 rad and $\sigma_x^*/l_z = 0.5$, $\sigma_y^*/l_z = \sigma_x^*/l_z\sqrt{\omega_y/\omega_x}$ (ω_y/ω_x is put at 1/5).

m (higher modes), the numbers of transverse spots increase correspondingly and the time evolution of all the transverse spots shows the oscillatory breathers.

Second, we consider the case where the transverse BEC profile corresponds to a 2D coherent state. Consequently, while the soliton-like longitudinal BEC profile is kept by potential controlling, the transverse one is a bi-Gaussian with a moving centroid (guiding center) whose coordinates, say $x_0(t)$ and $y_0(t)$, satisfy the classical harmonic oscillator equations: $d^2j_0/dt^2 + \omega_j j_0 = 0$, $p_{0j} = -m_a dj_0/dt$. Thus, the Gaussian transverse BEC distribution moves, as its centroid, around in the transverse $x-y$ plane as a rigid body preserving shape and rms (no spread variations). This motion is the composition of the rigid oscillations along each transverse direction of each Gaussian distribution (preserving shape and rms as well) according to the corresponding centroid oscillation. The phase relation between these two oscillations should be imposed by the initial conditions. In principle, the transverse BEC centroid describes the Lissajous figures. While the transverse motion takes place, the shape of the longitudinal soliton distribution is preserved together with its width (no spread variations). Figure 2 shows the Lissajous figures described by the "rigid" motion of a BEC coherent state distribution in the $x-y$ plane, which does not exhibit any oscillatory breathers.

The third special case is the one where $\Psi_\perp$ is a Schrödinger cat state. In the Dirac formalism, we can construct such a state by taking, for the jth transverse direction, the superposition $(|\alpha_j\rangle \pm |-\alpha_j\rangle)/\sqrt{2}$, which is called the even (sign "+") or odd (sign "–") coherent state, where $\alpha_j(t) = j_0(t)/2\sigma_j^* + \sigma_j^* p_0(t)/\hbar$. This combination is also known as the Schrödinger cat (associated with the jth transverse direction). In order to have a 2D Schrödinger cat, one may construct the combination $(|\vec{\alpha}\rangle \pm |-\vec{\alpha}\rangle)/\sqrt{2}$, where $\vec{\alpha}$ is the complex vector: $\vec{\alpha} = \hat{x}\,\alpha_x + \hat{y}\,\alpha_y$. Figure 3 shows density plots in the $x/\sigma_x^* - y/\sigma_y^*$ plane of $|\Psi_\perp(x, y)|^2$ corresponding to a transverse BEC Schrödinger cat state at different times.

In conclusion, we have presented a controlling potential method for solving the 3D GPE that governs the nonlinear dynamics of BECs in nonuniform confining potentials. This novel approach seems to be possible thanks to the increasingly employed techniques used to produce almost arbitrary potential trap shapes, by using suitably tapered wires as in the microtraps techniques as well as by using suitably shaped laser beams as in the optical potential techniques. We have shown that stationary bright solitons with a finite transverse extent are filtered and controlled by a proper potential trap which, in turn, is selected on the basis of the shape of a soliton excited in BECs; therefore, $\propto \mathrm{sech}^2(z/l_z)$. The present result shows that, by controlling the longitudinal potential, it is possible to control the transverse characteristics of a BEC. This is of crucial importance for the possible realization of atomic waveguides, especially, in the framework of lithographic microtraps. We would like to point out that the present solitonic solutions are stable; i.e., a small deviation from the potential $V(z, t)$ will not result in destruction of the soliton. A more complete stability analysis will be the subject of future work.

ACKNOWLEDGMENTS

This research was partially supported by the INFN (Napoli) and by the Russian Foundation for Basic Research, project no. 03-02-16408.

REFERENCES

1. E. P. Gross, Nuovo Cimento **20**, 454 (1961); L. P. Pitaevskii, Sov. Phys. JETP **13**, 451 (1961).
2. F. Dalfovo *et al.*, Rev. Mod. Phys. **71**, 463 (1999).
3. S. Burger *et al.*, Phys. Rev. Lett. **83**, 5198 (1999); E. A. Donley *et al.*, Nature **412**, 295 (2001); B. P. Anderson *et al.*, Phys. Rev. Lett. **86**, 2926 (2001); L. Khaykovich *et al.*, Science **296**, 1290 (2002); B. Eiermann *et al.*, Phys. Rev. Lett. **92**, 230401 (2004).
4. J. Forthàgh *et al.*, Phys. Rev. Lett. **81**, 5310 (1998); J. Reichel, Appl. Phys. B **74**, 469 (2002); R. Folman *et al.*, Adv. At. Mol. Opt. Phys. **48**, 263 (2002).
5. R. Grimm *et al.*, Adv. At. Mol. Opt. Phys. **42**, 95 (2000).

JETP Letters, Vol. 80, No. 8, 2004, pp. 540–543. Translated from Pis'ma v Zhurnal Éksperimental'noĭ i Teoreticheskoĭ Fiziki, Vol. 80, No. 8, 2004, pp. 614–618.

^{63,65}Cu NMR Study of Low-Frequency Spin Dynamics in the Infinite-Layer Antiferromagnetic Compound $SrCuO_2$

K. N. Mikhalev[1], S. O. Rebrin[1], A. P. Gerashchenko[1], and T. V. D'yachkova[2]

[1] *Institute of Metal Physics, Ural Division, Russian Academy of Sciences, Yekaterinburg, 620219 Russia*

[2] *Institute of Solid State Chemistry, Ural Division, Russian Academy of Sciences, Yekaterinburg, 620219 Russia*

Received August 25, 2004

The spin–lattice and spin–spin relaxation times have been measured for ^{63,65}Cu NMR in the infinite-layer antiferromagnet $SrCuO_2$ in the ordered state for temperatures from 4.2 to 361 K. In the region of low temperatures ($T \le 250$ K), both relaxation processes are of the same nature and the main contribution to the relaxation rate is associated with the diffusion of a small number of holes with an activation energy of ~42 meV. In the high-temperature range ($T > 250$ K), contributions to the transverse relaxation rate exhibit redistribution and this relaxation process is determined predominantly by indirect interactions. *© 2004 MAIK "Nauka/Interperiodica".*

PACS numbers: 75.50.Ee; 76.60.–k

A considerable part of high-T_c superconductors were synthesized via heterovalent substitution or by changing the degree of oxidation in the initial antiferromagnetic compounds such as La_2CuO_4, $YBa_2Cu_3O_6$, and $Ca(Sr)CuO_2$. All these compounds are quasi-two-dimensional (2D) Heizenberg antiferromagnets with $S = 1/2$ and are of considerable basic significance as model systems featuring anisotropic interactions. These antiferromagnets are also of interest for investigations of the possible relationship between magnetism and superconductivity. For these reasons, such systems have been extensively studied in recent years [1–3].

The infinite-layer antiferromagnet $SrCuO_2$ (SCO) is the initial compound for the synthesis of a series of electron-doped superconductors of the $Sr_{1-x}R_xCuO_2$ system (R = La, Nd, Pr, …) with record high values of the superconducting transition temperatures for this class of compounds ($T_c \sim 40$ K). At the same time, the SCO is characterized by the simplest structural formula and crystal structure, since no apical oxygen is present between the copper planes. It should be also noted that the SCO is the least studied compound in the group of such oxides. The long-range magnetic order in this compound was found for the first time when the NMR spectra in the local field were measured by Ishida *et al.* [4] and then confirmed in [5]. The magnetic properties of the SCO were also studied only recently in [6], where we determined for the first time the Néel temperature ($T_N \approx 442$ K) and evaluated the exchange integrals. These data allowed the SCO, like its analogs, to be classified into 2D antiferromagnets.

The NMR technique, which is frequently used for the investigation of such compounds, is a very effective tool capable of replacing magnetic neutron diffractometry. In some cases [1, 3], NMR measurements even refine the data obtained by neutron diffraction. This ability is due to the fact that the nuclear magnetic moment is coupled with the electron spin moment via the hyperfine interaction constant. Hence, by recording the NMR spectra in the internal local field in the ordered state, it is possible to determine the value of the hyperfine field proportional to the sublattice magnetization. At the same time, by measuring the relaxation characteristics in the ordered state, it is possible to analyze the parameters of low-frequency spin correlations [7].

It should be noted that investigations of the spin dynamics by NMR in the initial 2D antiferromagnets in the ordered state are very few. In one of these studies performed for the infinite-layer antiferromagnet $Sr_{0.15}Ca_{0.85}CuO_2$ (SCCO) [8], it was demonstrated that the rates of both spin–spin and spin–lattice relaxations are determined primarily by mechanisms associated with the diffusion of holes, rather than by the spectrum of spin waves as it had been suggested previously [7, 9]. However, the SCCO is a less convenient object for the investigation of spin dynamics, since the considerable linewidth of the central transition in this compound, being much greater than that in the SCO, complicates determination of the spin relaxation times. Moreover, the SCCO features additional compositional disorder ion Ca(Sr) layers [6], which may influence the mechanism of hole diffusion. Thus, the behavior of the relaxation characteristics in the SCO may differ significantly from that in the SCCO.

This paper presents the results of investigation of the temperature dependence of the spin–lattice and spin–spin relaxation times in the infinite-layer antiferromagnet $SrCuO_2$ in the ordered state. An analysis of the relaxation characteristics for two copper isotopes, ^{63}Cu

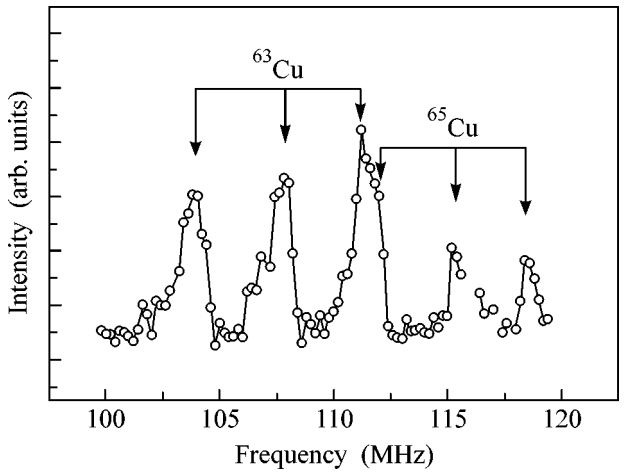

Fig. 1. Typical ^{63,65}Cu NMR spectrum of $SrCuO_2$ in the local field at $T = 295$ K. The relaxation times were measured at the frequencies corresponding to the central transition ($1/2 \longleftrightarrow -1/2$) for both copper isotopes.

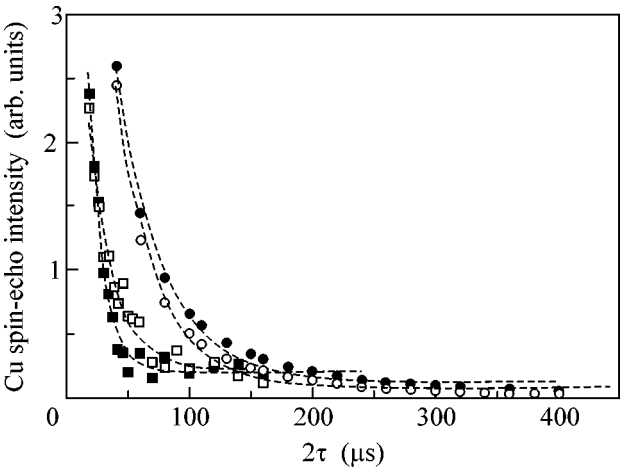

Fig. 2. Spin-echo signal amplitude for ^{63,65}Cu NMR in $SrCuO_2$ versus double delay of the second pulse at 295 K (■, ^{63}Cu; □, ^{65}Cu) and 4.2 K (●, ^{63}Cu; ○, ^{65}Cu). Dashed curves are data processing by least squares in the single-exponent approximation (see the text for explanations).

and ^{65}Cu ($I = 3/2$), with different gyromagnetic ratios and nuclear quadrupole moments allowed us to determine the main contributions to the relaxation rates in the entire temperature range from 4.2 to 361 K.

Peculiarities of the synthesis of the infinite-layer antiferromagnetic oxide $SrCuO_2$ with a tetragonal structure are described in detail elsewhere [6]. The x-ray diffraction measurements showed that the synthesized sample was single-phase and had the unit cell parameters $a = 3.9266(4)$ Å and $c = 3.4331(5)$ Å.

The NMR measurements were performed on a pulse phase-coherent spectrometer. The spin–spin (T_2) and spin–lattice (T_1) relaxation times were measured at the frequencies corresponding (at every temperature step) to the maximum of the central transition line ($1/2 \longleftrightarrow -1/2$) in the copper nuclei (^{63}Cu, ^{65}Cu). In order to obtain the maximum amplitude of the RF magnetic field H_1 in a coil with the sample and, hence, to decrease the $\pi/2$ pulse duration, we used an RF coil of minimum diameter (2.5 mm). The spin–spin relaxation time (T_2) was determined using the $\pi/2$–τ–π–echo pulse sequence. We analyzed the integral intensity of the spin echo signal proportional to the nuclear magnetization M. The spin echo decay was described by the function $M(\tau) = M_0\exp(-2\tau/T_2)$. The spin–lattice relaxation time (T_1) was determined using the inverted pulse sequence: π–t–$\pi/2$–τ–π–echo. The integral intensity of the spin echo signal in this case could be well described by the expression $1 - M(t)/M_0 = 0.9\exp(-6t/T_1) + 0.1\exp(-t/T_1)$ [10], which gave the T_1 value at each temperature step.

Figure 1 shows the characteristic room-temperature NMR spectrum of copper. Six lines in this spectrum are due to the presence of two isotopes, ^{63}Cu and ^{65}Cu. For each isotope, the spectrum consists of three lines representing the central transition line ($1/2 \longleftrightarrow -1/2$) and two quadrupole satellites ($\pm 3/2 \longleftrightarrow \pm 1/2$). The distance between these satellites determines the quadrupole frequency ν_Q proportional to the main component V_{ZZ} of the electric-field gradient tensor. Since the behavior of both V_{ZZ} and the position of the central line maximum was described in detail in [6], we will not dwell on this point here.

Figure 2 shows plots of the spin echo signal amplitude versus double delay of the second pulse. As can be seen, this dependence is satisfactorily described by the same exponent for both low and high temperatures. At the same time, the magnetization decays differently for various copper isotopes. The magnetization $M(\tau)$ exhibits a more rapid decay in the region of low temperatures for ^{65}Cu and at high temperatures for ^{63}Cu.

This character of the decay leads to a difference in the behavior of the transverse relaxation rate for the two isotopes (Fig. 3). The temperature dependence of T_2^{-1} can be divided into two parts: a low-temperature region (4.2–50 K), where the spin–spin relaxation time increases with temperature, and a high-temperature region (50–361 K), where T_2 is virtually independent of the temperature below 300 K and then increases as the temperature approaches T_N. In this respect (considering the results for ^{63}Cu), these data are very close to those reported for the isostructural SCCO compound [8]. However, considering the behavior of the relaxation for different isotopes, the data at $T \le 250$ K exhibit a substantial difference.

In this region, we have $^{63}T_2^{-1} < {}^{65}T_2^{-1}$ for the SCO, in contrast to the opposite relation ($^{63}T_2^{-1} > {}^{65}T_2^{-1}$) for the

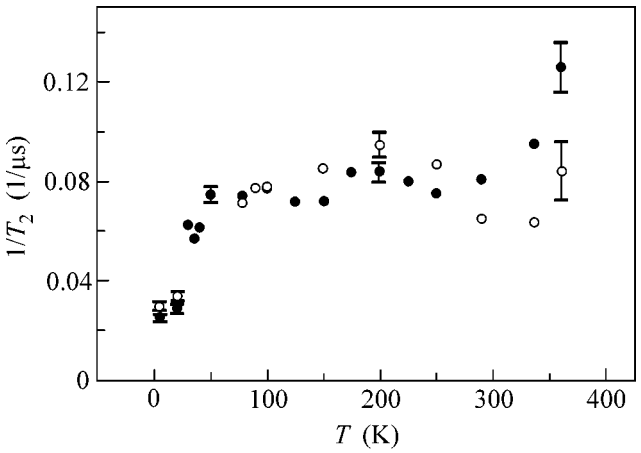

Fig. 3. Temperature dependence of the spin–spin relaxation rate for (●) ^{63}Cu and (○) ^{65}Cu in $SrCuO_2$.

SCCO [8]. In the high-temperature region ($T > 250$ K), the relation between the relaxation rates for the two isotopes coincides with that reported in [8].

The spin–spin relaxation rate can be represented as a sum of two contributions,

$$1/T_2 = 1/T_{2R} + 1/T_{2I}, \quad (1)$$

where $1/T_{2R}$ is the Redfield contribution related to fluctuations of the nuclear spin–lattice interaction [11] and $1/T_{2I}$ is the contribution due to the indirect interaction between nuclear spins. The contribution related to the direct dipole–dipole interaction [11] is very small (according to our estimates, not exceeding 3% of the relaxation rate) and will be ignored below.

If the first term dominates in Eq. (1), we may expect the following relation between the spin–spin relaxation times [8, 11]: $^{65}T_{2R}/^{63}T_{2R} = \gamma_{63}^2/\gamma_{65}^2 = 0.87$, where γ_{63} and γ_{65} are the corresponding gyromagnetic ratios. This very relation was observed (to within the experimental error) in our experiments in the low-temperature region (4.2–20 K). Therefore, we may suggest that the same mechanism determines the spin–lattice relaxation. If the second term dominates in Eq. (1), we have to expect another relation [12, 13]: $^nT_2^{-1} \sim \gamma_n^2 C^{0.5}$, where C is the native isotope content. This relation was observed in the region of high temperatures.

The spin–lattice relaxation rate exhibited nonmonotonic behavior (Fig. 4). In the temperature range $T >$ 150 K, this quantity weakly varied with the temperature (to within the experimental error). In contrast, at low temperatures, $1/T_1$ exhibited a well pronounced maximum at $T \sim 50$ K. Since the same maximum was observed for the isostructural compound SCCO [8], it would be expedient to relate this behavior to the diffusion of a small number of holes formed during the synthesis in the CuO_2 planes of the infinite-layer SCO.

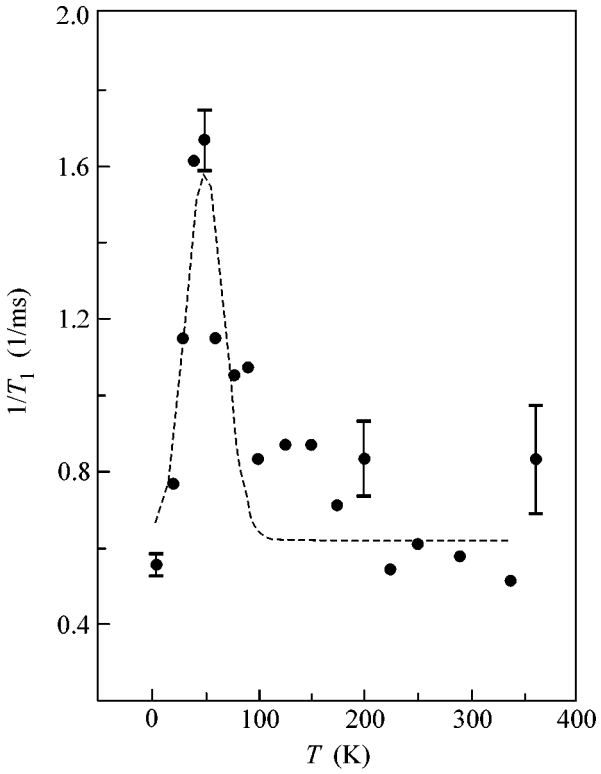

Fig. 4. Temperature dependence of the spin–lattice relaxation rate for the ^{63}Cu isotope in $SrCuO_2$. Dashed curve is data processing by least squares according to Eq. (2) (within the BPP model).

For the quantitative description of the behavior of the spin–lattice relaxation rate in the SCO, we use the Bloembergen–Purcell–Pound (BPP) model [14] and write the semiempirical expression

$$\frac{1}{T_1} = R_P + 2\gamma^2 h_\perp^2 \int_0^\infty G_{E_0,\Delta E}(E)\frac{\tau(E)}{1+\omega^2\tau^2(E)}dE. \quad (2)$$

Here, $G_{E_0,\Delta E}(E)$ is the Gaussian distribution of the activation energy, τ is the correlation time (according to the Arrhenius law, $\tau = \tau_0 \exp(E_0/kT)$, E_0 is the activation energy, ω is the NMR frequency, $h_\perp = h_x = h_y$ is the average amplitude of the fluctuating field in the direction perpendicular to the local field, and R_P is a temperature-independent contribution to the spin–lattice relaxation rate.

Upon fitting relation (2) to the experimental dependence, we obtained $\tau_0 \sim 1.3 \times 10^{-13}$ s for the characteristic time of the electron–electron correlations and $E =$ 42 meV, $\Delta E = 14$ meV, and $R_P = 620(250)$ s^{-1}. All the fitting parameters are rather close to the analogous values determined for the SCCO [8], which has to be expected for isostructural compounds with close hole densities. However, it should be noted that the somewhat higher activation energy, in our case, is evidence

of a higher degree of localization of the charge carriers in the SCO. The temperature-independent contribution R_p in $T_1^{-1}(T)$ is observed in most cases for low-doped cuprates [8, 15]. This contribution probably originates from the paramagnetic relaxation caused by localized moments in the defect structure of the high-pressure phase of the SCO. The hole density c in our case is directly proportional to the peak amplitude in the temperature dependence of the spin–lattice relaxation rate. For estimating this value by the order of magnitude, we can use the data for one SCCO sample [8] whose $T_1^{-1}(T)$ peak amplitude was close to that observed for the SCO, which yields $c \sim 10^{-4}$.

As was demonstrated above, the behavior of the transverse relaxation rate in the region of low temperatures is determined by the same mechanism as that for the spin–lattice relation. This mechanism is directly associated with the diffusion of a small number of holes in the CuO_2 planes. However, the expression for T_2^{-1}, according to the BPP model, differs from the expression for T_1^{-1} [11]:

$$\frac{1}{T_2} = \gamma^2\left[h_z^2\tau + h_\perp^2\frac{\tau}{1+\omega_0^2\tau^2}\right], \qquad (3)$$

where h_z is the average amplitude of the fluctuating field in the direction parallel to the local field. In this case, we may expect that T_2^{-1} will be temperature independent in the high-temperature range ($T > \sim 50$ K) and that it will decrease with decreasing temperature in the region of $T < 50$ K, in agreement with the observed behavior of $T_2^{-1}(T)$ (Fig. 3). This circumstance provides additional evidence in favor of the adopted model. The difference between the T_1^{-1} and T_2^{-1} magnitudes is explained by the possible anisotropy of fluctuations of the hyperfine field, whereby $h_z \gg h_\perp$.

In conclusion, we demonstrated that the infinite-layer antiferromagnet $SrCuO_2$ contains a small amount of holes, the motion of which primarily determines the low-temperature behavior of the relaxation rates. At the same time, the behavior of the spin–spin relaxation rate at high temperatures ($T > 250$ K) is determined by indirect interactions, which is similar to the behavior of this parameter in the isostructural compound $Sr_{0.15}Ca_{0.85}CuO_2$.

We are grateful to S.V. Verkhovskiĭ for fruitful discussions and valuable remarks. This study was supported by the Russian Foundation for Basic Research, project nos. 03-02-16673 and 02-03-32380.

REFERENCES

1. A. Lombardi, M. Mali, J. Roos, *et al.*, Phys. Rev. B **54**, 93 (1996).
2. T. Imai, C. P. Slichter, K. Yoshimura, *et al.*, Phys. Rev. Lett. **70**, 1002 (1993).
3. D. Brinkmann, J. Alloys Compd. **326**, 7 (2001).
4. K. Ishida, Y. Tokunaga, Y. Kitaoka, *et al.*, J. Phys. Soc. Jpn. **65**, 329 (1996).
5. K. Mikhalev, K. Kumagai, Y. Furukawa, *et al.*, Physica C (Amsterdam) **304**, 165 (1998).
6. K. Mikhalev, S. Verkhovskii, A. Gerashenko, *et al.*, Phys. Rev. B **69**, 132415 (2004).
7. E. A. Turov and M. P. Petrov, *Nuclear Magnetic Resonance in Ferro- and Antiferromagnets* (Nauka, Moscow, 1969; Wiley, New York, 1972).
8. F. Raffa, M. Mali, J. Roos, *et al.*, Phys. Rev. B **58**, 2724 (1998).
9. S. Chakravarty, M. P. Gelfand, P. Kopietz, *et al.*, Phys. Rev. B **43**, 2796 (1991).
10. A. Narath, Phys. Rev. **162**, 320 (1967).
11. C. P. Slichter, *Principles of Magnetic Resonance*, 3rd ed. (Springer, Berlin, 1990; Mir, Moscow, 1981).
12. C. H. Pennington, D. J. Durand, C. P. Slichter, *et al.*, Phys. Rev. B **39**, 274 (1989).
13. Y. Itoh, H. Yasuoka, Y. Fujiwara, *et al.*, Physica C (Amsterdam) **185–189**, 1223 (1991).
14. N. Bloembergen, E. M. Purcell, and R. V. Pound, Phys. Rev. **73**, 679 (1948).
15. K. R. Thurber, A. W. Hunt, T. Imai, *et al.*, Phys. Rev. Lett. **79**, 171 (1997).

Translated by P. Pozdeev

JETP Letters, Vol. 80, No. 8, 2004, pp. 544–547. Translated from Pis'ma v Zhurnal Éksperimental'noĭ i Teoreticheskoĭ Fiziki, Vol. 80, No. 8, 2004, pp. 619–622.

Visible Photoluminescence from Silicon Nanopowders Produced by Silicon Evaporation in a High-Power Electron Beam

M. D. Efremov[1], V. A. Volodin[1]*, D. V. Marin[1], S. A. Arzhannikova[1], S. V. Goryaĭnov[2], A. I. Korchagin[3], V. V. Cherepkov[3], A. V. Lavrukhin[3], S. N. Fadeev[3], R. A. Salimov[3], and S. P. Bardakhanov[4]

[1] *Institute of Semiconductor Physics, Siberian Division, Russian Academy of Sciences, pr. Akademika Lavrent'eva 13, Novosibirsk, 630090 Russia*

* *e-mail: volodin@isp.nsc.ru*

[2] *Institute of Mineralogy and Petrography, Siberian Division, Russian Academy of Sciences, Universitetskiĭ pr. 3, Novosibirsk, 630090 Russia*

[3] *Budker Institute of Nuclear Physics, Siberian Division, Russian Academy of Sciences, pr. Akademika Lavrent'eva 11, Novosibirsk, 630090 Russia*

[4] *Institute of Theoretical and Applied Mechanics, Siberian Division, Russian Academy of Sciences, ul. Institutskaya 4/1, Novosibirsk, 630090 Russia*

Received September 6, 2004

Silicon nanopowders produced by electron-beam-induced evaporation of a bulk silicon sample in an argon atmosphere are studied by the photoluminescence technique and Raman scattering spectroscopy. A photoluminescence peak in the visible region of the spectrum has been detected at room temperature in powders consisting of silicon nanocrystals. The strong short-wavelength shift of the photoluminescence peak can be attributed to the quantum size effect of electrons and holes in small silicon nanocrystals (about 2 nm). The size of silicon nanocrystals is determined by analyzing Raman spectra, and it is consistent with estimates obtained from photoluminescence data. © *2004 MAIK "Nauka/Interperiodica"*.

PACS numbers: 63.22.+m; 78.40.Fy; 78.55.–m; 81.15.–z

Interest in semiconductor nanocrystals is initiated by the possibility of modifying their electronic and optical properties determined by quantum size effects (band gap engineering). Starting with the pioneering studies performed in the early 1980s [1], a number of techniques have been developed for the production of semiconductor nanoclusters in a dielectric environment. Almost all of them are based either on the self-assembly of semiconductor nanoclusters in the course of thermal treatment of dielectrics or on the use of the controlled oxidation of semiconductor nanostructures. With the use of these techniques, which employ self-assembly effects, nanocrystals with a size of a few nanometers can be produced. We note that this limit cannot be achieved in modern lithography. Interest in silicon nanocrystals is primarily stimulated by the possibility of quasi-direct optical transitions in them as a result of *k*-space band folding due to the quantum size effect of electrons [2].

The optical properties of silicon nanocrystals formed in silicon dioxide films by various techniques are well understood [3–6]. The quantum size effect on the optical properties of such a heterostructure was directly demonstrated for a thin two-dimensional silicon layer (quantum well) surrounded by silicon dioxide [7]. A short-wavelength shift of the photoluminescence signal maximum was observed as the size of the nanocrystals decreased. With the release of excess silicon in SiO_x ($x < 2$), the average size of the nanocrystals can be slightly varied by changing either the concentration of excess silicon or the thermal treatment conditions [3–6]. However, stable silicon nanocrystals smaller than 3 nm cannot be produced using this approach likely due to a great surface contribution to the free energy of such nanocrystals. The minimum wavelength of the photoluminescence peak shifted to the short-wavelength region of the spectrum was as high as 700 nm.

Smaller clusters can be produced by using other approaches to the formation of silicon nanoclusters. Form this standpoint, the formation of silicon nanoparticles immediately in the course of plasma-chemical deposition [8, 9], as well as techniques based on the laser ablation of silicon [10], is promising. In this work, we applied an original radiation technique for forming silicon nanoparticles due to the evaporation of silicon ingots under the action of a high-power electron beam in an inert-gas (argon) atmosphere.

0021-3640/04/8008-0544$26.00 © 2004 MAIK "Nauka/Interperiodica"

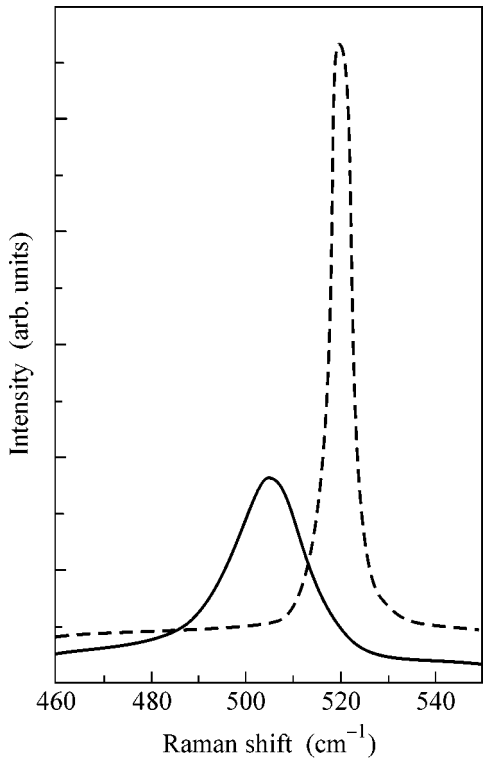

Fig. 1. Raman spectra of (dashed line) bulk silicon and (solid line) a silicon nanopowder prepared by electron-beam-induced evaporation.

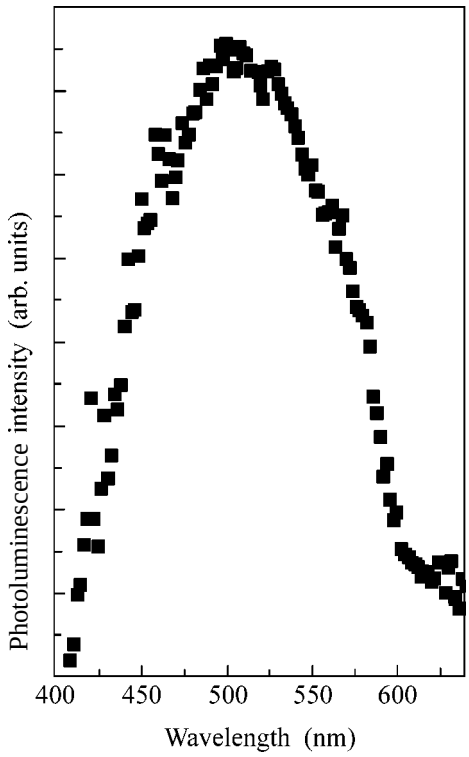

Fig. 2. Photoluminescence spectrum of a silicon nanopowder (excitation by a pulsed 337-nm N_2 laser at 300 K).

Silicon nanopowders were prepared with the use of an ELV-6 dc electron accelerator built at the Budker Institute of Nuclear Physics, Siberian Division, Russian Academy of Sciences. The accelerator was equipped with a system for extracting a beam into the atmosphere. The energy of irradiating electrons was 1.4 MeV. The power of the electron beam was sufficient to evaporate a bulk silicon sample in an argon atmosphere at a gas pressure slightly higher than atmospheric pressure. Silicon nanopowders were collected on a special filter and subsequently stored in an open atmosphere so that they might be coated with a silicon-oxide layer.

A pulsed N_2 laser (λ = 337 nm) was used to excite photoluminescence, and the spectra were measured by an SDL-1 spectrometer with an FEU-79 photomultiplier tube as a detector. Raman scattering spectra were obtained at room temperature by a DFS-52 spectrometer (using a 514.5-nm Ar-laser line) and a Dylor micro-Raman spectrometer. Quasi-backscattering geometry was used without analyzing the polarization of the incident and scattered light.

Raman spectroscopy, which is a rapid and nondestructive technique, combined with calculations, is highly informative for studying nanomaterials. The position of a Raman peak corresponding to scattering by localized optical phonons in nanocrystals depends on the size of the nanocrystals. Therefore, the average nanocrystal size can be determined by the convolution of the effective density of the states [11, 12]. Figure 1 shows the Raman spectrum of a silicon nanopowder (in the region of optical vibrations) in comparison with the spectrum of bulk silicon. As is seen, the former spectrum differs significantly from the latter one: the frequency is shifted, the intensity decreases, and the spectral line is broadened. The nanocrystal peak is shifted from the bulk-silicon peak toward lower frequencies, because the momentum selection rules become softer. Vibrational modes with nonzero wave vectors are manifested in the Raman spectra of nanocrystals. The frequency of these modes was lower than the frequency of long-wavelength optical phonons. The size of the nanocrystals was estimated in the approximation of the effective folding of vibrational modes. The model for calculating the average nanocrystal size from the position of a Raman peak corresponding to scattering by optical phonons was described in [11, 12]. A comparison between the experimental and calculated data shows that the average diameter of the silicon nanocrystals in the nanopowders is approximately equal to 2 nm. We note that our estimates are consistent with the calculated frequencies of the Raman-active localized optical phonons in the spherical clusters of crystalline silicon. These calculations were performed in the microscopic model of valence forces [13]. The Raman peak from the nanopowder is broadened due to both the

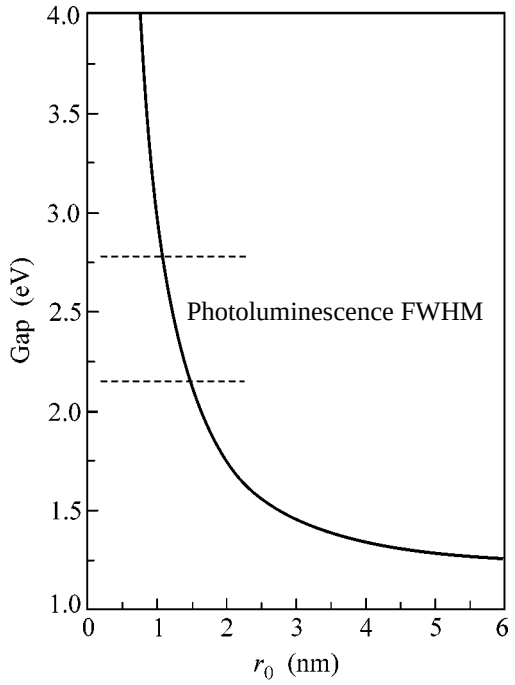

Fig. 3. Calculated optical gap in silicon nanocrystals.

increased anharmonicity in the nanocrystals, which reduces the lifetime of an optical phonon, and the size dispersion of the nanocrystals.

Figure 2 demonstrates the photoluminescence spectrum of the silicon nanopowder at room temperature. The photoluminescence spectrum exhibits a broad peak in the green region of the spectrum. The photoluminescence intensity maximum corresponds to 2.4 eV. Consequently, the difference between this maximum and the band gap of bulk silicon is equal to about 1.3 eV. This strong shift can be due to quantum size effects in the silicon nanocrystals. The large peak width is likely attributed to the size dispersion of the nanocrystals.

The energy levels of the localized states of the electrons and holes in the silicon nanocrystals were estimated in the simplest model of a spherically symmetric well. Calculations in this model were detailed in [12, 14]. The levels in the spherically symmetric well of radius r_0 with a barrier of height U_0 are found as follows [15]. The separation of variables leads to the following one-dimensional equation for the radial wave function with zero orbital angular momentum:

$$\frac{1}{r^2}\frac{\partial^2}{\partial r^2}(r^2\Psi(r)) - \frac{2m(r)}{\hbar^2}(E - U(r))\Psi(r) = 0.$$

Being localized, the electron states in the conduction band with wave vectors both along and across the ⟨100⟩ crystallographic directions are mixed. Therefore, in accordance with the approach proposed by Burdov [14], we take the effective electron mass $m_e = 0.26$ and the effective hole mass $m_h = 0.19$ in the units of the free electron mass. The solution for the finite barrier (in this case, the SiO_2 barrier is considered) is found by matching the wave function and its derivative at the boundary. The corresponding equations are solved numerically with consideration for the mass gap in the well and barrier. Figure 3 shows the results of the calculations, which are consistent with the experimental data (the dashed straight lines indicate the experimental FWHM for the photoluminescence peak). Thus, the photoluminescence signal detected in the green region of the spectrum in silicon nanopowders at room temperature can be attributed to quantum size effects, as in the case of the Si nanocrystal–SiO_2 matrix heterosystem.

In conclusion, we discuss the advantages of the technique chosen for the formation of nanopowders over the currently available techniques. The first advantage is the potentially high productivity of this technique. Thus, the efficiency of the techniques using laser ablation [10] is determined by the average laser power, which is limited to a few kilowatts even in state-of-the-art lasers. At the same time, the electron-beam power in an accelerator can be as high as 100 kW. The second advantage is that the size of the silicon nanoparticles can be regulated *ex situ* by controlled surface oxidation. The third advantage is the potential possibility of separating the nanoparticles by their size. This possibility is of paramount importance for potential applications. One of these applications (along with optoelectronic devices) is the development of memory elements based on silicon nanocrystals with the possibility of superdense packing [9].

We are grateful to Academician V.M. Buznik (Russian Academy of Sciences) for fruitful discussions of the results and helpful remarks. This work was supported in part by the Siberian Division of the Russian Academy of Sciences (interdisciplinary integration project no. 159).

REFERENCES

1. A. I. Ekimov and A. A. Onushchenko, Pis'ma Zh. Éksp. Teor. Fiz. **34**, 363 (1981) [JETP Lett. **34**, 345 (1981)].
2. D. Kovalev, H. Heckler, M. Ben-Chorin, *et al.*, Phys. Rev. Lett. **81**, 2803 (1998).
3. T. T. Shimizu-Iwayama, K. Fujita, S. Nakao, *et al.*, J. Appl. Phys. **75**, 7779 (1994).
4. G. A. Kachurin, S. G. Yanovskaya, V. A. Volodin, *et al.*, Fiz. Tekh. Poluprovodn. (St. Petersburg) **36**, 685 (2002) [Semiconductors **36**, 647 (2002)].
5. G. A. Kachurin, I. E. Tyschenko, V. Skorupa, *et al.*, Fiz. Tekh. Poluprovodn. (St. Petersburg) **31**, 730 (1997) [Semiconductors **31**, 626 (1997)].
6. D. Nesheva, C. Raptis, A. Perakis, *et al.*, J. Appl. Phys. **92**, 4678 (2002).
7. Eun-Chel Cho, M. A. Green, J. Xia, *et al.*, Appl. Phys. Lett. **84**, 2286 (2004).

8. N.-M. Park, C.-J. Choi, T.-Y. Seong, *et al.*, Phys. Rev. Lett. **86**, 1355 (2001).
9. M. L. Ostraat, J. W. De Blauwe, M. L. Green, *et al.*, Appl. Phys. Lett. **79**, 433 (2001).
10. G. Ledoux, *Trends in Nanotechnology Research. Photoluminescence Properties of Silicon Nanocrystals Synthesized by Laser Pyrolysis* (Nova Sci., New York, 2004).
11. V. Paillard and P. Puech, J. Appl. Phys. **86**, 1921 (1999).
12. V. A. Volodin, E. B. Gorokhov, M. D. Efremov, *et al.*, Pis'ma Zh. Éksp. Teor. Fiz. **77**, 485 (2003) [JETP Lett. **77**, 411 (2003)].
13. Wei Cheng and Shang-Fen Ren, Phys. Rev. B **65**, 205305 (2002).
14. V. A. Burdov, Fiz. Tekh. Poluprovodn. (St. Petersburg) **36**, 1233 (2002) [Semiconductors **36**, 1154 (2002)].
15. L. D. Landau and E. M. Lifshitz, *Course of Theoretical Physics*, Vol. 3: *Quantum Mechanics: Non-Relativistic Theory*, 4th ed. (Nauka, Moscow, 1989; Pergamon, New York, 1977).

Translated by V. Makhlyarchuk

JETP Letters, Vol. 80, No. 8, 2004, pp. 548–551. Translated from Pis'ma v Zhurnal Éksperimental'noĭ i Teoreticheskoĭ Fiziki, Vol. 80, No. 8, 2004, pp. 623–626.

Ab Initio Calculations of the Superconducting Transition Temperature for NbC at Various Pressures

E. G. Maksimov[1, *], M. V. Magnitskaya[2], S. V. Ebert[1], and S. Yu. Savrasov[3]

[1] *Lebedev Physical Institute, Russian Academy of Sciences, Moscow, 119991 Russia*

[2] *Institute of High Pressure Physics, Russian Academy of Sciences, Troitsk, Moscow region, 142190 Russia*

[3] *New Jersey Institute of Technology, Newark, New Jersey 07102, USA*

**e-mail: maksimov@lpi.ru*

Received September 4, 2004

Ab initio calculations of the superconducting properties have been performed for niobium carbide (NbC) at normal pressure and upon a 15 and 30% compression. Factors accounting for the relatively low values of the transition temperature T_c in transition metal carbides are considered and the possible ways of increasing this parameter are discussed. © *2004 MAIK "Nauka/Interperiodica".*

PACS numbers: 63.20.–e; 74.25.–q; 74.62.Fj; 74.70.Ad

According to the Bardeen–Cooper–Schrieffer (BCS) theory, the maximum critical temperature T_c of the superconducting transition might be observed in metals possessing minimum atomic masses M, since this theory predicts that $T_c \sim 1/M^{1/2}$. For this reason, much attention was devoted for many years to the possible superconductivity of metallic hydrogen (see, e.g., review [1]). The results of our recent *ab initio* calculations [2] showed that metallic hydrogen at ultrahigh pressures ($p \sim 20$ Mbar) might actually be a superconductor with $T_c \sim 600$ K. Unfortunately, not only practical use but even the synthesis of superconducting metallic hydrogen at such pressures is impossible. The possibility of reaching high T_c values was previously also considered for metal hydrides. Recently, Ashcroft [3] returned to this problem in the context of the revival of the general interest in searching for new high-T_c compounds exhibiting superconductivity in the intermediate temperature range.

In addition to metal hydrides, of considerable interest from the standpoint of reaching high T_c values are transition metal borides, carbides, nitrides, and oxides, because they are also characterized by quite high frequencies of optical phonons associated predominantly with the vibrations of light atoms. One of such compounds, possessing a relatively high transition temperature ($T_c \sim 40$ K), is magnesium diboride (MgB_2) [4], in which superconductivity is primarily due to the interactions between optical vibrations and electrons localized at the boron sites. As is known, T_c depends both on the atomic mass and, which is even more significant, on the constant of the electron–phonon interaction for a given phonon mode.

In this context, we apply the methods of *ab initio* calculations reported in [5, 6] to study superconductivity in niobium carbide (NbC) so as to elucidate the causes for the relatively low critical temperature ($T_c \sim 11$ K) and to determine the T_c change with increasing pressure.

Previously, transition metal carbides and nitrides were also considered as potential high-T_c materials [7, 8]. In these investigations, the electron–phonon interaction constants for these materials were qualitatively assessed and it was shown that $T_c \approx 30$ K might be expected in MoN. However, the calculations were performed for stoichiometric MoN with a structure of the NaCl type. Unfortunately, such a structure is never realized for the stoichiometric composition and can be stable only in MoN_{1-x} with $x \geq 0.3$.

Complete microscopic calculations of the electron and phonon spectra of transition metal carbides and nitrides and their electron–phonon interaction constants were almost not performed because of considerable difficulties. One of a few examples is offered by *ab initio* calculations of the phonon spectra of NbC [9] by the full-potential linear muffin-tin orbital method (FP-LMTO) [5]. In the present study, calculations were performed (like those in [2, 6, 9]) using the program package implementing the FP-LMTO method as described in [5].

Figure 1 shows the density of states (DOS) $N(E)$ calculated for NbC at $V = V_0$ (V_0 is the specific volume at atmospheric pressure) and at $V = 0.85V_0$ and $0.70V_0$ (that is at a 15 and 30% lattice compression, respectively). The compressibility of NbC is relatively small (the bulk modulus is $K_{NbC} = 340$ GPa) and these compressions correspond to a pressure of $p \sim 0.6$ and 1.5 Mbar, respectively. In Fig. 1, the $N(E)$ peak at an energy of ~0.2 Ry above the Fermi level (E_F) is due to the unoccupied Nb 4*d* states. The peak at ~0.3 Ry below E_F is mostly due to the C 2*p* states hybridized

with the occupied Nb 4*d* states. A structure in the region of energies about –1 Ry is formed by the so-called "semi-core" 4*p* states of niobium. At normal pressure, the shape of $N(E)$ agrees well with the results of previous DOS calculations for NbC [7, 8]. As can be seen from Fig. 1, it is most likely that an increase in pressure reduces T_c, because $N(E)$ at the Fermi level decreases in this case.

We have also calculated the phonon spectra $\omega(\mathbf{q})$ and the spectral density of the electron–phonon interaction (the Eliashberg function) for NbC in all the cases under consideration. The Eliashberg function $\alpha^2(\omega)F(\omega)$ for NbC at various pressures is shown in Fig. 2. The phonon DOS is not depicted in this figure because the shape of this curve is very similar to that of $\alpha^2(\omega)F(\omega)$. As is seen in Fig. 2, the Eliashberg function (as well as the phonon DOS) consists of two peaks significantly spaced on the frequency scale. The low-frequency peak describes the interaction of electrons with acoustic phonons, while the high-frequency peak refers to the interaction with optical phonons. The coupling constants for the corresponding phonons were calculated using the formula

$$\lambda_{ph} = 2\int_{\omega_1}^{\omega_2}\frac{d\omega}{\omega}\alpha^2(\omega)F(\omega). \quad (1)$$

Integrating in Eq. (1) from $\omega_1 = 0$ to $\omega_2 = 14$ THz (see Fig. 2), we obtain the constant of coupling with the acoustic phonons (λ_{ac}). At normal pressure and 15 and 30% compressions, this calculation yields $\lambda_{ac} = 0.71$, 0.50, and 0.35, respectively; the constants of coupling with the optical phonons at the same pressures are much lower: $\lambda_{op} = 0.21$, 0.19, and 0.16, respectively.

Within the framework of the simple "rigid muffin-tin" approximation used in the early investigations [7, 8], the coupling constant λ for binary compounds AB with substantially different ion masses can be expressed as

$$\lambda = \lambda_{ac} + \lambda_{op} = \frac{N_A(0)\langle I_A^2\rangle}{M_A\langle\omega_A^2\rangle} + \frac{N_B(0)\langle I_B^2\rangle}{M_B\langle\omega_B^2\rangle}, \quad (2)$$

where $N(0)$ is the DOS at the Fermi level and $N(0)\langle I^2\rangle$ is the Hopfield parameter [10], which is proportional to the square of the matrix element of the electron–phonon interaction integrated over the Fermi surface. According to estimates [11], carbides obey the relation

$$M_A\langle\omega_A^2\rangle \cong M_B\langle\omega_B^2\rangle. \quad (3)$$

The Hopfield parameter for Nb and C atoms was also calculated in [11], where the value for carbon has proved to be less than half of that for niobium. We have performed more precise calculations, which showed that, first, the constant of coupling with the optical modes is less than one-third of that for the acoustic modes and, second, our values of the constant of coupling with the acoustic modes are about twice as large as those obtained in [11]. Qualitatively, the smaller values of λ_{op} obtained in [11] and in our calculations are explained by a low DOS for the carbon-bound electrons on the Fermi surface. The chemical bonds in NbC are predominantly ionic: electrons from Nb pass to the C 2*p* states occurring 0.3–0.35 Ry (4–5 eV) below the Fermi level, and only small tails of these states emerge at the Fermi surface.

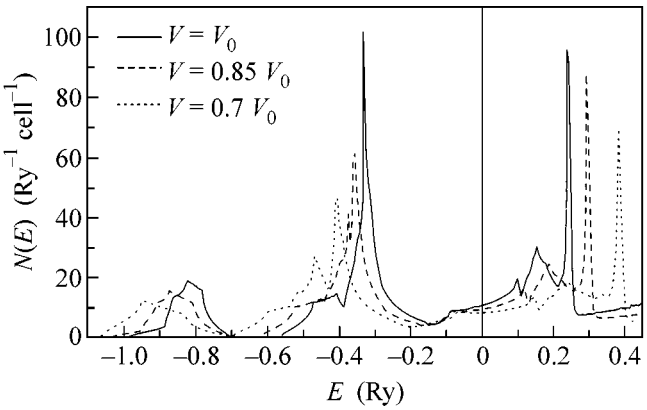

Fig. 1. DOS profiles $N(E)$ for NbC at normal pressure and upon 15 and 30% compression ($p \sim 0.6$ and 1.5 Mbar, respectively). V_0 is the equilibrium specific volume at $p \approx 0$. The energy is measured relative to the Fermi level.

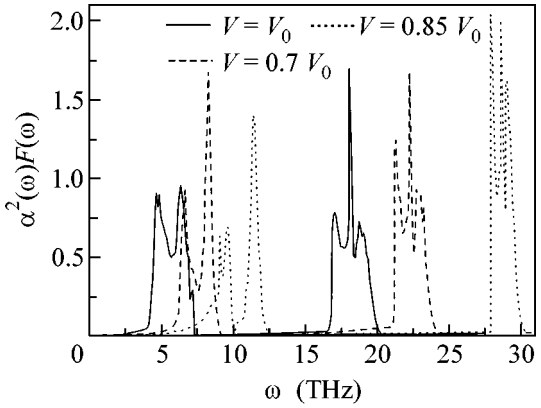

Fig. 2. Eliashberg function $\alpha^2(\omega)F(\omega)$ for NbC at normal pressure ($p \approx 0$) and upon 15 and 30% compression.

According to the results of our calculations, an increase in the pressure leads to a decrease in the DOS $N_{Nb}(0)$ associated with the niobium states at the Fermi level, while the DOS $N_C(0)$ associated with the carbon states at the Fermi level remains virtually unchanged. Increasing pressure leads to a sharp increase in the phonon frequency in both optical and acoustic branches. For a compression corresponding to $V = 0.7V_0$, the $M\langle\omega^2\rangle$ value increases by a factor of 2.5 and

2.3 for the optical and acoustic modes, respectively. At the same time, the coupling constant λ_{op} exhibits only a 25% decrease rather than a severalfold drop, as it might be expected from formula (2) for $\langle I^2 \rangle$ = const. This behavior implies that the growth of the pressure is accompanied by an increase in the matrix element of the electron–phonon interaction at the carbon atom. The acoustic coupling constant is halved; that is, it decreases approximately to the same extent to which the $M_{Nb}\langle \omega_{Nb}^2 \rangle$ value increases.

The superconducting transition temperature T_c can be determined by solving the Eliashberg equation [12] with the known function $\alpha^2(\omega)F(\omega)$. With neglect of the Coulomb repulsion, these calculations give T_c = 15.7 K for NbC. However, such *ab initio* calculations do not allow the Coulomb contribution to T_c to be estimated. For this reason, we have determined the Coulomb pseudopotential μ^* from the condition of coincidence of the calculated and experimental T_c values (T_c^{exp} = 11.1 K), which yields μ^* = 0.15. This value is likely to be somewhat overstated, since our calculations were performed for the stoichiometric NbC, while the real compound usually exhibits a deficiency of carbon. It is also known [7] that the transition temperature in NbC_{1-x} quite rapidly drops with increasing x. According to the results of our calculations, T_c also decreases rapidly with increasing pressure: T_c = 4.9 K for a 15% compression and T_c = 0.98 K for a 30% compression (the calculations were performed for the same pseudopotential μ^* = 0.15).

The good accuracy of our calculations of the Eliashberg function and coupling constants is confirmed by the following fact. We have calculated the transport Eliashberg function $\alpha_{tr}^2(\omega)F(\omega)$ and the electron–phonon interaction contribution to the resistivity ρ of NbC (the method of calculation is described in [5, 6]). At room temperature (T = 273 K), the calculated resistivity is ρ = 18.1 $\mu\Omega$ cm. The measurements of resistivity for a nearly stoichiometric niobium carbide $NbC_{0.98}$ [13] showed a rather high residual value of ρ_0 = 24 $\mu\Omega$ cm. When the temperature was changed from low values to 300 K, the resistivity increment amounted to ρ_{ph} = 15.5 $\mu\Omega$ cm. This value is very close to the result of our calculation (the difference is less than 20%). Taking into account that, for such a high value of ρ_0, Matthiessen's rule of the simple additivity of the residual and temperature-related contributions to the resistivity may itself be violated to within 20%, the obtained agreement between the calculated and experimental values of the resistivity can be considered as quite satisfactory.

Returning to our analysis of the possibility of reaching relatively high T_c values in transition metal carbides, it is possible to describe the situation as follows. According to formula (2), the electron–phonon interaction constant is determined to a considerable extent by the DOS at the Fermi level. For ZrC, NbC, MoC, and MoN systems with a cubic structure, $N(E)$ is well described using the "rigid band" approximation [14], that is, by simply shifting the Fermi level position. In ZrC, the number of electrons per unit cell is lower by one than that in NbC and, accordingly, the Fermi level is situated approximately 0.15 Ry (about 2 eV) lower and falls within a minimum in the DOS (see Fig. 1). In agreement with this picture, ZrC is not a superconductor. In NbN, where the number of valence electrons is greater by one than that in NbC, the Fermi level shifts rightward to higher DOS values. Accordingly, this compound is characterized by a higher transition temperature (T_c = 17 K). In MoN, E_F shifts rightward to an even greater extent, since the number of electrons per unit cell is greater by two than that in NbC. The DOS at the Fermi level in MoN is almost twice that in NbC. As was noted above, in accordance with the estimates obtained in [7], the transition temperature in MoN must be on the order of 30 K, although the experimental value is much lower. The fact is that this compound was never obtained with the stoichiometric composition and real samples always exhibited a deficiency of nitrogen. It was pointed out [14] that the cubic MoN phase is dynamically unstable and only the presence of nitrogen vacancies can stabilize this phase.

An even a more promising way of obtaining high T_c values would be the synthesis of carbides having the number of electrons per unit cell smaller by one than that in ZrC. An example could be offered by yttrium carbide with a structure of the NaCl type, where a situation (now purely hypothetical) might take place in which the Fermi level would fall within a peak in the DOS at 0.33 Ry (~4.5 eV) below E_F in NbC. In this energy region, the DOS is already sufficiently high, but it is even more important that, after such a rigid energy shift, the C 2*p* states strongly hybridized with the Y 5*d* states emerge directly at the Fermi level. However, it should be taken into account that it is the high value of $N(0)$ in MoN [14] that accounts for the instability of the cubic phase of this compound. In all probability, a cubic structure of the NaCl type is not more readily achieved in the stoichiometric YC. Moreover, a high concentration of carbon vacancies renders yttrium carbide either a poor metal (with a low density of carriers) or even a semiconductor [15].

It should be noted that, nevertheless, these are yttrium carbides in which record high T_c values have been observed. In particular, the transition temperature in Y_2C_3 is 18 K [16], while that in yttrium borocarbides reaches a level of 15–23 K [17]. In any case, the search for superconductors with relatively high T_c values (~40–50 K) among the compounds of metals with light elements is very interesting from the basic standpoint and important for practical applications.

At present, there are quite realistic projects for using the superconducting compound MgB_2, which offers considerable technological advantages in comparison,

for example, with high-T_c cuprates. Metal nitrides and carbides may be even more promising materials in this respect, provided that samples with transition temperatures on the order of ~40 K will be synthesized.

This work was supported by the Council of the President of the Russian Federation for Support of Young Russian Scientists and Leading Scientific Schools; Presidium of the Russian Academy of Sciences; Branch of General Physics and Astronomy, Russian Academy of Sciences; the Netherlands Organization for Scientific Research jointly with the Russian Foundation for Basic Research (NWO–RFBR grant no. 047.016.005); and the Russian Foundation for Basic Research (project nos. 02-02-16658 and 04-02-16061). All calculations were performed on the computers of the Joint Supercomputer Center, Russian Academy of Sciences.

REFERENCES

1. E. G. Maksimov and Yu. I. Shilov, Usp. Fiz. Nauk **169**, 1223 (1999) [Phys. Usp. **42**, 1121 (1999)].
2. E. G. Maksimov and D. Yu. Savrasov, Solid State Commun. **119**, 569 (2001).
3. N. W. Ashcroft, Phys. Rev. Lett. **92**, 187002 (2004).
4. J. Nagamatsu, N. Nagakawa, N. Muranaka, *et al.*, Nature **410**, 63 (2001).
5. S. Yu. Savrasov and D. Yu. Savrasov, Phys. Rev. B **46**, 12181 (1992).
6. E. G. Maksimov, S. Yu. Savrasov, and D. Yu. Savrasov, Usp. Fiz. Nauk **167**, 337 (1997) [Phys. Usp. **40**, 317 (1997)].
7. W. E. Pickett, B. M. Klein, and D. A. Papaconstantopoulos, Physica (Amsterdam) **108**, 667 (1981); D. A. Papaconstantopoulos, W. E. Pickett, B. M. Klein, *et al.*, Nature **308**, 494 (1984).
8. Y. Zho and S. Hes, Solid State Commun. **45**, 281 (1983).
9. S. Yu. Savrasov, Phys. Rev. B **54**, 16470 (1996).
10. J. J. Hopfield, Phys. Rev. **86**, 443 (1969).
11. B. M. Klein and D. A. Papaconstantopoulos, Phys. Rev. Lett. **32**, 1193 (1974).
12. G. M. Éliashberg, Zh. Éksp. Teor. Fiz. **39**, 1437 (1961) [Sov. Phys. JETP **12**, 1000 (1961)].
13. C. Y. Allison, F. A. Modine, and R. H. French, Phys. Rev. B **35**, 2573 (1987).
14. L. Gus, W. Hart, and B. M. Klein, Phys. Rev. B **61**, 3151 (2000).
15. T. Ya. Kosolapova, *Structure, Production, and Application of Refractory Carbides* (Metallurgizdat, Moscow, 1986) [in Russian].
16. G. Amano, S. Akutagawa, T. Muranaka, *et al.*, J. Phys. Soc. Jpn. **73**, 530 (2004).
17. R. J. Cava, H. Takagi, N. W. Zandbergen, *et al.*, Nature **367**, 252 (1994).

Translated by P. Pozdeev

JETP Letters, Vol. 80, No. 8, 2004, pp. 552–556. Translated from Pis'ma v Zhurnal Éksperimental'noĭ i Teoreticheskoĭ Fiziki, Vol. 80, No. 8, 2004, pp. 627–632.

Phonon Condensation in Quasi-One-Dimensional Atomic Gases with Time-Dependent Parameters

L. A. Manakova

Russian Research Centre Kurchatov Institute, pl. Akademika Kurchatova 1, Moscow, 123182 Russia

e-mail: manakova@kurm.polyn.kiae.su

Received July 23, 2004; in final form, September 23, 2004

It has been shown that, if the amplitude of uniform time-periodic variation in the density of a quasi-one-dimensional Bose gas exceeds a certain critical value, interactions between acoustic phonons lead to the formation of the condensate of correlated phonon pairs with energy equal to half the frequency of the gas-density oscillations. © *2004 MAIK "Nauka/Interperiodica".*

PACS numbers: 03.75.Fi; 05.30.Jp; 67.40.Db

1. Recently, interest in low-dimensional systems including one-dimensional systems is refreshed in connection with the creation of degenerate quantum gases in quasi-one-dimensional magnetic and optical traps. In particular, atomic Bose condensates were obtained in strongly anisotropic quasi-1D traps (see, e.g., [1], review [2] and references cited therein). The properties of quantum 1D gases upon time variation in their parameters (density or scattering length) are of great interest. In the experiment reported in [3], a magnetic-field-induced change in the frequency of the transverse parabolic potential in a strongly anisotropic cylindrical trap gave rise to radial (transverse) oscillations of the condensate as a whole. As was shown in [4], transverse oscillations of the condensate are responsible for periodic variation in the speed of sound and, as a consequence, the parametric resonance, which leads to the energy transfer to the subsystem of longitudinal (acoustic) modes. In addition, mechanisms of damping of the transverse mode that were attributed to the parametric resonance at zero temperature $T = 0$ were also considered in [4].

Uniform time-periodic variation in the Bose-gas parameters (density, the scattering length or, equivalently, the speed of sound) leads to the generation of pairs of acoustic phonons with opposite momenta. For definiteness, let us consider the Bose gas with time-dependent density that oscillates with an amplitude exceeding a certain critical value. In this case, the occupation numbers of acoustic phonons with energy equal to half the density-oscillation frequency (i.e., under the parametric-resonance condition) begin to increase exponentially in time. It is natural to assume that interactions between phonons become significant in this case. As will be shown below, interactions between phonons (anharmonisms), including phase-dependent interactions in 1D systems, are caused by (i) density fluctuations (along with phase fluctuations) in the kinetic energy of the 1D Bose gas and (ii) nonzero-range interaction between atoms in the 1D system (compared to zero-range interaction in a 3D system). We note that mechanisms of the appearance of anharmonisms and their role in the formation of the ground state have not yet been discussed in works devoted to 1D systems. Near the parametric resonance for $T = 0$, the coherent state of acoustic phonons is formed due to interactions. The phases of phonons with opposite momenta correlate in this state. Thus, the condensate of correlated phonon pairs is formed near half the frequency of the density oscillations in the Bose gas. This quantity serves as the chemical potential for acoustic phonons in this problem. Owing to the existence of phonon pairs, the density-oscillation amplitude is renormalized so that the occupation numbers of acoustic phonons reach steady-state values. In a certain region of the parameters, the condensation of phonon pairs provides a gap in the phonon spectrum for the wavenumber proportional to the density-oscillation frequency. In the new state, the stationary periodic modulation of the longitudinal density of the Bose gas occurs with an amplitude determined by the number of phonon pairs.

2. Let us consider mechanisms of the time modulation of the parameters of the Bose gas and the corresponding instability. In the absence of time modulation, the original Hamiltonian of the 1D Bose gas with interaction has the well-known form

$$H_{\rm B} = \frac{\hbar^2}{2m}\int dx\partial_x\Psi^+(x)\partial_x\Psi(x)$$

$$+\frac{1}{2}\int dxdx'\rho(x)U(x-x')\rho(x') + \int dxV(x)\rho(x), \quad (1)$$

$$\rho(x) = \Psi^+(x)\Psi(x); \quad [\Psi(x), \Psi^+(x')] = \delta(x-x').$$

0021-3640/04/8008-0552$26.00 © 2004 MAIK "Nauka/Interperiodica"

Here, $\Psi^+(x)$ and $\Psi(x)$ are the boson creation and annihilation operators for the atoms, $V(x)$ is the external potential, and $U(x-x')$ is the potential of the two-particle interaction between the atoms. Hamiltonian (1) means that we consider the gas in a strongly anisotropic trap whose longitudinal size is much larger than its transverse radius. The 1D model requires two conditions: $T \ll \omega_\perp$ and $\mu < \omega_\perp$, where $\omega_\perp$ is the transverse frequency of the trap and μ is the chemical potential of the Bose gas. In what follows, the gas in a box with the length $\mathcal{L}$ and the periodic boundary conditions are considered for simplicity. We emphasize that the phonon condensation proposed in this work is independent of the type of the boundary conditions (periodic or open). It is convenient to describe the 1D system by the phase and density operators [5]. In this representation, the boson field operator $\Psi^+(x)$ is written as

$$\Psi^+(x) = \sqrt{\rho(x)}e^{-i\theta(x)}; \quad \rho(x) = n + \frac{\partial_x\phi(x)}{\pi}; \qquad [\partial_x\phi(x), \theta(y)] = i\pi\delta(x-y). \tag{2}$$

In [5], the acoustic spectrum is obtained if density fluctuations are ignored in the kinetic energy; i.e., if $\rho(x) \approx n$ is substituted into Eq. (2). In this case, Eq. (1) takes the form of the known Hamiltonian of the Luttinger model

$$H_B = \frac{\hbar}{2\pi}\int dx[v_J(\partial_x\theta)^2 + v_N(\partial_x\phi)^2]; \qquad v_N = \frac{\partial_n\mu}{\pi\hbar}; \quad v_J = \frac{\pi\hbar n_s}{m}. \tag{3}$$

Here, n_s and $n = N/\mathcal{L}$ are the superfluid and total average densities in the ground state of the Bose gas, respectively, and N is the total particle number. The speed of sound is defined as $c_s = \sqrt{v_J v_N}$. If one defines the operators $\phi(x)$ and $\theta(x)$ in the form

$$\phi(x) = \frac{1}{2}\sum_{k\neq 0}\sqrt{\frac{2\pi}{\mathcal{L}|k|}}e^{-\delta|k|/2}(b_k^+e^{-ikx} + b_k e^{ikx}); \qquad \theta(x) = \frac{1}{2}\sum_{k\neq 0}\sqrt{\frac{2\pi}{\mathcal{L}|k|}}e^{-\delta|k|/2}\mathrm{sgn}(k)(b_k^+e^{-ikx} + b_k e^{ikx}), \tag{4}$$

$[b_k, b_k^+] = 1$, then it is easy to see that Hamiltonian (3) corresponds to the inclusion of all the terms that are bilinear in the operators $b_{\pm k}$ and $b_{\pm k}^+$. [In Eq. (4), so-called zero modes that are not necessary in this problem are omitted.]

Mechanisms of the generation of phonon pairs by means of the time modulation of the Bose-gas parameters are attributed to external-field-induced change in the coefficients of the bilinear terms $b_k^+b_{-k}^+$ in both the first and second terms of Hamiltonian (3). These are the Bose-gas density in the first term and the scattering length a in the second term, $U(x-x') = U\delta(x-x')$, $U = 4\pi\hbar^2a/m$. Assuming that $n_s \approx n$ for $T = 0$, we introduce the uniform density modulation $n = n_0 + n_1(t)$, where $n_1(t) \sim \exp(-i\omega_0 t)$. This mechanism can be realized by the corresponding time variation in the magnetic-trap potential, and it is equivalent to the introduction of the term $\int dx\psi^+(x)V(t)\psi(x)$ into original Hamiltonian (1) of the 1D Bose gas. Taking the usual expression $\psi(x) = \psi_0(x) + \delta\hat{\psi}(x)$, where $\delta\hat{\psi}(x) = \sum_k[u_k(x)b_k + v_k(x)b_{-k}^+]$, we obtain the term $\int dx\delta\hat{\psi}^+(x)V(t)\delta\hat{\psi}(x)$ responsible, in particular, for the generation of excitation pairs. Near the Feshbach resonance, the time modulation of the magnetic field can provide periodic time variation in the scattering length, which also results in the generation of phonon pairs in the 1D Bose gas. As is known [6], $a = a(B)$, where B is the magnetic field, in this region. Taking $B = B_0 + B_1(t)$, where $B_1(t) \sim \exp(-i\omega_0 t)$, we obtain $a_1(t) \sim \exp(-i\omega_0 t)$. Both mechanisms contribute to the Hamiltonian as

$$H_p = \frac{1}{2}\sum_k(E_0e^{-i\omega_0 t}b_k^+b_{-k}^+ + \mathrm{H.c.}). \tag{5}$$

Here, E_0 is proportional to the amplitude of the time-dependent parameter of the Bose gas (this quantity can generally be complex). Only terms important for further consideration are retained in Eq. (5). In this work, we analyze the case where E_0 is a given value. For definiteness, we treat E_0 as the density oscillation amplitude for the entire Bose gas. The total Hamiltonian of the problem has the form $H = H_B + H_p + H_{int}$, where H_B and H_p are defined in Eqs. (3) and (5), respectively, and the interactions H_{int} between phonons are disregarded in "harmonic" approximation (3). However, the last interactions can be essential for determining the system state if the amplitude n_0 exceeds the critical value. These interactions will be defined later. Hamiltonian (3) is diagonalized by the canonical transformation $\phi(x) = \sqrt{K}\,\phi'(x)$, $\theta(x) = (1/\sqrt{K})\theta'(x)$, and $K = \sqrt{v_J/v_N} = e^{2\xi}$, so that we arrive at the following Bose-gas Hamiltonian with the acoustic spectrum:

$$H_B = \sum_{k\neq 0} c_s|k|\tilde{b}_k^+\tilde{b}_k. \tag{6}$$

Since $H_p \longrightarrow \tilde{H}_p = (1/2)\sum_k[\tilde{E}_0\exp(-i\omega_0 t)\tilde{b}_k^+\tilde{b}_{-k}^+ + \mathrm{H.c.}]$ + [nonresonant terms] in the new representation and the interactions also conserve their forms, the tilde sign will be omitted in the operators and coefficients for simplicity. The system described by the Hamiltonian $H_0 = H_B + H_p$, where H_{int} is disregarded, has instability due to the paramagnetic resonance. Indeed, the equations of motion for

Heisenberg operators, $i(\partial b_k/\partial t) = [H, b_k]$, disregarding H_{int} are written in the form

$$\left[\frac{d}{dt} + \gamma_k + i(\omega_k - \omega_0/2)\right]a_k + iE_0 a_{-k}^+ = 0;$$

$$\left[\frac{d}{dt} + \gamma_k - i(\omega_k - \omega_0/2)\right]a_{-k}^+ - iE_0^* a_k = 0; \qquad (7)$$

$$b_k = a_k e^{-i\omega_0 t/2}.$$

Here, γ_k is the phenomenological parameter describing photon damping. According to Eqs. (7), $a_k(t)$ and $a_{-k}^+(t) \sim \exp(\alpha_k^{(0)} t)$ and $\alpha_k^{(0)} = -\gamma_k + [|E_0|^2 + (\omega_k - \omega_0/2)^2]^{1/2}$. Thus, the occupation numbers of acoustic phonons generated by density oscillations increase exponentially for $\omega_k = \omega_0/2$ and $|E_0| > \gamma_k$. Resonance occurs for wave vectors determined by the relation $|k_0| = \omega_0/2c_s$. Terms that are disregarded in Eq. (5) and relate acoustic phonons to external perturbation are responsible for renormalizations near the resonance that are immaterial for the case under consideration.

3. We assume that the stable state of phonons for $|E_0| > \gamma_k$ is formed due to interactions between them. Let us consider mechanisms generating interactions (anharmonisms) in 1D systems.

We include density fluctuations into the kinetic energy of Hamiltonian (1) [in addition to phase fluctuations appearing in Eq. (3)]. To this end, we write the boson operator of particles in the form $\Psi^+(x) = \sqrt{n + \partial_x\phi(x)}\exp(-i\theta(x)) \approx [\sqrt{n} + (\partial_x\phi)/2\sqrt{n}]\exp(-i\theta(x))$. The second preexponential term provides kinetic-energy terms including $\int dx(\partial_x\phi)^2(\partial_x\theta)^2$, $\int dx(\partial_x\phi)(\partial_x\theta)^2$, etc., corresponding to the interactions between phonons. Using Eq. (4), we show that the terms $\int dx\,(\partial_x\phi)^2(\partial_x\theta)^2$ include, along with the trivial density–density interaction, the following interaction depending on the sum phase of two phonons with opposite momenta:

$$H_{\text{int}}^{(2)} = \sum_{kk'} \mathcal{T}_{kk'} b_k^+ b_{k'}^+ b_k b_{k'} + \sum_{kk'} V_{kk'} b_{k'}^+ b_{-k'}^+ b_k b_{-k}. \qquad (8)$$

The terms $\int dx\,(\partial_x\phi)(\partial_x\theta)^2$ contain combinations of three boson operators. Such terms will be analyzed below. Other terms are immaterial in this problem.

The inclusion of the nonzero-range interaction $U(x - x')$ in Eq. (1) is the second source of interactions between phonons. In the Gross–Pitaevskiĭ theory, the energy density of the self-consistent field in the form $U|\Psi|^4 \sim n^2 \sim (\partial_x\phi)^2$ corresponds to the assumption that the interaction range is much smaller than the average distance between particles. In this case, the interaction is described by the zero-range potential. The theory based on the zero-range potential can be inapplicable for low-dimensional systems [7]. Indeed, under the assumption that the interaction range is about the average distance between particles, $R \sim n^{-1/d}$, where d is the dimension of space, and writing the interaction in the form $U(R) \sim U/R^d$, we obtain the extra multiplier of density in the energy of the self-consistent field, i.e., $U|\Psi|^4 n \sim n^3 \sim (\partial_x\phi)^3$. A similar term appears in the kinetic energy. The terms $\sim n^3 = |\Psi|^6$ physically correspond to triple collisions between particles. The role of these collisions must increase with decreasing dimension. Since terms with $n^3 \sim (\partial_x\phi)^3$ contain various combinations of three boson operators, the basic anharmonisms can be written as $H_{\text{int}} = H_{\text{int}}^{(2)} + H_{\text{int}}^{(3)}$, where $H_{\text{int}}^{(2)}$ are two-particle interactions defined in Eq. (8) and $H_{\text{int}}^{(3)}$ are all the terms containing combinations of the three boson operators. If the parameters of the system are such that the energy and momentum conservation laws cannot be satisfied for the three-particle processes, the terms $H_{\text{int}}^{(3)}$ may be excluded from the Hamiltonian by a canonical transformation. In the second order of the perturbation theory, they contribute to the matrix elements of the two-particle interactions $H_{\text{int}}^{(2)}$. In this case, $\gamma \sim \mathbb{O}(\mathcal{T}^2, V^2)$ [see Eqs. (10), (12)]. If some three-particle processes are allowed by conservation laws, damping is determined by these processes. For zero temperature, the probability of decaying excitations with momentum k and energy ω_k is calculated by means of Fermi's golden rule as $\gamma \sim |V_3|^2(k^4/m^2c_s)$ [8]. Near resonance, we set $k \approx |k_0|$. In both cases, linear damping independent of the occupation numbers of phonon pairs will be considered below. This is obviously applicable slightly above the threshold amplitude of E_0.

4. To determine the spectrum of phonons for $T = 0$ with the inclusion of interaction, we calculate the normal $G(k, \omega) = -i\langle a_k a_k^+\rangle_\omega$ and anomalous $F(k, \omega) = -i\langle a_k a_{-k}\rangle_\omega$ Green's functions for the phonons. For the system with the Hamiltonian $H = H_B + H_p + H_{\text{int}}^{(2)}$, the equations of motion for $G(k, \omega)$ and $F(k, \omega)$ have the form

$$(\omega - \omega_k - \Sigma)G(k, \omega) - \Delta_0 F^+(k, \omega) = 1;$$

$$(-\omega - \omega_k + \omega_0 - \Sigma^+)F(k, \omega) - \Delta_0^+ G(k, \omega) = 0;$$

$$\Sigma = 2i\mathcal{T}\int\frac{dk'd\omega'}{(2\pi)^2}G(k', \omega') + \mathbb{O}(\mathcal{T}^2, V^2); \qquad (9)$$

$$\Delta_0 = E_0 + iV\int\frac{dk'd\omega'}{(2\pi)^2}F(k', \omega') + \mathbb{O}(\mathcal{T}^2, V^2);$$

where $\mathbb{O}(\mathcal{T}^2, V^2)$ are terms quadratic in interaction. For simplicity, the matrix elements of the interaction are replaced by their values for $k = k' = |k_0|$ so that $V_{kk'} \approx$

$V_{|k_0|} \equiv V$, $T_{kk'} \approx T_{|k_0|} \equiv \mathcal{T}$. In this case, the solutions of Eqs. (9) are represented in the form

$$\begin{aligned} G(k,\omega) &= -\frac{(\omega-\omega_0/2)+\tilde{\xi}_k+i\gamma}{D(k,\omega)};\\ F(k,\omega) &= \frac{\Delta_0}{D(-k,\bar{\omega})};\\ \tilde{\xi}_k &= \tilde{\omega}_k-\omega_0/2; \quad \bar{\omega}\equiv(\omega_0-\omega);\\ D(k,\omega) &= -[(\omega-\omega_0/2)^2-\tilde{\xi}_k^2]\\ &\quad +\gamma^2-|\Delta_0|^2+2i\gamma(\omega-\omega_0/2);\\ \tilde{\omega}_k &= \omega_k+\mathrm{Re}\Sigma\equiv\omega_k+\mathcal{N}; \quad \gamma = \mathrm{Im}\Sigma. \end{aligned} \tag{10}$$

Hereinafter, it is assumed that $\tilde{\omega}_k = \tilde{\omega}_{-k}$. Since $i\int dk'\,d\omega G(k',\omega)$ is a real quantity, $\gamma \sim \mathbb{O}(\mathcal{T}^2, V^2)$. For the system with the Hamiltonian $H_{\mathrm{int}} = H_{\mathrm{int}}^{(2)} + H_{\mathrm{int}}^{(3)}$, the damping associated with the terms $H_{\mathrm{int}}^{(3)}$ is first calculated and it is then substituted as a parameter into solution (10) obtained above. The quantity Δ_0 in Eqs. (9) is the new amplitude of oscillations of the Bose-gas density whose magnitude and phase are renormalized due to the formation of correlated phonon pairs. In the general case, the following system of equations for Δ_0 and $\mathcal{N}$ in Eqs. (9):

$$\begin{aligned} \Delta_0 &= E_0 + i\frac{V\Delta_0}{(2\pi)^2}J_1(\mathcal{N},\Delta_0);\\ \mathcal{N} &= \frac{-i\mathcal{T}}{2\pi^2 c_s}\int_{-\xi_0}^{\xi_0} d\xi_k \int_{-\infty}^{+\infty}\frac{(\omega'+\tilde{\xi}_k+i\gamma)d\omega'}{D(\varepsilon_k,\omega')};\\ J_1 &= -\frac{1}{c_s}\int_{-\xi_0}^{\xi_0} d\xi_k \int_{-\infty}^{+\infty}\frac{(\omega'^2-\varepsilon_k^2)d\omega'}{(\omega'^2-\varepsilon_k^2)^2+4\gamma^2\omega'^2}, \end{aligned} \tag{11}$$

can be solved only numerically. Here, $\varepsilon_k^2 = \tilde{\xi}_k^2 + \Delta_\gamma^2$, $\Delta_\gamma^2 = \gamma^2 - |\Delta_0|^2$, integration with respect to k is replaced by integration with respect to ξ_k by means of the relation $d|k| = d\xi_k/c_s$, $\omega' = \omega - \omega_0/2$, and $\xi_0 = \min[\omega_0, \mu]$ is the cutoff parameter in the integrals with respect to ξ_k. However, the mechanisms of the effect of the phonon pairs on the formation of the system state beyond the stability threshold are qualitatively different for different damping values of the acoustic phonons. For this reason, we will consider the two limiting cases that are likely to be of most physical interest.

The first case is characterized by sufficiently large finite damping and small interaction-induced renormalization of the phonon frequency, so that $\mathcal{N} \ll |\Delta_0| < \gamma$. In this case, the phonon states depend on time as a_k, $a_{-k}^+ \sim e^{\alpha_k t}$ with $\alpha_k = -\gamma + [|\Delta_0|^2 - (\tilde{\omega}_k - \omega_0/2)^2]^{1/2}$. The new state with phonon pairs can either be steady for $\tilde{\omega}_k - \omega_0/2 = 0$ and $|\Delta_0| \ll \gamma$ or have an anomalously low decrement for $\gamma - |\Delta_0| \ll \gamma$. In the latter case, the solution of system (11) is given by the simple expressions

$$\begin{aligned} J_1 &= \frac{\pi\xi_0}{2\gamma c_s}; \quad \Delta_0 = \frac{E_0}{1-i(V\xi_0/8\pi\gamma c_s)};\\ \mathcal{N} &= \frac{\mathcal{T}\xi_0}{2\pi c_s}, \end{aligned} \tag{12}$$

which are obtained under the assumption that $d\tilde{\xi} = d\xi$. The relation $\mathcal{N} \ll \gamma$ is valid if $(\mathcal{T}/c_s) \ll (\gamma/\xi_0)$. When the density-oscillation amplitude is slightly larger than the threshold value, i.e., $E_0 - E_{\mathrm{th}} \ll E_{\mathrm{th}} \equiv \gamma$, the quantity $\Delta_\gamma^2 = \gamma^2 - |\Delta_0|^2$ is determined by the expression

$$\Delta_\gamma^2 = E_{\mathrm{th}}^2\left[\left(\frac{V\xi_0}{8\pi c_s E_{\mathrm{th}}}\right)^2 - \frac{E_0-E_{\mathrm{th}}}{E_{\mathrm{th}}}\right]. \tag{13}$$

We emphasize that the solution with $\Delta_\gamma^2 > 0$ above the threshold amplitude value exists only for sufficiently strong interaction V.

The second case is characterized by the large renormalization of the frequency due to the interaction independent of phonon phases and low damping, so that $\mathcal{N} > |\Delta_0| \gg \gamma$. In this case, $\alpha_k = -i[(\omega_k - \omega_0/2)^2 + 2\mathcal{N}(\omega_k - \omega_0/2) + (\mathcal{N}^2 - |\Delta_0|^2)]^{1/2} - 0^+$ and the steady state of phonons with the gap in the spectrum $\Delta^2 = \mathcal{N}^2 - |\Delta_0|^2$ exists for momenta determined by the equalities $\omega_k - \omega_0/2 = 0$ and $\omega_k - \omega_0/2 = -2\mathcal{N}$. To obtain the solutions for Δ_0 and $\mathcal{N}$ in this case, $\tilde{\xi}_k = \xi_k + \mathcal{N}$ is substituted into Eqs. (11) and the integration with respect to ξ_k is performed. When the gap is narrow, i.e., for $\mathcal{N} - |\Delta_0| \ll \mathcal{N}$, we arrive at the expression

$$\Delta^2 = \mathcal{N}^2 - \frac{E_0^2}{[1+(V/4\pi c_s)\ln(1-4\pi\mathcal{T}/c_s)^{-1}]^2}. \tag{14}$$

According to this expression, the threshold value for the amplitude E_0 is determined in this case by renormalization that is caused in the frequency of acoustic modes by density–density interaction, $E_{\mathrm{th}} \equiv \mathcal{N}$. In particular, when the amplitude is slightly above the threshold value, i.e., for $(E_0 - E_{\mathrm{th}})/E_{\mathrm{th}} \ll 1$, the gap in the phonon spectrum is equal to

$$\Delta^2 = E_{\mathrm{th}}^2\left[\left(\frac{V}{2\pi c_s}\right)\ln(1-4\pi\mathcal{T}/c_s)^{-1} - \frac{E_0-E_{\mathrm{th}}}{E_{\mathrm{th}}}\right]. \tag{15}$$

We emphasize that the gap above the threshold value of the density oscillation amplitude can exist only for non-

zero interaction depending on the total phase of the phonons.

We also note that the solution with $\Delta_0 \neq 0$ is absolutely unstable for $\gamma \ll \mathcal{N} \ll \Delta_0$. In other words, the above mechanism does not lead to the formation of a stable state in the corresponding region of parameters.

We now present relations determining the applicability limits of the above theory for the Bose gas. First, the allowable upper limit is determined for the density oscillation frequency ω_0. The wave vector k_0 introduced above is expressed in terms of the parameters of the Bose gas as $|k_0| \sim \omega_0/c_s = (\omega_0/v_J)K$. The long-wavelength approximation, which is described by Hamiltonian (3), is valid when $|k_0|/n \ll 1$. Hence, the density oscillation frequency has an upper bound determined by the inequality $\omega_0/v_J n \ll K^{-1}$. For a weakly nonideal Bose gas $K \gg 1$, whereas $K \longrightarrow 1$ values correspond to strong interaction in the Bose gas [5]. Since $v_J n \sim \mu < \omega_\perp$, the density oscillation frequency ω_0 can vary from 10^3 s^{-1} to 10 s^{-1} for, e.g., $\omega_\perp \sim 10^4$ s^{-1} and $K \sim 1$–100. In turn, the ratio V/c_s determining the existence of solutions above the threshold is estimated as $V/c_s \sim V/v_J K$. The inequality $V/v_J \ll 1$, where the left-hand side characterizes deviation from the harmonic approximation, is the applicability condition for the theory. For the weakly interacting Bose gas, the ratio V/c_s can be both much lower and much larger than unity depending on whether K is large or small (or whether the interatomic interaction is weak or strong). Since the conditions obtained for ω_0 and V/c_s are compatible, the states predicted in this work for the Bose gas can apparently be realized for gases with intermediate values $K \sim 10$, when ω_0 is not too low and the ratio V/c_s can still vary over a quite wide range. According to the available experimental parameters of the quasi-1D atomic Bose gases, the suitable values $K \sim 30$ are characteristic of the Bose gas consisting of 10^4 Na atoms with $U_{\text{eff}}/n_0 = 10^{-2}$, $U_{\text{eff}} \sim a/l_\perp^2$, and $K = \sqrt{n_0/mU_{\text{eff}}}$, where $l_\perp$ is the transverse trap size.

The single-component Fermi gas with repulsive interaction in a 1D trap is also described by Hamiltonian (6). In this case, $0 \leq K \leq 1$ [5], and, for quite small K values, the frequency ω_0 can vary in much wider ranges than for the Bose gas. In this case, $V/c_s \ll 1$. Thus, the above states can be realized for spinless fermions with almost any values of $K \leq 1$.

The above analysis implies that the original spectrum of phonons in Eq. (6) is continuous. This condition imposes certain restrictions on the longitudinal size of the real quasi-1D trap. The spacing between the longitudinal-quantization levels $\Delta\omega \sim c_s/\mathcal{L}$ must be much smaller than the above gap in the phonon spectrum Δ_γ, Δ. Thus, the above mechanism of condensation of phonon pairs can be observed in quasi-1D traps whose longitudinal size satisfies the conditions $\mathcal{L} \gg c_s/(\Delta_\gamma, \Delta)$.

I am grateful to Yu.M. Kagan for discussions and critical remarks. This work was supported by the Russian Foundation for Basic Research.

REFERENCES

1. M. Greiner, I. Bloch, O. Mandel, *et al.*, Phys. Rev. Lett. **87**, 160405 (2001).
2. M. A. Cazalilla, cond-mat/0307033.
3. F. Chevy, V. Bretin, P. Rosenbusch, *et al.*, Phys. Rev. Lett. **88**, 250402 (2002).
4. Yu. Kagan and L. A. Maksimov, Phys. Rev. A **64**, 053610 (2001).
5. F. D. M. Haldane, Phys. Rev. Lett. **47**, 1840 (1981).
6. J. L. Roberts, N. R. Claussen, S. L. Cornish, *et al.*, Phys. Rev. Lett. **86**, 4211 (2001).
7. T. D. Lee and C. N. Yang, Phys. Rev. **105**, 1119 (1957).
8. A. Recati, P. O. Fedichev, W. Zweger, and P. Zoller, cond-mat/0212195.

Translated by R. Tyapaev

JETP Letters, Vol. 80, No. 8, 2004, pp. 557–562. Translated from Pis'ma v Zhurnal Éksperimental'noĭ i Teoreticheskoĭ Fiziki, Vol. 80, No. 8, 2004, pp. 633–638.

Singularity in the LEIS Spectrum of Metal Nanoclusters

V. D. Borman[1], V. V. Lebid'ko[1], M. A. Pushkin[1], I. Smurov[2], V. N. Tronin[1], and V. I. Troyan[1,*]

[1] *Moscow Engineering Physics Institute (State University), Kashirskoe sh. 31, Moscow, 115409 Russia*

* *e-mail: VITroyan@mail.ru*

[2] *Ecole Nationale d'Ingénieurs de Saint-Etienne, 42023 Saint-Etienne, France*

Received September 28, 2004

The asymmetry of lines has been observed in the spectra of the inelastic scattering of low-energy ions interacting with nanoclusters of *d* metals. It is attributed to the mechanism of exciting *e–h* pairs with low energies and high momenta (infrared catastrophe). Analysis of the asymmetry of x-ray photoelectron spectra and spectra of low-energy scattered ions shows that the Anderson singularity indices α associated with the electron states on the surface and in bulk have different behaviors as functions of the nanocluster size. The results cannot be explained in the framework of the available concepts of the redistribution of these contributions with decreasing of the nanocluster size. © *2004 MAIK "Nauka/Interperiodica".*

PACS numbers: 73.22.–f

The current investigations of the electron properties of metal nanoclusters are urgent for both fundamental science and numerous applications. In [1, 2], x-ray photoelectron spectroscopy (XPS) showed that a decrease in the nanocluster size leads to a decrease in the density of the electron states $\rho(\varepsilon_F)$. Therefore, the valence-electron screening of a core hole also decreases, which can change the characteristics of nanoclusters up to their transition to a nonmetallic state [3, 4]. In this case, when a unit positive charge (core hole) suddenly appears, the response of the electron subsystem changes, which results in the excitation of electron–hole (*e–h*) pairs. This mechanism leads to the asymmetry of the spectral lines of photoelectrons. The mechanism of the creation of *e–h* pairs was proposed by Anderson [5] and Mahan [6]. They showed that the sudden photoionization-induced appearance of a long-lived hole (localized disturbance) on the core level leads to the creation of *e–h* pairs with very low energy and high momentum in the electron gas near the Fermi level. Since the core hole has infinite effective mass and, hence, can absorb arbitrarily high momentum, a large number of such pairs are excited (infrared catastrophe) [5, 7]. In this case, the photoelectron spectrum is singular [5, 6]:

$$I(\varepsilon) = \frac{1}{(\varepsilon - \varepsilon_0)^{1-\alpha}}\theta(\varepsilon - \varepsilon_0), \qquad (1)$$

where ε_0 is the electron binding energy on the core level, α is the Anderson singularity index, and $\theta(\varepsilon)$ is the Heaviside step function.

The singularity index is determined by the symmetry of the electron–hole scattering phases δ_l and depends quadratically on the screened potential of the local hole and the density $\rho(\varepsilon_F)$ of the electron states on the Fermi level [7, 8]. This behavior makes it possible to analyze the band structure and density of the electron states on the Fermi level of metals. Singularity indices measured for simple metals can be found in [9]. Similar phenomena were also observed in the absorption and emission of x rays in metals [10, 11]. The Coulomb potential of a light helium ion ($m/M \gg 1$, where m and M are the masses of the scatterer atom and ion, respectively) can be used as the exciting potential for *e–h* pairs. Varying the kinetic energy of ions, one can observe the excitations of collective modes in a wide range of energies and momenta from plasmons to quasiparticles (*e–h* pairs) and separate the energy range where only *e–h* pairs are excited. This procedure is fundamentally impossible for XPS. We note that the spectrum of scattered ions inelastically interacting with conduction electrons is measured in this case. At the same time, the spectrum of photoelectrons whose emission is responsible for the appearance of the local core hole is measured in XPS.

In this paper, we report experimental results on the scattering of low-energy He^+ ions by nanoclusters of a number of *d* metals (Au, Co, Mo) whose spectra exhibit the asymmetry of lines. Since low-energy-ion spectroscopy (LEIS) is sensitive only to the surface (~1 monolayer), such investigations of the asymmetry of the spectra of scattered He^+ ions provide information on the Anderson singularity index and, therefore, on the spectrum of excited *e–h* pairs in surface electron states,

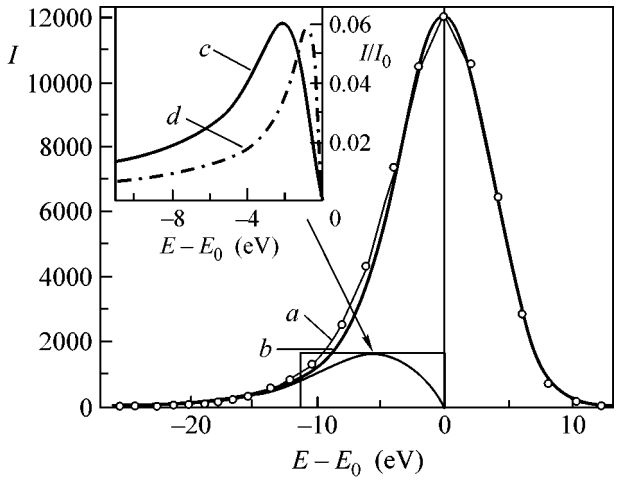

Fig. 1. (*a*) Experimental spectrum of low-energy scattered ions, (*b*) approximation of the spectrum by the convolution of function (9) with the Gaussian distribution, and excitation spectrum for *e–h* pairs according to (*c*) LEIS and (*d*) XPS.

which, as is known, differ from bulk states [12]. Nanoclusters of Au, Co, and Mo were studied also by XPS, where the asymmetry of the spectra is determined by the electron states over the mean free path of a photoelectron (several monolayers). Owing to this investigation, the contributions of the surface and bulk electron states near the Fermi surface are separated as functions of the nanocluster size. It has been found that the singularity index determined by the surface states in nanoclusters over the entire size range (20–60 Å) does not change within the error. At the same time, α determined by bulk electron states increases by a factor of almost 3 with decreasing of the nanocluster size.

Nanoclusters were formed by the pulsed laser deposition of metal (Au, Co, Mo) on the surface of highly oriented pyrolytic graphite (HOPG) at room temperature in ultrahigh vacuum ($p_{res} \approx 5 \times 10^{-10}$ Torr) in the preparation chamber of an XSAM-800 "Kratos" electron spectrometer. *In situ* control of the surface was carried out by XPS and Auger spectroscopy. The radiation of a YAG:Nd^{3+} laser ($\lambda = 1.06$ μm, *Q*-switched mode, pulse duration $\tau = 15$ ns, repetition frequency 25 Hz, energy per pulse 80 mJ) was focused on a target placed inside the preparation chamber. The surface density of the metal atoms deposited per pulse varied in the range 10^{13}–10^{15} atom/cm^2 for the deposition pulse duration $\tau_p \approx 10^{-6}$ s. The total amount of the deposited substance as a function of the number of deposition pulses for a given geometry and laser-radiation energy was determined by the *in situ* XPS method and *ex situ* Rutherford-backscattering method. The size distribution of the nanoclusters, as well as the mean nanocluster size as a function of the deposited-substance amount (and the number of deposition pulses), was determined by analyzing images obtained by vacuum–scanning–tunneling microscopy with resolution reaching the atomic value. Thus obtained dependences enabled us to analyze the singularity in the XPS and LEIS spectra of nanoclusters as a function of their mean size.

The creation of *e–h* pairs in metal nanoclusters on the HOPG surface can be indicated by the asymmetry of the spectra of He^+ ions elastically scattered on the surface of the samples under investigation on the side of lower kinetic energies. The LEIS method includes measurement of the spectrum of the ions elastically scattered by the atoms of the surface under investigation. The energy of the scattered ions is equal to $E = kE_0$, where $k = k(\theta, m/M)$ is the kinematic factor depending on the scattering angle θ, which is equal to 125° in the geometry of the XSAM-800 electron spectrometer. In particular, $k = 0.938$ for Au.

Line *a* in Fig. 1 is the typical spectrum $I(E)$ of 0.5-keV He^+ ions elastically scattered by the atoms of gold nanoclusters with the size $d \approx 60$ Å, which are formed on the HOPG surface after 5000 deposition pulses. A low-energy tail (asymmetry) appears in the entire ion-energy range under investigation. This tail arises due to inelastic losses in the kinetic energies of He^+ ions interacting with the surface atoms of Au nanoclusters. Similar dependences were obtained for other kinetic energies of He^+ ions from 0.3 to 1.5 keV. The asymmetry of the Au$4f_{5/2}$ XPS line was measured for the same nanoclusters ($d \approx 60$ Å).

As was mentioned in [8], the asymmetry observed in XPS is caused by *e–h* pair excitation. The asymmetry of the LEIS line can also be attributed to the creation of *e–h* pairs due to the sudden action of the Coulomb potential of the ion on the electron subsystem. The Massey parameter [13] $\xi = Ua/\hbar v$, where $a \cong 1.7 \times 10^{-8}$ cm is the characteristic approach distance between He^+ ions and Au atoms [14], $U \sim 1$ eV is the potential of the He^+ ion at the distance *a*, and $v \approx 2.2 \times 10^7$ cm/s is the velocity of He^+ ions for $E = 1$ keV, is estimated as $\xi = 0.77 < 1$ for the energies under investigation, which shows that the potential arises suddenly. In turn, this is the condition of the excitation of the *e–h* pairs in the ion field. Estimations for the above experimental conditions show that the following relation between the characteristic times is valid:

$$\tau_{int} < \tau_{rel} < \tau_1. \quad (2)$$

Here, $\tau_{int} = a/v \approx 7 \times 10^{-16}$ s is the time of the appearance of the potential near the surface, $\tau_{rel} \approx 10^{-15}$ s is the time of the screening of the positive charge (relaxation of valence electrons) [6], and $\tau_1 \approx 10^{-14}$ s is the charge lifetime determined by the Auger-neutralization processes in the experiments [14]. According to inequalities (2), neutralization is the slowest process. In this case, the He^+ ion loses energy due primarily to the creation of *e–h* pairs.

In view of the conservation of the energy E and momentum $\mathbf{p}$ of the He^+ ion interacting with the metal nanoclusters, the energy $\hbar\omega$ and momentum $\mathbf{q}$ associated with the creation of an e–h pair in the electron gas are related as

$$\hbar\omega = \mathbf{qp}/M. \quad (3)$$

The response of the conduction electrons of the nanocluster to external perturbation that induces the electron transition from the state with the momentum $\hbar k \le \hbar k_F$ to an unoccupied state with the momentum $\hbar k \ge \hbar k_F$ leads to the creation of an e–h pair with low energy ($\hbar\omega < \varepsilon_F$) and high momentum ($q < 2k_F$). In this case, the excitation spectrum of the e–h pairs is represented in the form [10]

$$\hbar\omega = \frac{\hbar^2}{2m}(q^2 \pm 2\mathbf{qk}_F). \quad (4)$$

Figure 2 shows dispersion relation (4) $\hbar\omega/2\varepsilon_F = f(q/k_F)$. It is seen that excitation energies are not all allowed in the spectrum of e–h excitations in the homogeneous electron gas. The allowed values lie between the lines $\frac{1}{2}q^2 \pm \mathbf{qk}_F$. In view of Eq. (3), the excitation energy $\hbar\omega/2\varepsilon_F$ is related to the momentum q/k_F of the e–h pairs as

$$\frac{\hbar\omega}{2\varepsilon_F} = \left(\frac{v}{v_F}\cos\beta\right)\frac{1}{k_F}. \quad (5)$$

Here, β is the angle between the ion momentum and the momentum excited in the electron gas and v and v_F are the velocities of the ion and electron on the Fermi surface, respectively. It is seen that electrons with low energies ($\hbar\omega \cong 1.6$ eV for $q/k_F \approx 1.5$, $\varepsilon_F = 5.5$ eV [15]) are excited in the continuous spectrum corresponding to the creation of e–h pairs in Au nanoclusters for the He^+-ion energies under investigation ($E = 300$ eV). We emphasize that the spectrum $\hbar\omega/2\varepsilon_F = f(q/k_F)$ for low momenta and high energies includes a band, where electron collective modes (plasmons) can be excited. However, according to Fig. 2 and the above estimates, the excitation of plasmons is not very probable for the low ion energies ($E < 1.5$ keV) under consideration. Their excitation is possible for ion energies of $E \ge 50$ keV.

Thus, the measured asymmetric dependence $I(E)$ (Fig. 1, line *a*) for the He^+ ions scattered on the nanocluster surface can be explained only by the excitation of a large number of e–h pairs near the Fermi surface, which is singular when the perturbing potential appears suddenly.

The asymmetry of the spectrum is quantitatively characterized by the Anderson singularity index α, which is determined by the nature of the electron–hole interaction and represented as [6]

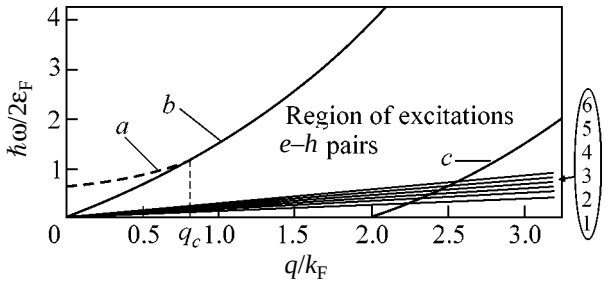

Fig. 2. Dispersion relation (4): (*a*) the plasmon excitation region and the (*b*) left and (*c*) right boundaries of the allowed excitation energies of the e–h pairs. These boundaries are determined by the formulas $\frac{1}{2}q^2 - \mathbf{qk}_F$ and $\frac{1}{2}q^2 + \mathbf{qk}_F$, respectively. The straight lines correspond to formula (5) for the following kinetic energies of the He^+ ions: (*1*) 0.3, (*2*) 0.5, (*3*) 0.7, (*4*) 1.0, (*5*) 1.3, and (*6*) 1.5 keV.

$$\alpha = \sum_l 2(2l+1)\left(\frac{\delta_l}{\pi}\right)^2. \quad (6)$$

Here, δ_l are the phase shifts corresponding to the scattering of ions by the Coulomb potential. According to Eq. (6), $\alpha > 0$ and it is limited by the value $\alpha = 0.5$ given by the Friedel sum rule [16]

$$Z = \sum_l 2(2l+1)\left(\frac{\delta_l}{\pi}\right). \quad (7)$$

Here, Z is the valence of an impurity atom [for the case under consideration, $Z = 1$ is the charge of the He^+ ion (for LEIS) or local core hole (for XPS)]. Hence, line shape (1) diverges for $\varepsilon \longrightarrow \varepsilon_0$ and has a tail for $\varepsilon \longrightarrow \infty$ with the exponent determined by α. The singularity index is determined by the density $\rho(\varepsilon_F)$ of the electron states on the Fermi level and the exciting potential U [7, 8]:

$$\alpha \propto U^2\rho^2(\varepsilon_F). \quad (8)$$

Thus, according to Eqs. (6) and (8), measurement of the singularity index in metal nanoclusters can enable one to analyze the band structure (scattering phases) and electron-state density as functions of the nanocluster size. Studies of the Anderson singularity index for the excitation of e–h pairs by the suddenly switched-on Coulomb potential provide measurement of the asymmetry of the scattering spectrum $I(E)$ of the He^+ ions (E is the kinetic energy of an ion). In this case, which is similar to XPS, singularity is determined by the excitation of e–h pairs. Thus, taking into account the energy conservation law relating the excitation energy $\hbar\omega$ of the conduction electrons to the ion kinetic energy E, we see that the spectrum of scattered ions for the case of

Table

Metal	$\rho(\varepsilon_F)$, eV^{-1}	Electron configuration in atom	XPS				LEIS			
			α	δ_l			α	δ_l		
				δ_0	δ_1	δ_2		δ_0	δ_1	δ_2
Au	0.25 [17]	$5d^{10}6s^1$ [15]	0.05* 0.05 ± 0.01	0.21	0.03	0.24	0.06 ± 0.01	0.25	0.04	0.18
Co	2.07 [18]	$3d^74s^2$	0.30 ± 0.03	1.2	0.03	0.07	0.31 ± 0.05	1.25	0.08	0.6
Mo	0.6 [19]	$4d^55s^1$	0.06 ± 0.01	0.26	0.04	0.03	0.09 ± 0.01	0.4	0.05	0.06

* The singularity index is determined for bulk Au [20].

the Coulomb potential of the ion and infinite lifetime has the form

$$I(E) = \frac{1}{(E-E_0)^{1-\alpha}}, \quad E > E_0. \tag{9}$$

Here, E_0 is the kinetic energy of the elastically scattered ions. Since the exciting potentials exist for a finite time in both XPS and LEIS, the spectral lines are broadened in the form of Lorentz broadening [9] for XPS and Gaussian broadening [14] for LEIS. Therefore, the shape of the line in XPS and LEIS spectra must be determined by the convolution of singular function (1) with the Lorentz distribution and function (9) with the Gaussian distribution, respectively, and depend on two parameters—singularity index α and spectrum half-width γ. The singularity index α may be determined by using the spectrum processing procedure proposed in [9].

Figure 1 shows the experimentally observed spectrum of low-energy 0.5-keV He^+ ions scattered by Au nanoclusters ($d \approx 60$ Å). The experimental spectrum is approximated by the solid line that is the convolution of singular function (9) with the Gaussian distribution with the half width $\gamma \approx 10$ eV. It is seen that this approximation satisfactorily reproduces the experimentally observed spectrum within the errors. Line *c* is the difference between the asymmetric and symmetric ($\alpha = 0$) spectra, and it can be treated as the excitation spectrum of the *e–h* pairs. This spectrum has a bell shape rather than the singular shape predicted theoretically. This difference is likely attributed to both the measurement errors and errors in the mathematical processing of the measured spectra. For comparison, Fig. 1 also shows (line *d*) the spectrum of *e–h* pairs excited by the core-hole potential as was measured by XPS. The significant difference observed for the line shapes can be attributed to the deviation from the suddenness of the appearance of the Coulomb potential for LEIS.

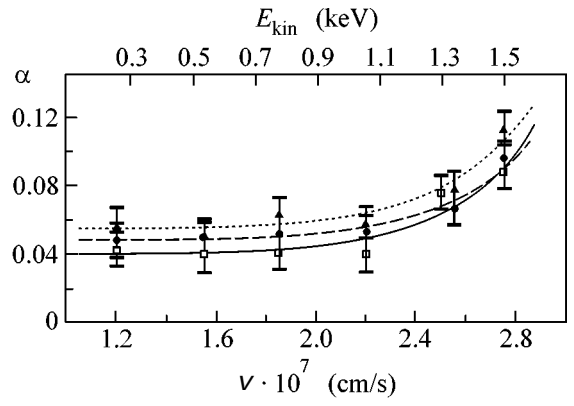

Fig. 3. Experimental singularity indices α vs. the velocity v and kinetic energy E_{kin} of ions for the laser-pulse number N = (squares) 5000 (d = 60 Å), (triangles) 400 (d = 40 Å), and (circles) 50 (d = 30 Å).

The resulting singularity indices α for nanoclusters Au, Co, and Mo ($d \approx 60$ Å) are presented in the table in comparison with the α values obtained for these metals by the XPS method. It is seen that the α values determined by XPS are systematically smaller than those obtained by LEIS. This difference can be attributed to the fact that He^+ ions for the energies under consideration interact only with surface atoms of nanoclusters, and the electron properties of the surface atoms differ from the properties of bulk atoms. This result is consistent with the observation of asymmetry (singularity index) in the excitation of surface electron states by synchrotron radiation [12]. According to the table, the α values correlate with the densities of the electron states on the Fermi level of the nanoclusters of the metals under consideration. These results are consistent with the theory presented in [7, 8] [see Eq. (8)].

Using Eqs. (6) and (7), one can determine the phases of the scattering of plane waves by the potential of the core hole or the Coulomb potential of the He^+ ion for the singularity indices of the metals under investigation (see table). Phase shifts δ_0 (*s* waves) make the largest contribution for both XPS and LEIS. In addition, the contribution from surface electron states to δ_0 is larger than the contribution from bulk states. The table also shows that the dominant contribution to the phase shift for Co ($\alpha = 0.3$) comes from *s* electrons ($\delta_0 \gg \delta_2$), whereas the dominant contribution to the phase shift for Au and Mo ($\alpha \approx 0.06$–0.09) comes from both *s* and *d*

electrons (δ_0 and δ_2). As expected, the phase δ_1 is close to zero for the *s*–*d* metals under investigation (see table).

A feature of the investigation of the spectra of He^+ ions scattered on the surface of metal nanoclusters is that the singularity index is independent, within the measurement errors, of the ion velocity in the range from 1.2×10^7 to 2.2×10^7 cm/s ($E \approx 0.3$–1 keV) (see Fig. 3) for various mean sizes of the nanoclusters. For high velocities of ions $v > 2.5 \times 10^7$ cm/s, the singularity index α increases from 0.05 to 0.09, which is likely caused by the excitation of single-particle electron states.

Figure 4 shows the singularity parameter α for LEIS spectra as a function of the mean size d of Au nanoclusters for the ion kinetic energy $E = 300$ eV. It is seen that this parameter depends only slightly (within the error) on the size d in the size range $d \approx 20$–60 Å under investigation. In addition, Fig. 4 shows singularity in the XPS spectra of Au4$f_{5/2}$ photoelectrons. For large nanoclusters ($d \approx 60$ Å), $\alpha \approx 0.05$, which corresponds to the bulk singularity index [20]. With a decrease in d, the singularity index α increases and reaches the value $\alpha \approx 0.15$ for $d \approx 20$ Å. Similar dependences were obtained for different energies of He^+ ions.

The above experimental results cannot be explained within the framework of the accepted assumption on the change in the number of nearest neighbors [21], hence, the redistribution of the contributions from the surface and bulk states with varying of the nanocluster size. Indeed, let us assume that the singularity index measured in XPS is representable in the form $\alpha = x\alpha_s + (1 - x)\alpha_b$, where the quantities α_s and α_b determined by the surface and bulk electron states, respectively, are independent of size d, and $x \sim 1/d$ and vary from 0 to 1. In this case, it is easy to show that $\alpha(d)$ is a step function such that $\alpha \longrightarrow \alpha_s \approx 0.06$ for $d \longrightarrow 0$ ($x \longrightarrow 1$) and $\alpha \longrightarrow \alpha_b \approx 0.05$ for $d \longrightarrow \infty$ ($x \longrightarrow 0$), which is inconsistent with the observed $\alpha(d)$ dependence. We note that, under this assumption, the binding energies of the core electrons in the XPS spectra of the initial and final states are satisfactorily described as functions of the nanocluster size [1, 2]. Thus, the nanocluster-size dependence of the singularity index obtained in this work can be attributed to the fact that α is determined not only by the change in $\rho(\varepsilon_F)$ but also by the redistribution of the band structure of the conduction electrons in the nanocluster with varying of its size. The above analysis of the experimental results shows that, when the mean size ($d \approx 20$ Å) of the Au nanocluster decreases, the phase shift δ_0 (*s* wave) increases by a factor of almost 3 ($\delta_0 \approx 0.75$) compared to the bulk value ($\delta_0 \approx 0.21$) and the phase shift δ_2 (*d* wave) decreases by a factor of 1.5 ($\delta_2 \approx 0.16$). Thus, the change in the singularity index with the nanocluster size is determined by the band structure of the nanocluster in contrast to the usual characteristics [1, 2] such as the energies of the initial and final states.

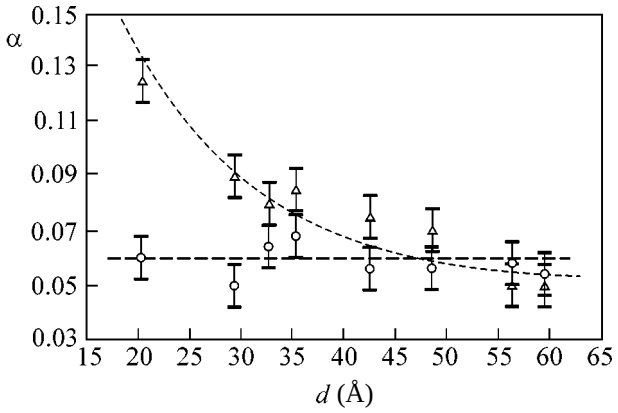

Fig. 4. Experimental singularity indices α vs. the size d of the Au nanoclusters deposited on the surface of highly oriented pyrolytic graphite according to (circles) LEIS (E_{kin} = 0.3 keV) and (triangles) XPS.

In conclusion, it should be noted that the asymmetry observed in metal nanoclusters is attributed to the excitation of the continuous spectrum of *e*–*h* pairs. In the nonmetallic state of matter, instead of the continuous spectrum of *e*–*h* pairs, discrete shake-up satellites and, hence, discrete excitations appear [19]. Therefore, the metal–nonmetal transition can be observed when the cluster size decreases.

We are grateful to A.V. Zenkevich, D.O. Filatov, D.A. Antonov, and Yu.Yu. Lebedinskiĭ for assistance in obtaining nanoclusters by pulsed laser deposition and carrying out scanning tunneling microscopy studies and experiments on LEIS. The work of V.V.L. was supported in part by the Ministry of Education of the Russian Federation (project no. A03-2.9-813). The work of M.A.P. was supported by the Basic Research and Higher Education Program, the US Civilian Research and Development Foundation for the Independent States of the Former Soviet Union and the Ministry of Education of the Russian Federation (grant no. Y1-P-01-12).

REFERENCES

1. P. H. Citrin and G. K. Wertheim, Phys. Rev. B **27**, 3176 (1983).
2. V. N. Nevolin, A. V. Zenkevich, X. Ch. Lai, *et al.*, Laser Phys. **11**, 45 (2001).
3. C. Xu, X. Lai, G. W. Zajac, and D. W. Goodman, Phys. Rev. B **56**, 13464 (1997).
4. V. D. Borman, X. Ch. Lai, M. A. Pushkin, *et al.*, JETP Lett. **76**, 444 (2002).
5. P. W. Anderson, Phys. Rev. Lett. **18**, 1049 (1967).
6. G. D. Mahan, Phys. Rev. **163**, 612 (1967).
7. J. J. Hopfield, Comments Solid State Phys. **2**, 2 (1969).
8. D. C. Langreth, Phys. Rev. B **1**, 471 (1970).

9. P. H. Citrin, G. K. Wertheim, and Y. Baer, Phys. Rev. B **16**, 4256 (1977).
10. N. H. March and M. Parrinello, *Collective Effects in Solids and Liquids* (Hilger, Bristol, 1982; Mir, Moscow, 1986).
11. P. Nozieres and C. T. de Dominicis, Phys. Rev. **178**, 1097 (1969).
12. G. K. Wertheim, D. M. Riffe, and P. H. Citrin, Phys. Rev. B **45**, 8703 (1992).
13. J. R. Taylor, *Scattering Theory: the Quantum Theory of Nonrelativistic Collisions* (Wiley, New York, 1972; Mir, Moscow, 1975).
14. *Interaction of Charged Particles with Solids and Surfaces*, Ed. by A. Gras-Marti, H. M. Urbassek, N. R. Arista, and F. Flores (Plenum, New York, 1991).
15. N. W. Ashcroft and N. D. Mermin, *Solid State Physics* (Holt, Rinehart and Winston, New York, 1976; Mir, Moscow, 1979).
16. J. M. Ziman, *Principles of the Theory of Solids*, 2nd ed. (Cambridge Univ. Press, London, 1972; Mir, Moscow, 1974).
17. N. V. Smith, G. K. Wertheim, S. Hüfner, and M. M. Traum, Phys. Rev. B **10**, 3197 (1974).
18. F. Batallan, I. Rosenman, and C. B. Sommers, Phys. Rev. B **11**, 545 (1975).
19. D. D. Koelling, F. M. Mueller, and A. J. Arko, Phys. Rev. B **10**, 4889 (1974).
20. S. Hufner and G. K. Wertheim, Phys. Rev. B **11**, 5197 (1975).
21. M. G. Mason, Phys. Rev. B **27**, 748 (1983).
22. *Practical Surface Analysis by Auger and X-ray Photoelectron Spectroscopy*, Ed. by D. Briggs and M. Seah (Wiley, New York, 1983; Mir, Moscow, 1987).

Translated by R. Tyapaev

JETP Letters, Vol. 80, No. 8, 2004, pp. 563–567. Translated from Pis'ma v Zhurnal Éksperimental'noĭ i Teoreticheskoĭ Fiziki, Vol. 80, No. 8, 2004, pp. 639–644.

On a Collective Attack on the Key in Quantum Cryptography on Two Nonorthogonal States

S. N. Molotkov

Institute of Solid State Physics, Russian Academy of Sciences, Chernogolovka, Moscow region, 142432 Russia

Faculty of Computational Mathematics and Cybernetics, Moscow State University, Vorob'evy gory, Moscow, 119899 Russia

Received September 21, 2004

A "collective" attack on the key is considered, and its connection with the classical capacity of a quantum communication channel is analyzed. It has been shown that the allowable error probability for legitimate users to which the secure key can be extracted is less than half the value for "translucent" eavesdropping and individual measurements. © *2004 MAIK "Nauka/Interperiodica".*

PACS numbers: 03.67.Dt; 42.50.–p; 89.70.+c

Quantum key distribution (quantum cryptography) ensures the security of key distribution at the level of fundamental quantum-mechanical laws of nature [1–3].

Various eavesdropping strategies can be conventionally classified as follows.

(i) The "opaque" eavesdropping strategy, which is often called reception–retransmission, is reduced to measurement of a transmitted state and further retransmission of a new state depending on the measurement result.

(ii) In individual "translucent" eavesdropping strategy, the eavesdropper ensures interaction of its auxiliary state for each message with the transmitted state for a certain time. After the interaction, the transmitted and auxiliary states are in a common entangled state. Then, the eavesdropper carries out measurement of the auxiliary state for each message and the informative state is transmitted to the legitimate user at the receiving end.

(iii) A "collective" attack is similar to the preceding case, but the eavesdropper accumulates his auxiliary states in quantum memory and does not carry out measurements until all the states have been transmitted by the legitimate user. Then, after exchange through an open channel has been completed in order to correct errors and enhance security, the eavesdropper carries out measurements simultaneously over all his states.

(iv) Finally, the most general and apparently most efficient attack (joint attack) is similar to the preceding one, but the eavesdropper uses a single auxiliary state from the Hilbert space of high-dimensional states that interacts with the transmitted states, and all the measurements over which are carried out at the end.

In this work, a "collective" attack on the key is considered, and its connection with the classical capacity of a quantum communication channel is analyzed. Quantum cryptography on two nonorthogonal states (B92 protocol) [2] is conceptually the simplest. The security of this protocol was analyzed in a number of works [4–9] for various measurements at the receiving end. Collective measurements were considered for this exchange protocol only for a particular case of the determination of the parity bit [10].

The standard protocol for the legitimate users is as follows. A pair of nonorthogonal single-photon states $0 \longrightarrow |u\rangle$ and $1 \longrightarrow |v\rangle$ is used as the informative states. We follow the notation from [4] for convenient comparison:

$$\langle u|v\rangle = \sin(2\alpha), \quad \langle e_0|e_1\rangle = 0, \tag{1}$$

where $|e_0\rangle$ and $|e_1\rangle$ are the orthonormalized basis vectors in space spanned by $|u\rangle$ and $|v\rangle$ (see Fig. 1). The same measurement is always carried out at the receiving end. This measurement is described by the unity decomposition

$$\mathcal{A}_u = \frac{(I - |v\rangle\langle v|)}{1 + \langle u|v\rangle}, \quad \mathcal{A}_v = \frac{(I - |u\rangle\langle u|)}{1 + \langle u|v\rangle}, \tag{2}$$
$$\mathcal{A}_? = I - \mathcal{A}_u - \mathcal{A}_v.$$

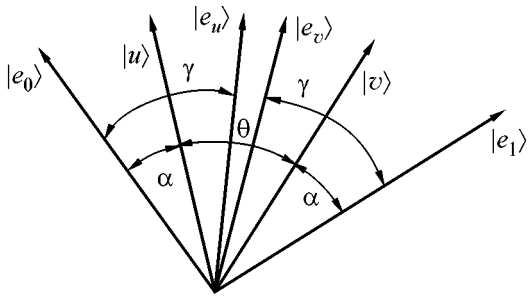

Fig. 1.

0021-3640/04/8008-0563$26.00 © 2004 MAIK "Nauka/Interperiodica"

The space of results at the receiving end consists of three results 0, 1, and ?, whose probabilities on the input states $|u\rangle$ and $|v\rangle$ are

$$\mathrm{Tr}_B\{|u\rangle\langle u|\mathcal{A}_v\} = \mathrm{Tr}_B\{|v\rangle\langle v|\mathcal{A}_u\} = 0,$$
$$\mathrm{Tr}_B\{|u\rangle\langle u|\mathcal{A}_u\} = \mathrm{Tr}_B\{|v\rangle\langle v|\mathcal{A}_v\} = 1-\cos(\theta), \quad (3)$$
$$\mathrm{Tr}_B\{|u\rangle\langle u|\mathcal{A}_?\} = \mathrm{Tr}_B\{|v\rangle\langle v|\mathcal{A}_?\} = \cos(\theta).$$

Subscript B means the trace over the space of states at the receiving end.[1] Results 0 and 1 are conclusive results; i.e., the channel $\mathcal{A}_u$ can trigger only on the state $|u\rangle$ and never on the input state $|v\rangle$ and vice versa. Counts in the channel $\mathcal{A}_?$ are inconclusive results, because they may occur on both states $|u\rangle$ and $|v\rangle$.

Further actions of the legitimate users are as follows. Alice transmits states $|u\rangle$ and $|v\rangle$ with equal probability to Bob, who carries out measurement (2). After the transmission of a sufficiently long sequence, Bob, using an open classical channel, reports in which messages he has obtained inconclusive measurement results. These messages are omitted. Further, approximately half the randomly chosen bits are reported, and the error probability Q is estimated. These open bits are then rejected. The error probability in the unopened part of the long sequence coincides with Q. If $Q < Q_c$, the legitimate users correct the errors and extract the secure key.

The actions of Eve are as follows. Eve prepares her auxiliary state $|e\rangle$ for each message. This auxiliary state interacts with the transmitted state. The joint evolution is described as (see Fig. 1 and [4])

$$|u\rangle\otimes|e\rangle \longrightarrow U(|u\rangle\otimes|e\rangle)$$
$$= a|u\rangle\otimes|e_u\rangle + b|v\rangle\otimes|e_v\rangle = |\phi_1\rangle, \quad (4)$$

$$|v\rangle\otimes|e\rangle \longrightarrow U(|v\rangle\otimes|e\rangle)$$
$$= b|u\rangle\otimes|e_u\rangle + a|v\rangle\otimes|e_v\rangle = |\phi_2\rangle. \quad (5)$$

Here, $|e_u\rangle$ and $|e_v\rangle$ are states in space spanned by $|u\rangle$ and $|v\rangle$, whereas a and b are real coefficients, which can be chosen by Eve (are determined by the operator of joint unitary evolution). Eve stores her modified states in quantum memory and does not carry out any measurements until the legitimate users do not complete the exchange of information through both the quantum and classical channels.

Bob carries out individual measurements over the states in each message. States that are seen by Bob are given by the partial trace over Eve's subspace of states. For the input states $|u\rangle$ and $|v\rangle$, we have

$$\rho(|u\rangle) = \mathrm{Tr}_E\{|\phi_1\rangle\langle\phi_1|\}$$
$$= a^2|u\rangle\langle u| + ab\sin(2\gamma)(|u\rangle\langle v| + |v\rangle\langle u|) + b^2|v\rangle\langle v|, \quad (6)$$

and

$$\rho(|v\rangle) = \mathrm{Tr}_E\{|\phi_2\rangle\langle\phi_2|\}$$
$$= b^2|u\rangle\langle u| + ab\sin(2\gamma)(|u\rangle\langle v| + |v\rangle\langle u|) + a^2|v\rangle\langle v|, \quad (7)$$

respectively. Taking Eqs. (4)–(7) into account, we arrive at the following expressions for the result probabilities at the receiving end (the right-hand symbol corresponds to the sent state, and the left-hand symbol corresponds to the interpretation of the measurement result):

$$\Pr\{0|0\} = \mathrm{Tr}_B\{\mathcal{A}_u\rho(|u\rangle)\} = a^2(1-\sin(2\alpha)), \quad (8)$$

$$\Pr\{1|0\} = \mathrm{Tr}_B\{\mathcal{A}_v\rho(|u\rangle)\} = b^2(1-\sin(2\alpha)), \quad (9)$$

$$\Pr\{?|0\} = \mathrm{Tr}_B\{\mathcal{A}_?\rho(|u\rangle)\}$$
$$= 1-(a^2+b^2)(1-\sin(2\alpha)). \quad (10)$$

For the remaining transition probabilities, we similarly obtain

$$\Pr\{1|1\} = \Pr\{0|0\}, \quad \Pr\{0|1\} = \Pr\{1|0\},$$
$$\Pr\{?|1\} = \Pr\{?|0\}. \quad (11)$$

The legitimate users reject messages where inconclusive results have been obtained. The probabilities of correctly ($\Pr\{1|1\}$, $\Pr\{0|0\}$) and erroneously ($\Pr\{0|1\}$, $\Pr\{1|0\}$) interpreted results are determined as

$$Q_{\mathrm{OK}} = \frac{a^2}{a^2+b^2} \quad (12)$$

and

$$Q = \frac{b^2}{a^2+b^2}, \quad (13)$$

respectively. Eve also rejects states from quantum memory in the positions where Bob obtains an inconclusive result.

Then, Alice and Bob open approximately half their bit sequences by random sampling and estimate the error probability Q. As a result, Eve holds states only in the positions where Bob obtains conclusive results. States in these positions that are seen by Eve after measurements made by Bob are given by the (unnormalized) density matrices

$$\rho_E^{\mathrm{OK}}(|u\rangle) = \mathrm{Tr}_B\{\sqrt{\mathcal{A}_u}|\phi_1\rangle\langle\phi_1|\sqrt{\mathcal{A}_u}\}$$
$$= (1-Q)|e_u\rangle\langle e_u|, \quad (14)$$

because the operators $\mathcal{A}_u$ and $\mathcal{A}_v$ are orthogonal projectors up to normalization. Formula (14) means that the state $|u\rangle$ is present in Eve's quantum-memory cell, and Bob's measurement yields the correct result, which corresponds to the input state $|u\rangle$ sent by Alice. Correspondingly, Eve's memory cell contains the state

$$\rho_E^{Q}(|u\rangle) = \mathrm{Tr}_B\{\sqrt{\mathcal{A}_v}|\phi_1\rangle\langle\phi_1|\sqrt{\mathcal{A}_v}\} = Q|e_v\rangle\langle e_v|, \quad (15)$$

[1] For brevity, the ordinary names Alice, Bob, and Eve are used for the transmitter, receiver, and eavesdropper, respectively.

if Bob obtains the measurement result on the state $|u\rangle$ with error. Similarly, for the input state $|v\rangle$,

$$\rho_E^{\mathrm{OK}}(|v\rangle) = \mathrm{Tr}_B\{\sqrt{\mathscr{A}_v}|\phi_2\rangle\langle\phi_2|\sqrt{\mathscr{A}_v}\} = (1-Q)|e_v\rangle\langle e_v|, \quad (16)$$

$$\rho_E^{Q}(|v\rangle) = \mathrm{Tr}_B\{\sqrt{\mathscr{A}_u}|\phi_2\rangle\langle\phi_2|\sqrt{\mathscr{A}_u}\} = Q|e_u\rangle\langle e_u|. \quad (17)$$

There is one-to-one correspondence between the correct and erroneous positions obtained by Bob and Eve. Namely, Eve has the state $\rho_E^{\mathrm{OK}}(|u\rangle)$ in a position corresponding to the position where Bob's measurement yields a conclusive result and it is correctly interpreted; e.g., Alice transmits the state $|u\rangle$ and Bob interprets it as 0. Eve has the erroneous state $1 - \rho_E^{Q}(|u\rangle)$ rather than 0 in a position corresponding to the position where Bob's measurement yields a conclusive result, but it is erroneously interpreted: Alice transmits the state $|u\rangle$ and Bob interprets it as 1. The situation is similar for the transmitted state $|v\rangle$.

Naturally, the positions of the erroneous results are unknown for Bob and Eve. At that instant, the difference between Bob and Eve is that Bob has information in retained positions in the classical form (0 and 1 bits), whereas Eve has information in the form of quantum states corresponding to Bob's classical bits. Eve will attempt to determine the secure key by quantum-mechanical measurements and decision rules that provide the classical bit sequence closest to the key sequence used by Alice and Bob. In fact, Eve has only pure states $|u\rangle$ and $|v\rangle$ in each cell of quantum memory, and they are found with a probability of 1/2.

At that instant, the legitimate users have classical bit strings, whereas Eve has a quantum-memory register with states. The further argumentation is based on random codewords. As is known [11, 12], such random codes provide the Shannon limit. Since Alice and Bob communicate through a classical binary symmetric channel with error probability Q, they can use an open channel to generate a set of M random codewords that allow them to correct errors with unit probability upon decoding. In this procedure, Alice treats the n-bit unopened part of the bit string transmitted to her as the first codeword, randomly generates $M-1$ additional codewords of length n, and openly reports all M codewords to Bob.

Let $w^1, w^2, \ldots, w^M$ be such a set of codewords. Each codeword is a binary string of length n: $w^i = \{i_1, i_2, \ldots, i_n\}$, where $i_k = 0$ or 1. The code redundancy (the number of codewords for random codewords) must be such that it ensures the unit-probability correction of errors occurring with frequency Q. This is possible if the number of codewords satisfies the inequality [11, 12]

$$M < 2^{n[H(Q)-\delta]}, \quad I_{AB}(Q) = H(Q) = 1 + Q\log(Q) + (1-Q)\log(1-Q), \quad (18)$$

where $H(Q)$ is the capacity of the binary symmetric channel. The error probability over all the codewords satisfies the inequality [12]

$$p_{AB}(n, M) \le 2\varepsilon + (M-1)2^{n[H(Q)-\delta]} \longrightarrow 0 \quad (19)$$

under condition (18).

Eve aims to refer to the classical codewords openly announced by Alice. Then, using the classical codewords, Eve constructs decision rules for quantum-mechanical measurements in order to determine the correct codeword corresponding to the key with the maximum probability. Eve compares $|\psi_{w^i}\rangle = |e_{i_1}\rangle \otimes |e_{i_2}\rangle \ldots \otimes |e_{i_n}\rangle$, where $|e_{i_k}\rangle = |e_u\rangle$ and $|e_v\rangle$ for $i_k = 0$ and 1, respectively, with each classical codeword $w^i = \{i_1, i_2, \ldots, i_n\}$ of Alice and Bob. In fact, Eve compares the nonorthogonal quantum states $|e_u\rangle$ and $|e_v\rangle$ with each of the positions 0 and 1, respectively, of each classical codeword. If the states were orthogonal, Eve could reliably distinguish them, i.e., write 0 and 1 to the corresponding positions and have the same bit string as Bob. However, the states are reliably indistinguishable due to nonorthogonality, and Eve's measurement provides extra error compared to Bob's measurement. Eve may carry out individual measurements [13] of states in each of the positions and treat the result as 0 or 1. The error is smaller if Eve carries out collective measurements [14] using the measurement operators described below.

Since the codewords are chosen randomly and independently from each other, the probability of an individual codeword is given as (for details, see [14])

$$\Pr\{w = (i_1, i_2, \ldots, i_n)\} = p_{i_1}p_{i_2}\ldots p_{i_n} = \frac{1}{2^n}, \quad p_{i_k} = \frac{1}{2}, \quad (20)$$

and the mathematical expectation $\rho_{w^i} = |\psi_{w^i}\rangle\langle\psi_{w^i}|$ has the form

$$\mathbf{E}(\rho_{w^i}) = \sum_{i_1, i_2, \ldots, i_n} p_{i_1}p_{i_2}\ldots p_{i_n}|e_{i_1}\rangle\langle e_{i_1}| \otimes \ldots \otimes |e_{i_n}\rangle\langle e_{i_n}| = \rho_E^{\otimes n}, \quad (21)$$

where

$$\rho_E = \frac{1}{2}|e_u\rangle\langle e_u| + \frac{1}{2}|e_v\rangle\langle e_v| \quad (22)$$

is the density matrix describing the quantum-memory states.

Further, Eve decodes quantum codewords (transforms them into classical bit strings) by using the decision rule specified by the measurement operators

$$\mathscr{X}_k = |\tilde{\psi}_{w^k}\rangle\langle\tilde{\psi}_{w^k}|, \quad |\tilde{\psi}_{w^k}\rangle = \mathscr{P}|\psi_{w^k}\rangle, \quad (23)$$

where

$$\mathcal{P} = \sum_{J \in B} |\lambda_J\rangle\langle\lambda_J|, \quad |\lambda_J\rangle = |\lambda_{j_1}\rangle \otimes |\lambda_{j_2}\rangle \ldots \otimes |\lambda_{j_n}\rangle, \quad (24)$$

$\mathcal{P}$ is the projector on the typical subspace of the density matrix $\rho_E^{\otimes n}$. Here, $|\lambda_{j_k}\rangle$ are the eigenvectors of ρ_E and $\lambda_J = \lambda_{j_1}\lambda_{j_2}\ldots\lambda_{j_n}$ are its eigenvalues. The typical subspace of the density matrix is defined as

$$B = \{J : 2^{-n[H(\rho_E)+\delta]} < \lambda_J < 2^{-n[H(\rho_E)-\delta]}\}, \quad (25)$$

and satisfies the conditions (see [14])

$$\left\|\rho_E^{\otimes n}\mathcal{P}\right\| < 2^{-n[H(\rho_E)-\delta]}, \quad \mathrm{Tr}\{\rho_E^{\otimes n}(1-\mathcal{P})\} < \varepsilon. \quad (26)$$

The quantity $H(\rho_E)$ is the von Neumann entropy and, in the case under consideration, coincides with the classical capacity of the binary quantum communication channel [14]:

$$\begin{aligned}\bar{C}(\rho_E) &= H(\rho_E) = -\mathrm{Tr}\{\rho_E \log \rho_E\} \\ &= -\lambda_1 \log \lambda_1 - \lambda_2 \log \lambda_2 \\ &= -\left(\frac{1-\sin(2\gamma)}{2}\right)\log\left(\frac{1-\sin(2\gamma)}{2}\right) \\ &\quad -\left(\frac{1+\sin(2\gamma)}{2}\right)\log\left(\frac{1+\sin(2\gamma)}{2}\right),\end{aligned} \quad (27)$$

where $\lambda_{1,2} = (1 \pm \sin(2\gamma))/2$ are the eigenvalues of ρ_E.

Eve decodes M codewords, which are generated by Alice, with the error [14]

$$\begin{aligned}p_E(n, M) &\le 2\mathrm{Tr}\{\rho^{\otimes n}(1-\mathcal{P})\} \\ &+ (M-1)\mathrm{Tr}\{(\rho^{\otimes n}\mathcal{P})^2\} \le 2\varepsilon + (M-1)2^{-[H(\rho_E)-\delta]},\end{aligned} \quad (28)$$

whereas the legitimate users decode with the error [12]

$$p_{AB}(n, M) \le 2\varepsilon + (M-1)2^{n[H(Q)-\delta]}. \quad (29)$$

Thus, if

$$H(Q) > H(\rho_E) = \bar{C}(\rho_E) \quad (30)$$

and the legitimate users choose $M < 2^{n[H(Q)-\delta]}$ codewords, then their decoding error tends to zero, whereas Eve's error is nonzero (tends to unity). In other words, under condition (18), Alice and Bob have the same (with unit probability) bit string (secure key) after decoding, whereas Eve with unit probability does not know this string.

The quantity $\bar{C}(\rho_E)$ is the classical capacity of the binary quantum communication channel [13, 14]. If Eve carried out optimum individual measurements with the minimum error of distinguishing a pair of nonorthogonal states, then $\bar{C}(\rho_E)$ would change to the classical capacity of the binary quantum communication channel per one shot [14], which is given as

$$\begin{aligned}C_1(\rho_E) &= \frac{1}{2}[(1+\sqrt{1-\sin^2(2\gamma)})] \\ &\times \log(1+\sqrt{1-\sin^2(2\gamma)}) \\ &+ (1-\sqrt{1-\sin^2(2\gamma)})]\log(1-\sqrt{1-\sin^2(2\gamma)})]\end{aligned} \quad (31)$$

and never exceeds expression (27); i.e., $C_1(\rho_E) < \bar{C}(\rho_E)$.

Secure key distribution is possible if, for a given error Q of the legitimate users, the capacity of the classical binary symmetric channel between Alice and Bob exceeds the classical capacity of the binary quantum channel for Eve. To obtain the final result, it is necessary to express $\bar{C}(\rho_E)$ [in fact, $\sin(2\gamma)$] in terms of the parameters a, b, Q, and $\sin(2\alpha)$, where α is the angle between the signal states chosen by the legitimate users. Let us derive these relations. The unitarity and normalization conditions for the states $|\phi_{1,2}\rangle$ in Eqs. (4) and (5) lead to the conditions

$$\begin{aligned}\sin(2\alpha) &= 2ab + (a^2+b^2)\sin(2\alpha)\sin(2\gamma), \\ a^2 + b^2 + 2ab\sin(2\alpha)\sin(2\gamma) &= 1.\end{aligned} \quad (32)$$

Therefore,

$$\sin(2\gamma) = \frac{\sqrt{1-(1-2Q)^2} - \sin(2\alpha)}{\sin(2\alpha)[\sqrt{1-(1-2Q)^2}\sin(2\alpha) - 1]}. \quad (33)$$

Let us discuss the results. As is known [15, 16], secure key distribution is possible if

$$C_s \ge \max I_{AB} - I_{AE}, I_{AB} - I_{BE} > 0. \quad (34)$$

Here, C_s is the secure capacity of the channel between Alice and Bob in the presence of Eve (the number of bits of the secure key per message that can be transmitted by the legitimate users in the long-sequence limit) and I_{AB}, I_{AE}, and I_{BE} are the maximum mutual information (upon Eve's attack and chosen signal states and measurements at the receiving end) between Alice and Bob, Alice and Eve, and Bob and Eve, respectively. For Eve's individual measurements (see below), $I_{AE} \le I_{BE}$. Therefore, condition (34) is reduced to the form

$$C_s \ge I_{AB} - I_{AE} > 0. \quad (35)$$

The quantities I_{AE} and I_{BE} are determined by the errors Q_{AE} and Q_{BE} in the Alice–Eve and Bob–Eve channels, respectively. Taking Eqs. (6)–(13) into account, we obtain (for details, see [4, 5])

$$Q_{AE} = Q\cos^2\gamma + (1-Q)\sin^2\gamma, \quad Q_{BE} = \sin^2\gamma, \quad (36)$$

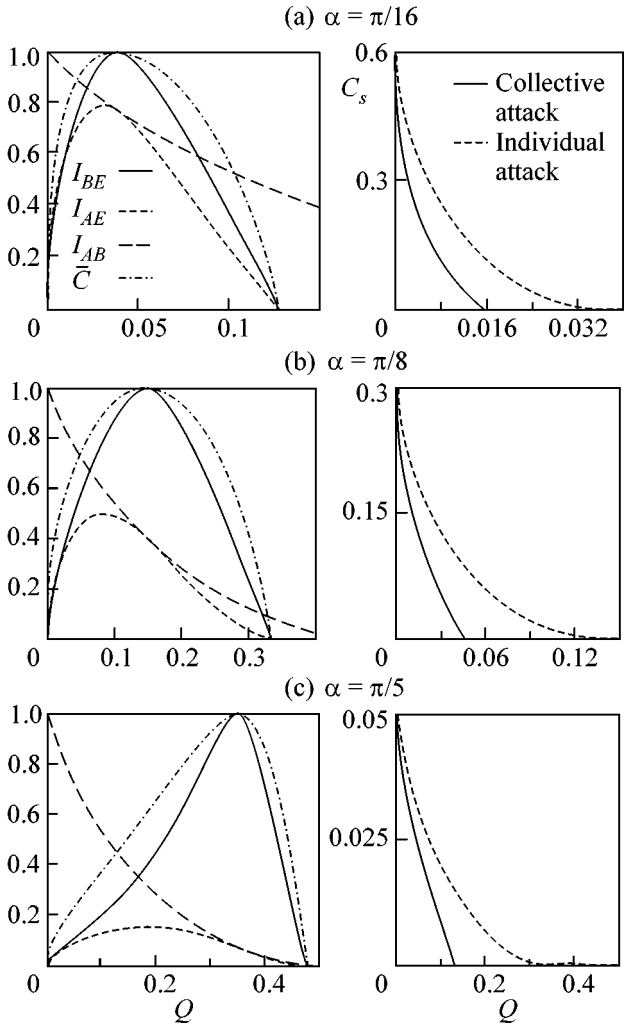

Fig. 2.

and

$$I_{AE} = 1 + Q_{AE}\log Q_{AE} + (1 - Q_{AE})\log(1 - Q_{AE}),$$
$$I_{BE} = 1 + Q_{BE}\log Q_{BE} + (1 - Q_{BE})\log(1 - Q_{BE}). \quad (37)$$

We emphasize that the mutual information between Eve and both legitimate users is the same upon the collective attack; i.e., $I_{AE} = I_{BE} = \bar{C}(\rho_E)$. In this case, condition (34) takes the form

$$C_s \geq I_{AB} - \bar{C}(\rho_E) > 0, \quad I_{AB} \geq \bar{C}(\rho_E). \quad (38)$$

Figure 2 shows (left-hand panels) I_{AB}, I_{AE}, and I_{BE} for translucent eavesdropping and $\bar{C}(\rho_E)$ for the collective attack as functions of the error Q introduced by Eve in the channel between the legitimate users for the overlapping angle α = (a) $\pi/16$, (b) $\pi/8$, and (c) $\pi/5$ between the signal states $|u\rangle$ and $|v\rangle$. It is seen that the critical error to which the secure key distribution is guaranteed in the presence of the collective attack is approximately half the critical error upon individual measurements by Eve. Therefore, the collective attack is much more efficient for Eve. The right-hand panels in Fig. 2 show the secure capacity (38) multiplied by the fraction of conclusive results. For small overlapping angles between the signal states (when the nonorthogonal states are more distinguishable), the secure capacity for, e.g., $\alpha = \pi/16$ is sufficiently large (Q is small, $C_s \sim 0.6$, approximately every second bit of the initial sequence is secure). However, the critical error is no more than 1.5%. For large overlapping angles, when the nonorthogonal states are less distinguishable, e.g., $\alpha = \pi/5$, the critical error ≈11%. However, the secure capacity is very small. Only 5% of the bits of the initial transmitted sequence are secure.

This work was supported by the Academy of Cryptography of the Russian Federation, the Russian Foundation for Basic Research (project no. 02-02-16289), and Moscow State University (interdisciplinary project).

REFERENCES

1. S. Wiesner, SIGACT News **15**, 78 (1983).
2. C. H. Bennett and G. Brassard, in *Proceedings of IEEE International Conference on Computers, Systems, and Signal Processing, Bangalore, India* (IEEE, New York, 1984), p. 175; C. H. Bennett, Phys. Rev. Lett. **68**, 3121 (1992).
3. W. K. Wootters and W. H. Zurek, Nature **299**, 802 (1982).
4. A. K. Ekert, B. Huttner, G. M. Palma, and A. Peres, Phys. Rev. A **50**, 1047 (1994).
5. H. E. Brandt, J. M. Myers, and S. J. Lomonaco, Jr., Phys. Rev. A **56**, 4456 (1997).
6. B. A. Slutsky, R. Rao, Pang-Chen Sun, and Y. Fainman, Phys. Rev. A **57**, 2383 (1998).
7. K. Tamaki, M. Koashi, and N. Imoto, quant-ph/0212161.
8. K. Tamaki, M. Koashi, and N. Imoto, quant-ph/0212162.
9. K. Tamaki and N. Lutkenhaus, quant-ph/0308048.
10. E. Biham and T. Mor, Phys. Rev. Lett. **78**, 2256 (1997); **79**, 4034 (1997).
11. C. E. Shannon, Bell Syst. Tech. J. **27**, 397 (1948); **27**, 623 (1948).
12. R. Gallagher, *Information Theory and Reliable Communication* (Wiley, New York, 1968; Sovetskoe Radio, Moscow, 1974).
13. A. S. Kholevo, *Introduction to the Quantum Theory of Information* (MTsNMO, Moscow, 2002), Sovrem. Mat. Fiz., No. 5.
14. A. S. Kholevo, Probl. Peredachi Inf. **8**, 63 (1972); **15**, 3 (1979); Usp. Mat. Nauk **53**, 193 (1998).
15. I. Csiszár and J. Körner, IEEE Trans. Inf. Theory **24**, 339 (1978).
16. D. Maurer, IEEE Trans. Inf. Theory **39**, 733 (1993).

Translated by R. Tyapaev

JETP Letters, Vol. 80, No. 8, 2004, pp. 568–571. Translated from Pis'ma v Zhurnal Éksperimental'noĭ i Teoreticheskoĭ Fiziki, Vol. 80, No. 8, 2004, pp. 645–649.

Femtosecond Laser Photoelectron Projection Microscopy of Organic Nanocomplexes

S. A. Aseev, B. N. Mironov, S. V. Chekalin, and V. S. Letokhov

Institute of Spectroscopy, Russian Academy of Sciences, Troitsk, Moscow region, 142190 Russia

Received September 29, 2004

Organic nanocomplexes obtained by applying an organic dye (Coumarin 153) solution onto the surface of a metal nanotip were studied by femtosecond laser photoelectron projection microscopy. The tip was a 100-nm-diameter capillary covered with a thin nickel layer. The image of a through hole of the capillary was a convenient reference for interpretation of the results. The spatial resolution achieved in these experiments was equal to about 5 nm. © *2004 MAIK "Nauka/Interperiodica".*

PACS numbers: 06.60.Jn; 68.37.–d; 79.60.Jv

Reaching a spatial resolution of several nanometers is among the most important tasks in nanooptics [1]. The development of such methods is of considerable importance for the characterization of nanostructured materials. One possible solution is offered by laser photoelectron projection microscopy (LPPM). The key elements of a photoelectron projector are a sharp tip (the radius of curvature of the point tip can be significantly smaller than the laser wavelength) and a position-sensitive detector of charged particles emitted from the point tip. When a certain voltage is applied between the nanotip and detector, photoelectrons emitted under the action of the laser radiation travel in the radial electric field. Since the depth of the escape of photoelectrons is typically within a few nanometers [2], the object of investigation in this case is the point tip surface. Due to the projection effect, the photoelectron-image magnification of the laser-irradiated surface nanostructure obtained in the detector plane can reach up to 10^4–10^6. Previously, this method was successfully used for the observation of single color centers on the surface of a LiF crystal [3].

This investigation was aimed at the optical visualization of organic nanocomplexes by means of femtosecond LPPM. We have studied nanostructures formed on the surface of a metal tip upon application of a solution of Coumarin-153 (C153) organic dye in ethyl alcohol. The probability of the photoinduced decomposition of the C153 molecules in this experimental geometry is very small, because the metal substrate surface produces rapid quenching of the laser-excited molecular electron states [4, 5]. The organic dye used in these experiments belongs to the class of promising chromophores for biologically active macromolecules [6].

The experiments were performed on a setup described elsewhere [3]. A simplified scheme of the experimental setup is presented in Fig. 1. The tip was a commercially available quartz capillary (μTIP™, WPI, Israel) with a diameter of d = 100 nm, onto which a nickel film of definite thickness was deposited. Mounted in a vacuum chamber, the capillary was oriented so that its tip faced a position-sensitive detector of charged particles (microchannel plate, MCP). The distance between the nanotip and the detector surface was L = 7 cm. The orientation of the capillary in the vacuum chamber could be adjusted within ±10° with the aid of a special vacuum feedthrough.

The LPPM measurements were performed using femtosecond pulses ($\tau_p \cong 60$ fs) of laser radiation with a wavelength of $\lambda \cong 400$ nm (which falls within the optical absorption band of C153 [7]) and a pulse repetition rate of ≅76 MHz. The pulse energy could be varied within 0.03–0.3 nJ. The laser radiation was focused on the sample by a lens with a focal distance of $f_L \cong$ 12 cm. The use of femtosecond laser pulses provides

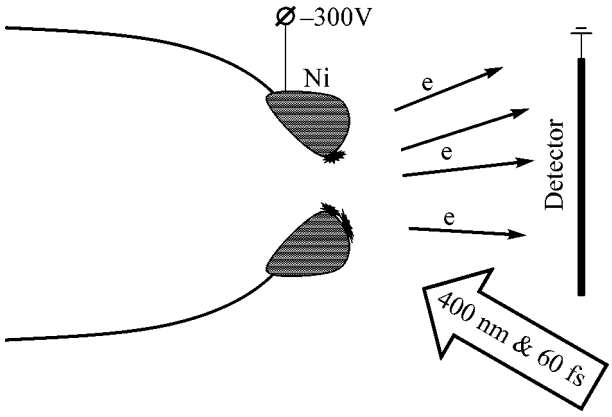

Fig. 1. Schematic diagram of the experimental setup. The asterisks show organic nanocomplexes.

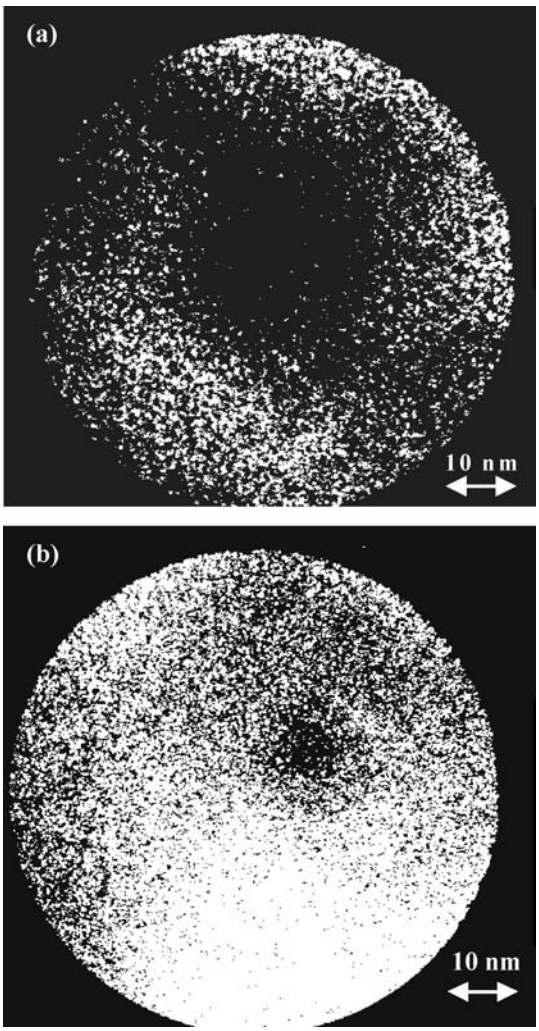

Fig. 2. Photoelectron images of the tip of a 100-nm-diameter quartz capillary covered with a (a) 25- and (b) 40-nm-thick nickel layer (an observation time of 1.5 and 3 min, respectively).

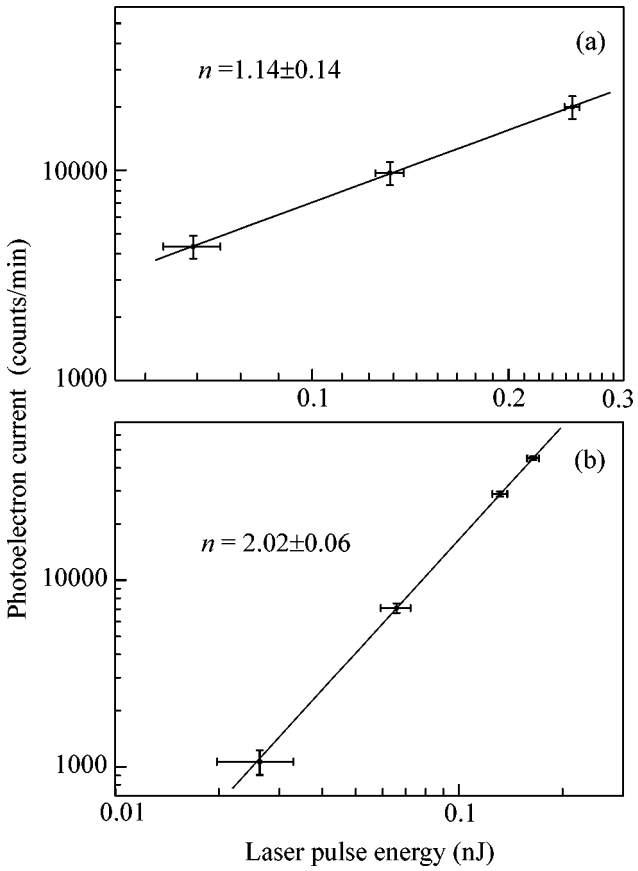

Fig. 3. Plots of the photoelectron current versus laser-pulse energy for (a) a capillary covered with a 40-nm-thick layer of nickel and (b) the same metallized capillary with deposited Coumarin 153 dye molecules. The points present the experimental data with error bars; the solid lines correspond to the (a) linear and (b) quadratic dependences of the photocurrent on the laser-pulse energy.

for an effective laser-induced photoelectron emission without significant heating of the sample.

In the first stage of the experiments, we obtained the photoelectron images of two nickel-coated capillaries (Fig. 2). For this purpose, a relatively small negative potential $\varphi_{tip} = -300$ V was applied to the irradiated nanotip. The thickness of the deposited nickel layer was controlled by changing the deposition time and amounted to 25 nm (Fig. 2a) and 40 nm (Fig. 2b). The difference between the diameters of the capillary channel in these two cases was $\Delta d \cong 30 \pm 5$ nm. The photoelectron signal depends linearly on the laser pulse energy (Fig. 3a). In our case, the applied static field ($F \sim 1$ V/nm) reduces the work function φ_{WF} (for nickel, $\varphi_{WF} \cong 4.6$ eV [8]) and provides for single-photon-induced electron emission from the metal surface irradiated by light with $\lambda = 400$ nm.

The magnification coefficient k of an electron projection microscope can be calculated using the well-known expression [9]

$$k \cong L/(\eta^* r^* \theta), \quad (1)$$

where r is the capillary radius, $\theta \cong 1.5$ [9], and η is a factor taking into account the contraction of the image of the central region of the capillary tip due to converging field lines. Assuming that $\eta \cong 2$, we can estimate the magnification coefficient as $k \cong 4.7 \times 10^5$.

In the LPPM method employed, the main error of measurement of the characteristic dimensions of nanostructures, which eventually determines the spatial resolution, is related to the nonzero initial transverse component of the photoelectron velocity. Indeed, electrons possessing a nonzero energy E_0 are detected by a position-sensitive detector with a spatial uncertainty of

$$\phi \cong 2L(E_0/e\varphi_{tip})^{1/2}. \quad (2)$$

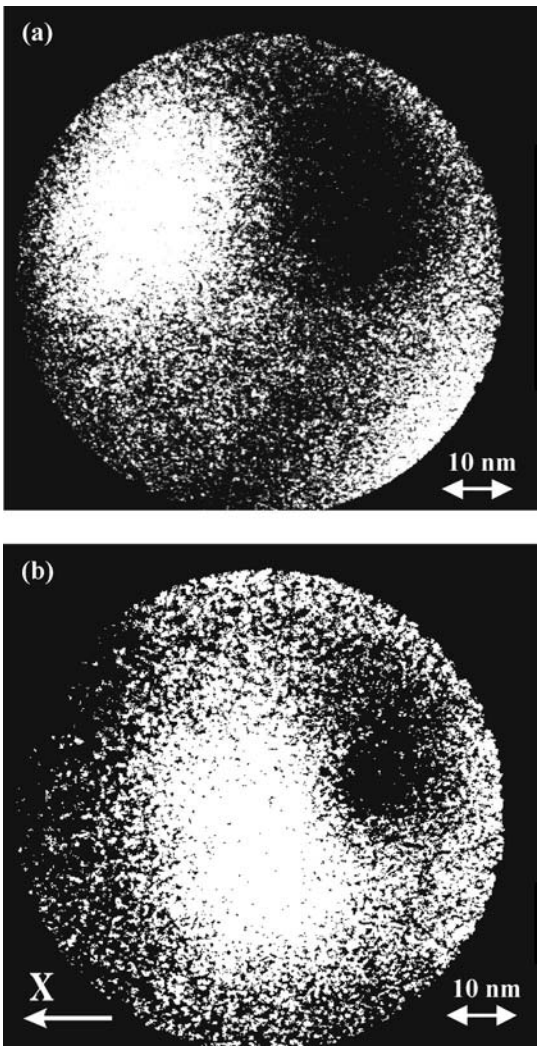

Fig. 4. Photoelectron images of the tip of a quartz capillary with a deposited nanocomplex obtained at a laser-pulse energy of (a) 0.16 and (b) 0.28 nJ.

For $E_0 \leq 0.1$ eV, the error of the measurements is approximately $\Delta \cong \phi/k \leq 5$ nm. This allows the LPPM method to be used for the investigation of nanoobjects with a characteristic size as small as ~5–10 nm.

Analysis of the images presented in Fig. 2 with the use of (1) shows that the diameters of the holes are $d_{25\,\mathrm{nm}} \cong 35 \pm 5$ nm (Fig. 2a) and $d_{40\,\mathrm{nm}} \cong 11 \pm 5$ nm (Fig. 2b). The difference is $\Delta d = 24 \pm 7$ nm, which agrees (to within the experimental uncertainty) with the estimate obtained above using the relation between the hole size and the deposited layer thickness. It should be emphasized that this agreement confirms the validity of the assumptions made above.

We have also performed experiments with an electron beam traveling through the capillary channel. For this purpose, a bundle of silicon nanotubes acting as an electron emitter was introduced into the rear end of the capillary (not depicted in Fig. 1). It is natural to assume that the number of electrons detected in this geometry at the capillary exit is determined by the channel cross section. The ratio of electron currents measured for the two samples studied was $i_{25\,\mathrm{nm}}/i_{40\,\mathrm{nm}} \cong 5$. According to this, the ratio of the output hole diameters can be estimated as $d_{25\,\mathrm{nm}}/d_{40\,\mathrm{nm}} \cong 2.2$, which is also in good agreement with the independent estimates obtained by another method. The results of the measurements performed with the nanotube emitter will be reported in more detail in a separate publication.

In the second stage of our experiments, the nickel-coated capillary was dipped into a solution of C153 dye molecules in ethyl alcohol (the solution concentration was $n \cong 2.4 \times 10^{19}$ cm^{-3}) and then dried. Irradiation of such a sample with femtosecond pulses of 400-nm laser radiation showed a quadratic dependence of the photoelectron current on the laser-pulse energy (Fig. 3b). According to published data [10], the ionization potential of the organic dye molecule is ≥7 eV. The photoionization of such molecules in the applied static electric field ($F \sim 1$ V/nm) requires at least two photons. It should be recalled that the dependence of the photoelectron current on the laser-radiation energy measured before the application of the dye molecules on the sample was linear (Fig. 3a).

When the laser-pulse energy was increased from 0.16 to 0.28 nJ, the complex of dye molecules exhibited movement over the tip surface (Fig. 4). The displacement observed in Fig. 4 occurred within approximately 1 min. This process is probably related to heating of the sample (the used laser-radiation power was 0.28 nJ × 76 MHz = 21 mW).

Using laser radiation with a pulse energy of 0.28 nJ, we performed an additional series of measurements to determine the dependence of the coordinate x of the center-of-gravity of the photoelectron image of the nanostructure (the x-axis direction is shown in Fig. 4b) on the time of exposure to the laser radiation (Fig. 5a). The exposure was additionally accompanied by a significant decrease in the signal of the photoelectron emission (Fig. 5b). A comparison of the data presented in Figs. 5a and 5b suggests that the drop in the photoelectron response and the decrease in the velocity of the motion of the nanostructure proceed within approximately the same interval of time. These changes may reflect both the photoinduced decomposition of some of the organic dye molecules (with the corresponding decrease in the degree of heating of the nanocomplex) and the desorption of some fragments of the nanocomplex under the action of the laser radiation [11].

It should be noted that the experimental data presented in Fig. 5b are quite well described by the equation of exponential decay with a characteristic time of about 1 min. This expression shows that the photoelectron response at the initial time was about 170000 ± 16000 counts per minute (cpm). Assuming a quadratic energy dependence (Fig. 3b), the signal intensity at the

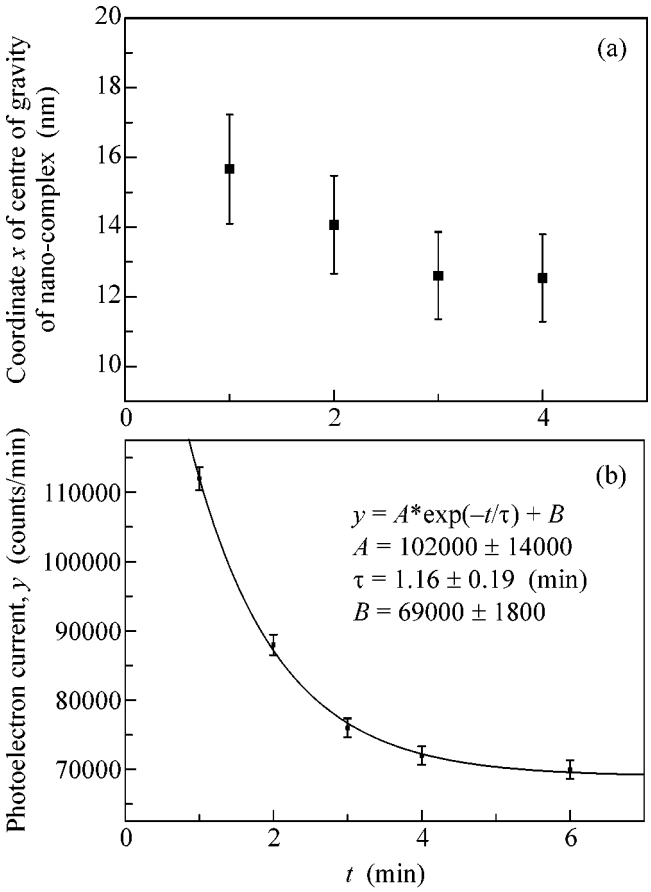

Fig. 5. Plots of (a) the coordinate x of the center-of-gravity of the photoelectron image of a nanocomplex and (b) the photoelectron current versus the time of irradiation of the sample at a laser-pulse energy of 0.28 nJ. The x-axis direction is indicated in Fig. 4b. The points present the experimental data with error bars (the data acquisition time was 30 s); the solid curve shows the results of interpolation.

initial time for Fig. 5b at a laser pulse energy of 0.28 nJ should be 133000 ± 20000 cpm (this estimation also assumes that the spatial nonuniformity of the MCP detector efficiency for photoelectrons may reach up to 10% of the total count). We note that the two estimates coincide to within the indicated error limits. Based on these results, we may assume that the "jump" of the nanocomplex depicted in Fig. 4 was not accompanied by significant changes in the photoelectron signal. Therefore, the observed process cannot be attributed to the laser-induced desorption of the dye molecules. However, it should be recalled that a relatively small displacement of the center-of-gravity of the nanostructure (Fig. 5a) was accompanied by a significant decrease in the photoelectron emission (Fig. 5b) and might be caused by the desorption of some fragments of the nanocomplex under the action of the laser radiation.

In conclusion, we have experimentally demonstrated the possibility of imaging organic nanocomplexes on the surface of a nanotip by means of LPPM. The fact of visualization of a 10-nm hole in the laser-irradiated capillary shows evidence of the rather high spatial resolution (on a level of 5 nm) achieved in these experiments.

We are grateful to S.K. Sekatskiĭ for kindly providing 100-nm-diameter quarts capillaries for the experiments. This study was supported by the Ministry of Industry, Science, and Technology of the Russian Federation, project no. 40.020.1.1.1163.

REFERENCES

1. S. Kawata, M. Ohtsu, and M. Irie, *Nano-Optics* (Springer, Berlin, 2002).
2. O. H. Griffith and G. F. Rempfer, Adv. Opt. Electron. Microsc. **10**, 269 (1987).
3. V. N. Konopsky, S. K. Sekatskii, and V. S. Letokhov, Appl. Surf. Sci. **94/95**, 148 (1996); Opt. Commun. **132**, 251 (1996).
4. Sh. Nie and St. R. Emory, Science **275**, 1102 (1997).
5. K. H. Drexhage, J. Lumin. **1** (2), 693 (1970).
6. P. K. Chowdhury *et al.*, Photochem. Photobiol. **79** (5), 440 (2004).
7. U. Brackmann, *Lambdachrome Laser-Grade Dyes Data Sheets*, 1st ed. (Lambda Physik GmbH, Gottingen, 1986), D-3400.
8. A. A. Malyutin, in *Handbook of Physical Quantities*, Ed. by I. S. Grigor'ev and E. Z. Meĭlikhov (Énergoatomizdat, Moscow, 1991; CRC Press, Boca Raton, N.Y., 1997).
9. E. W. Muller and T. T. Tsong, *Field Ion Microscopy, Field Ionization, and Field Evaporation* (Pergamon Press, Oxford, 1973; Nauka, Moscow, 1980).
10. I. V. Sokolova, N. Yu. Vasil'eva, Ya. O. Vylegzharina, and G. V. Maier, Opt. Spektrosk. **79** (3), 460 (1995) [Opt. Spectrosc. **79**, 426 (1995)].
11. V. S. Antonov, V. S. Letokhov, Yu. A. Matveets, and A. N. Shibanov, Poverkhnost, No. 1, 54 (1982).

Translated by P. Pozdeev